



## 저작자표시-비영리-동일조건변경허락 2.0 대한민국

이용자는 아래의 조건을 따르는 경우에 한하여 자유롭게

- 이 저작물을 복제, 배포, 전송, 전시, 공연 및 방송할 수 있습니다.
- 이차적 저작물을 작성할 수 있습니다.

다음과 같은 조건을 따라야 합니다:



저작자표시. 귀하는 원저작자를 표시하여야 합니다.



비영리. 귀하는 이 저작물을 영리 목적으로 이용할 수 없습니다.



동일조건변경허락. 귀하가 이 저작물을 개작, 변형 또는 가공했을 경우에는, 이 저작물과 동일한 이용허락조건하에서만 배포할 수 있습니다.

- 귀하는, 이 저작물의 재이용이나 배포의 경우, 이 저작물에 적용된 이용허락조건을 명확하게 나타내어야 합니다.
- 저작권자로부터 별도의 허가를 받으면 이러한 조건들은 적용되지 않습니다.

저작권법에 따른 이용자의 권리는 위의 내용에 의하여 영향을 받지 않습니다.

이것은 [이용허락규약\(Legal Code\)](#)을 이해하기 쉽게 요약한 것입니다.

[Disclaimer](#)

공학박사학위논문

**Tunable pore structure of Carbide Derived  
Carbon using accurate control of  
TiC solid solution**

TiC 고용상의 조성 조절을 이용한  
CDC의 기공구조 조절

2012년 8월

서울대학교 대학원

재료공학부

서 문 수

# **Tunable pore structure of Carbide Derived Carbon using accurate control of TiC solid solution**

TiC 고용상의 조성 조절을 이용한 CDC의 기공구조 조절

지도교수 강 신 후

이 논문을 공학박사 학위논문으로 제출함

2012년 8월

서울대학교 대학원

재료공학부

서 문 수

서 문 수의 공학박사 학위논문을 인준함

2012년 6월

위 원 장	_____한 승 우_____인
부위원장	_____강 신 후_____인
위 원	_____남 기 태_____인
위 원	_____김 동 옥_____인
위 원	_____전 석 우_____인

**Tunable pore structure of Carbide Derived  
Carbon using accurate control of  
TiC solid solution**

Advisor : Shinhoo Kang

by  
Moonsu Seo

2012.08

Department of Materials Science and Engineering  
Graduate School  
Seoul National University

# Abstract

Novel precursor, titanium solid solution carbide, was produced for the synthesis of carbide derived carbon (CDC) which has variety of applications such as supercapacitor, catalyst support, or adsorbents for gases like hydrogen, methane or separation of CO<sub>2</sub> gas. All these applications are possible due to its tunable pore characteristics with experimental parameters.

First, we can successfully synthesize and control accurate composition of solid solution precursor such as (Ti<sub>1-x</sub>Me<sub>x</sub>)C and Ti(C<sub>1-x</sub>A<sub>x</sub>) by high energy ball milling. Second, with selection of the substitutional atom (A), it could be possible to change specific dimension of pore volumes which can be covered in the range of micropore (<2nm) or mesopore size (2nm-50nm). Third, properties for hydrogen storage and supercapacitor are analyzed. Finally, Pore structure of carbide derived carbon was successfully designed by chlorination of Ti(C<sub>1-x</sub>A<sub>x</sub>)<sub>(A= Oxygen or Nitrogen)</sub> solid solution phase. Ti(C<sub>1-x</sub>A<sub>x</sub>)-CDC has significantly better values of SSA and pore volume than reported before. Ti(C<sub>1-x</sub>O<sub>x</sub>)-CDC contains micropore sized pore, in contrast, Ti(C<sub>1-x</sub>N<sub>x</sub>)-CDC is dominantly shows formation of mesopore. Thus, characteristic dimensions of mesopore or micropore can be controlled by which kind of substitutional atom instead of carbon in solid solution. One of CDCs have noticeably shows not only 90% (V<sub>micro</sub>/V<sub>total</sub>) micropore volume fraction up to Ti(C<sub>0.7</sub>O<sub>0.3</sub>)CDC: 1.55cm<sup>3</sup>/g (V<sub>micro</sub>) per 1.72cm<sup>3</sup>/g (V<sub>total</sub>), 3200cm<sup>2</sup>/g (SSA) but also mesopore volume up to Ti(C<sub>0.5</sub>N<sub>0.5</sub>) : 3.34cm<sup>3</sup>/g (V<sub>meso</sub>) per 3.45cm<sup>3</sup>/g (V<sub>total</sub>) , 522.1cm<sup>2</sup>/g (SSA) by selective extraction of

titanium. Although  $(\text{Ti}_{1-x}\text{Me}_x)\text{C}$ -CDC didn't show significant difference, its result was used for the basic data for analysis of CDC pore structure with molecular dynamics simulation.

**Keywords:** Ti solid solution carbide, Carbide Derived Carbon, Micropore, Mesopore, Hydrogen storage, Supercapacitor

**Student Number:** 2006-20851

# Contents

<b>Abstract</b>	i
<b>List of Figures</b>	v
<b>List of Tables</b>	vii
<b>I. Introduction</b>	1
1.1. Carbide Derived Carbons	1
1.2. Titanium Solid Solution Carbide	3
1.3. Aims of the work and outline of the thesis	4
<b>II. SYNTHESIS OF SOLID SOLUTION AND ACCURATE CONTROL COMPOSITION</b>	5
2.1. Introduction	5
2.2. Solubility limit of solid solution	5
2.3. Experimental	9
2.4. Results and Discussion	10
2.4.1. $(\text{Ti}_{1-x}\text{Me}_x)\text{C}$ (Me= W or Zr)	10
2.4.2. $\text{Ti}(\text{C}_{1-x}\text{A}_x)$ (A= O or N)	13
2.5. Summary	18
<b>III. CARBIDE DERIVED CARBON FROM TIC SOLID SOLUTION</b>	19
3.1. Introduction	19
3.1.1. Adsorption isotherms	19
3.1.2. Hysteresis	21
3.1.3. BET method	23
3.1.4. MP method	24
3.1.5. BJH	29
3.1.6. Non-Local Density Functional Theory	36
3.2. Experimental	38

3.3 Results and Discussion	39
3.3.1. $(\text{Ti}_{1-x}\text{Me}_x)\text{C-CDC}$ (Me= W or Zr)	39
3.3.2. $\text{Ti}(\text{C}_{1-x}\text{A}_x)\text{-CDC}$ (A= O or N)	41
3.4. Summary	47
<b>IV. MECHANISM OF SOLID SOLUTION CARBIDE DERIVED CARBON</b>	<b>49</b>
4.1. Introduction	49
4.2. Result and discussion of $\text{Ti}(\text{C}_{1-x}\text{A}_x)\text{-CDC}$ (A= O or N)	51
4.3. Empirical calculation method	60
4.3.1. Introduction	60
4.3.2. Assumption	61
4.3.3. Calculation	61
4.3.4. Structure of simulated results	64
4.3.5. Connolly surface area	68
4.4. Summary	71
<b>V. APPLICATIONS OF MICRO/MESO POROUS CARBIDE DERIVED CARBON</b>	<b>72</b>
5.1. Micropore of $\text{Ti}(\text{C}_{1-x}\text{O}_x)$ for hydrogen storage material	72
5.1.1. Introduction	72
5.1.2. Experiment	73
5.1.3. Result and discussion	73
5.2. Mesopore of $\text{Ti}(\text{C}_{1-x}\text{N}_x)$ for supercapacitor candidate	76
5.1.1. Introduction	76
5.1.2. Experiment	78
5.1.3. Result and discussion	78
5.4. Summary	80
<b>VI. Overall Conclusion</b>	<b>81</b>
<b>VII. References</b>	<b>82</b>
<b>Korean Abstract</b>	<b>92</b>
<b>Acknowledgement</b>	<b>93</b>



## List of Figures

- Figure 1. (a) Schematic picture of molecular sieve, (b) CDC for supercapacitor [4]
- Figure 2.  $(\text{Ti}_{1-x}\text{W}_x)\text{C}$  thermodynamic stability plot [39]
- Figure 3. Activities of (a) TiC and TiO in  $\text{Ti}(\text{C}_{1-x}\text{O}_x)$  solid solution,[48] (b) TiC and TiN in  $\text{Ti}(\text{C}_{1-x}\text{N}_x)$  solid solution at 1578K
- Figure 4.  $(\text{Ti}_{1-x}\text{W}_x)\text{C}$  experimental results (a) SEM-EDS [39] and (b) XRD [39]
- Figure 5.  $(\text{Ti}_{1-x}\text{Zr}_x)\text{C}$  experimental results of XRD ( $x=0 \sim 0.3$ )
- Figure 6. Peak shift of  $(\text{Ti}_{1-x}\text{Zr}_x)\text{C}$  in XRD ( $x=0 \sim 0.3$ )
- Figure 7. XRD result of  $\text{Ti}(\text{C}_{1-x}\text{O}_x)$  with oxygen content of (a)  $x=0\sim 1$ , (b)  $x=0.6\sim 0.9$
- Figure 8. Peak shift of  $\text{Ti}(\text{C}_{1-x}\text{O}_x)$  in XRD with oxygen content of  $x=0.6\sim 0.9$
- Figure 9. Carbon and Oxygen analysis of  $\text{Ti}(\text{C}_{1-x}\text{O}_x)$  with oxygen content of  $x=0.6\sim 0.9$
- Figure 10. XRD result of  $\text{Ti}(\text{C}_{1-x}\text{N}_x)$  with nitrogen content
- Figure 11. Peak shift of  $\text{Ti}(\text{C}_{1-x}\text{N}_x)$  with the content of nitrogen in XRD
- Figure 12. Carbon and Nitrogen analysis of  $\text{Ti}(\text{C}_{1-x}\text{N}_x)$
- Figure 13. IUPAC classification of sorption isotherms.  $P_o/P$  represents the relative
- Figure 14. Standardizing adsorption isotherm of non-porous solid with thickness of nitrogen
- Figure 15. 3 kinds of t-plots of adsorption volume ( $\text{cm}^3/\text{g}$ ) per thickness(nm) from the conversion between standard and sample isotherm
- Figure 16. (a) Schematic model of t-plot method (b)
- Figure 17. Schematic diagram of capillary condensation for BJH method.
- Figure 18. Schematic picture for understanding BJH method
- Figure 19. Schematic of the experimental process of chlorination
- Figure 20. Nitrogen adsorption isotherms at 77K with x content of  $(\text{Ti}_{1-x}\text{M}_x)\text{C}$ -CDC within solubility limit.
- Figure 21. Nitrogen adsorption isotherms at 77K with oxygen content of  $\text{Ti}(\text{C}_{1-x}\text{O}_x)\text{CDC}$
- Figure 22. Nitrogen adsorption isotherms at 77K with nitrogen content of  $\text{Ti}(\text{C}_{1-x}\text{N}_x)\text{CDC}$
- Figure 23. Micro and meso pore volume of  $\text{Ti}(\text{C}_{1-x}\text{O}_x)$  and  $\text{Ti}(\text{C}_{1-x}\text{N}_x)$
- Figure 24. Pore size distribution of  $\text{Ti}(\text{C}_{1-x}\text{O}_x)$  calculated by NLDFT.
- Figure 25. Pore size distribution of  $\text{Ti}(\text{C}_{1-x}\text{N}_x)$  calculated by NLDFT.
- Figure 26. Schematic of the synthesis steps for a  $\text{Ti}(\text{C}_{1-x}\text{A}_x)\text{-CDC}$  powders, with a proposed schematic process.

Figure 27. Nitrogen adsorption isotherms at 77K with chlorination temperature of (a)Ti(C0.7O0.3)CDC (b)Ti(C0.7N0.3)CDC

Figure 28. Micro/meso-pore volume of (a) Ti(C0.7O0.3)-CDC, (b) Ti(C0.7N0.3)-CDC with chlorination temperature. Results of TiC-CDC is from reference [76]

Figure 29. The difference of Ti(C1-xNx) with chlorination temperature between 400 °C and 800 °C, XRD result of yellow residual solid phase from 800 °C chlorination.

Figure 30. XPS results of Ti(C<sub>0.8</sub>O<sub>0.2</sub>)-CDC at (a)400 °C, (b)800 °C

Figure 31. XPS results of Ti(C<sub>0.5</sub>N<sub>0.5</sub>)-CDC at (a)400 °C, (b)800 °C

Figure 32. Mass spectroscopy of (a)TiC-CDC chlorinated 800 °C (b)Ti(C<sub>0.5</sub>N<sub>0.5</sub>)-CDC chlorinated 800 °C (c)Ti(C<sub>0.5</sub>N<sub>0.5</sub>)-CDC which is chlorinated at 400 °C

Figure 33. Dependence of CDC structure from initial carbon distribution.

Figure 34. Convergence of total energy and difference of CDC structure with simulation time.

Figure 35. Calculated structure of SiC from the surface layer with eliminating by (a)0 layer (b)2nd layers (c)3rd layer (d) 4th layer (e) 6th layer (f) 8th layer (g)residual layers (h)all layer at once from initial SiC

Figure 36. CDC structures of (a)Ti(C0.7O0.3)-CDC and (b)Ti(C0.7N0.3)-CDC after convergence

Figure 37. CDC structures of (a)TiC-CDC (b) Ti(C0.7O0.3)-CDC and (c) Ti(C0.7N0.3)-CDC after elimination of oxygen or nitrogen

Figure 38. Schematic diagram for understand the definition of connolly surface area (red line), probe molecule (N<sub>2</sub>) [109]

Figure 39. Slice planes of calculated (a)TiC-CDC, (b)Ti(C0.7O0.3)-CDC, (c)Ti(C0.7N0.3)-CDC (red: carbon occupied layers, blue: empty space)

Figure 40. Low pressure (~1atm) H<sub>2</sub> sorption isotherms at 77K with oxygen content of Ti(C1-xOx)-CDC

Figure 41. High pressure (80atm) H<sub>2</sub> sorption isotherms at 77K with oxygen content of (a) TiC-CDC and (b)Ti(C0.7O0.3)-CDC

Figure 42. Schematic explanation of the optimum pore size for the highest surface area accessible by the electrolyte ions.

Figure 43. CV taken at scan rates of 50mV/s for Ti(C<sub>0.5</sub>N<sub>0.5</sub>)CDC chlorinated at 800 °C

## **List of Tables**

Table 1. Compositions of  $\text{Ti}(\text{C}_{1-x}\text{A}_x)$

Table 2. Pore properties of  $(\text{Ti}_{1-x}\text{Me}_x)\text{C}$ -CDC

Table 3. Summary of pore properties of  $\text{Ti}(\text{C}_{1-x}\text{A}_x)$

Table 4. Summary of pore properties of  $\text{Ti}(\text{C}_{1-x}\text{O}_x)$  with chlorination temperature

Table 5. Summary of pore properties of  $\text{Ti}(\text{C}_{1-x}\text{N}_x)$  with chlorination temperature

Table 6. Specific surface area and total pore volume calculated by Connolly surface which is from the surface layer with eliminating Si atoms in (a)0 layer (b)2nd layers (c)3rd layer (d) 4th layer (e) 6th layer (f) 8th layer (g)residual layers (h)all layer at once from initial SiC

Table 7. Specific surface area and pore volume calculated by Connolly surface of CDCs.

# I. Introduction

## 1.1. Carbide Derived Carbon (CDC)

Porous carbon materials have been receiving much attention due to their thermal stability, light weight and high porous properties. A detailed description of the pore structure in terms of pore size distribution may be used for correlation and prediction of the performance of carbon materials in industrial applications as well as in developing new porous materials.[1] The classification of pores given by IUPAC is: micropore ( $<2.0\text{nm}$ ), mesopore ( $2.0\text{--}50\text{nm}$ ), macropore ( $>50\text{ nm}$ ).[2] Micropore can be further divided into narrow ( $<0.7\text{nm}$ ) and wide ( $0.7\text{--}2.0\text{nm}$ ) micropores.[3] Porous carbon is the one of good candidates for pore applications as a supercapacitor, separation or adsorbents for gases like hydrogen, methane or separation of  $\text{CO}_2$  gas as seen in Figure 1.

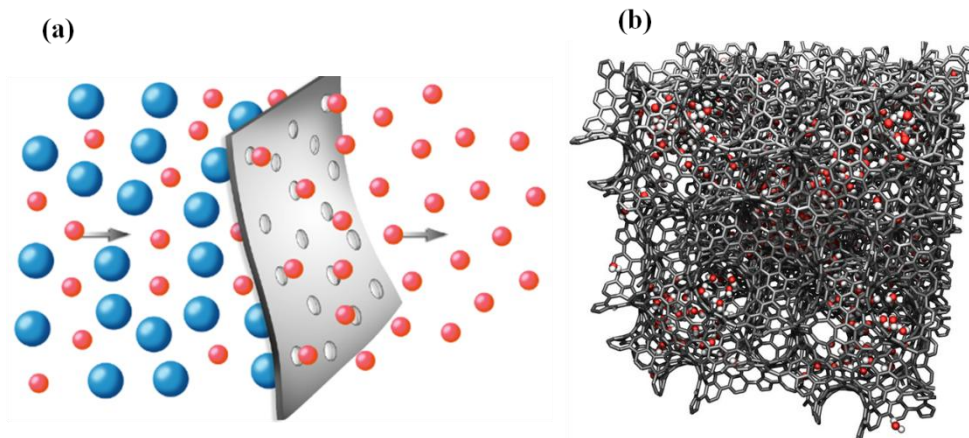


Figure 1. (a) Schematic picture of molecular sieve, (b)CDC for supercapacitor [4]

Mesopores and micropores have been treated separately when characterizing porous materials by mean of adsorption due to the limitations in the mathematical models used for extracting structural information from the isotherms, and in the description of pore filling mechanisms for variable pore sizes. The dimensions of mesopore are traditionally calculated using the Kelvin equation, but in the recently the use of models

based on the density functional theory (DFT), which seem to give a better description of the adsorption in the pores, is increased, especially as it covers both meso- and micropore regions.[5, 6] One of carbon based porous materials, novel microporous material was reported, as named CDC (Carbide Derived Carbon). CDC shows different pore volume, pore size distribution with raw carbides, chlorination temperature. Using CDC, it has been shown recently that the sorption capability of hydrogen or methane gas which is related energy industry which is depends on the micropores. High fraction of micropore leads high SSA and good to fill gases. Traditionally, it understood that sorption amount depends on the SSA or pore size. However, it does not necessarily scale with the surface area or pore size, but it depends on the volume of pores smaller than 1nm which is in the range of micropore.[7] While mesopore has unique properties such as semiconductivity, ability to intercalate, gas storage, lubricant, biomolecule adsorption, and drug delivery, etc.[8] For example, high specific capacitance; larger pores facilitate ion mobility throughout CDC particles.[9] To satisfy theses needs, exact pore size and pore volume control is the key issue. Previously, it is reported that total and characteristic dimension of micro- and mesopores can be controlled by choice of a binary or ternary carbide solid solution and variation of the chlorination temperature.[10] Pore structure of CDC depends on the initial carbide unit cells or experimental parameter (temperature, post annealing, etching agent)[10-12] Nowadays, many efforts to control pore structure with various raw materials can be seen. Already, most of carbides like binary (TiC, ZrC, HfC, WC, SiC, B<sub>4</sub>C, Al<sub>4</sub>C<sub>3</sub>)[13-17] and ternary MAX phases (Ti<sub>3</sub>SiC<sub>2</sub>, Ti<sub>3</sub>AlC<sub>2</sub>, Ti<sub>2</sub>AlC, Ta<sub>2</sub>AlC) investigated.[4, 18-20] In this way, tunable pore size and volume have been challenged for long time, but there are limitations about controlling compositions of raw precursors due to stable carbide phase. Gogotsi suggested that the larger size of metal atom in Me-C carbide structure appear to favor the formation of micropore volume, on the contrary, crystal structure of initial carbides effects mesopore volume.[21] Also recently, his group has shown that polymer derived ceramics (PDCs) provide an additional degree of freedom for

optimizing CDC porosity and performance by controlling the pyrolysis and chlorination conditions (e.g., temperature). They mentioned that the high mesopore volume is obtained by chlorination of SiCN as a raw material which is synthesized from polymer.[22, 23] But it needs stable nanocrystalline  $\text{Si}_3\text{N}_4$  phase for mesopore formation so they need further work to control accurate  $\text{Si}_3\text{N}_4$  content in raw precursors. Many experimental or simulation [24-26] works have been done, however it is still not understood exactly about pore formation mechanism during chlorination.

## 1.2. Titanium Solid Solution Carbide

TiC based solid solution phases are famous for variety of applications such as cutting tools, transparent material, tunable electronic structure of carbide. Particularly, TiC based solid solution materials which will be investigated in present study have the B1(NaCl, Fm-3m, No.225) crystal structure because the crystal structure of solvent material remained without transformation from TiC. During synthesis of solid solution, solute and solvent combination is very important because kinds and amount of solute are able to derive a lattice distortion, a disruption of physical, chemical homogeneity of solvent materials. There are numerous researches in TiC based solid solution materials. The primary material of TiC based solid solution is  $(\text{Ti}_{1-x}\text{M}_x)\text{C}$ -type solid solution, it is known to improve the toughness of the composite and has drawn much attention from researchers in cutting material field.[27-30] For example, homogeneous  $(\text{Ti}_{1-x}\text{W}_x)\text{C}$  phase has been demanded by hard material industries since the 1980s.  $(\text{Ti}_{1-x}\text{W}_x)\text{C}$  solid solution material which is solutionized WC(hex.) in TiC(B1) matrix interested to increase toughness without losing hardness compared to TiC.[31, 32] Many attempts have been made to synthesize  $(\text{Ti}_{1-x}\text{W}_x)\text{C}$  solid solution powders via the thermal reaction of a TiC/WC powder mixture at high temperatures or by the self heat-propagation synthesis (SHS) of a Ti, W and C powder mixture.[33-35] Since TiC is thermodynamically more stable than WC,  $(\text{Ti}_{1-x}\text{W}_x)\text{C}$  is synthesized commercially by reacting TiC with WC in the temperature range of 1700–2100°C for periods ranging

from 10 to 20 h.[33] This method is expensive and always results in inhomogeneous powders with unreacted TiC. Similar results were reported when  $(\text{Ti}_{1-x}\text{W}_x)\text{C}$  was synthesized through SHS.[35] Also Xiabo et al. studied homogeneous  $(\text{Ti}_{1-x}\text{Zr}_x)\text{C}$ [36] and  $(\text{Ti}_{1-x}\text{Mo}_x)\text{C}$ [37] powders too.

Meanwhile,  $\text{Ti}(\text{C}_{1-x}\text{N}_x)$  which is blended TiC and TiN has been used in the field of cutting tool too because of their high hardness, strength, wear resistance and phase stability that is necessary for high temperature processing.[38] Mechanical and physical properties of TiC are enhanced using appropriate amount of TiN as a solute materials.[39] Also titanium oxycarbide,  $\text{Ti}(\text{C}_{1-x}\text{O}_x)$ , has been considered as a thin film coating material for decorative applications due to possibility of tailoring its optical properties by changing the electronic structure with tunable oxygen/carbon ratio.[40, 41]

### 1.3. Aims of the work and outline of the thesis

Even many CDCs which are synthesized from different raw carbides have studied recently, but studies of CDCs from solid solution are very few. Here, we introduce a synthesis of CDCs from rational design of raw  $\text{Ti}(\text{C}_{1-x}\text{A}_x)$  (A= Oxygen or Nitrogen) or  $(\text{Ti}_{1-x}\text{Me}_x)\text{C}$  (Me= Tungsten or Zirconium) which is produced by high energy ball milling and carbothermal reduction. A great possibility for the tunable micro-/mesopore volume can be shown by selection of substitutional atoms in raw precursors. This thesis shows that solid solution CDCs provide an additional degree of freedom for controlling pore structure such as SSA, PSD, pore volume. In this work, it is demonstrated that pore properties of CDC can be fine tuned with a high accuracy by controlling raw carbide solid solution composition and varying the additional atoms. Specially, we suggest definitely clear results of the tunable dimension of pore volume which can be covered specific range of micro- or mesopore with the selection of oxygen or nitrogen content in cubic  $\text{Ti}(\text{C}_{1-x}\text{A}_x)$  structure as a raw material.

## **II. Synthesis of TiC solid solution & accurate control composition**

### **2.1. Introduction**

Mechanical alloying (MA) of powder particles has been developed as a versatile alternative of many processing routes in preparing nanostructure materials such as inert gas condensation, electrodeposition, rapid solidification, sputtering, crystallization of amorphous phase by annealing. It is greatly affected by a number of factors that play very important roles in the design of new alloying materials due to its simplicity, relatively inexpensive equipment and its potential for large-scale production.[42] One of MA methods, high energy ball milling is an efficient and simple method for the fabrication of alloy materials with sub-micron or nanostructure, especially for manufacturing of composite powders. In ball milling process, main factors are rotation speed, size of balls, weight ratio of balls to powder, proper milling time etc. Because of the variety of the powder materials, the selection of parameters varied substantially. In particular, the control of particle size and the amount of defects (lattice strain) can be changed reaction temperature effectively and derive less agglomeration and synthesis of homogeneous particles. Thus, high energy ball milling is effective method to synthesize solid solution phase.[32] It means that partial substitution of titanium or carbon atom by other interested elements is possible with our own optimized milling process.

### **2.2. Solubility limit of solid solution**

The solid solution materials have a solubility limit due to the different crystal properties between sorbent and solute materials.[43-46] Metcalfe A. [47] investigated the solubility limit of WC in TiC matrix material at finite temperature. Solubility limit and phase stability of solid solutions in this thesis were already calculated previously



with thermodynamic calculation. Also  $(\text{Ti}_{1-x}\text{W}_x)\text{C}$  is previously studied from J. Jung.[31] He has reported that dissolving tungsten into TiC system improves mechanical properties of TiC. Also Kim calculated thermodynamic stability of  $(\text{Ti}_{1-x}\text{W}_x)\text{C}$  solid solution phase with DFT and compared experimental result as seen in Figure 2 and **Figure 4**. [39]  $(\text{Ti}_{1-x}\text{W}_x)\text{C}$  solid solutions have a solubility limit because TiC and WC have a different crystal structure B1 and hexagonal, respectively. He showed solubility limit (x) of tungsten in TiC is 0.4wt%. Also recently, solid solution of zirconium in TiC has been done to enhance fracture toughness of TiC and its solubility limit(x) is observed 0.19wt% of  $(\text{Ti}_{1-x}\text{Zr}_x)\text{C}$  at 1610°C.[36] Generally, transitional carbides have very broad non-stoichiometric compositions with  $\text{MeC}_x$ , resulting to contain much vacancy when its system has carbon deficiency. It means that certain atom can substitute to carbon position easily without deformation of crystal structure. Based on our previous study,[48] thermodynamic calculation of  $\text{Ti}(\text{C}_{1-x}\text{O}_x)$  solid solution shows positive activity deviation behavior from ideal solution between TiC and TiO. It means that  $\text{Ti}(\text{C}_{1-x}\text{O}_x)$  phase is relatively unfavorable. Figure 3(a) and (b) show the activities to form solid solution between TiC and TiO, TiC and TiN each calculated from the Gibbs-Duhem equation at 1300°C. In spite of this positive activity deviation of  $\text{Ti}(\text{C}_{1-x}\text{O}_x)$ , we can control carbon/oxygen ratio with high accuracy in specific range due to the broad nonstoichiometric composition of titanium carbide. By contrast,  $\text{Ti}(\text{C}_{1-x}\text{N}_x)$  shows strong negative activity deviation from ideal solution in Figure 3(b). This stability behavior of  $\text{Ti}(\text{C}_{1-x}\text{N}_x)$  investigated that nitrogen rich solid solution materials have higher stability than that of the carbon rich solid solution. This result is originated from high stability of TiN.

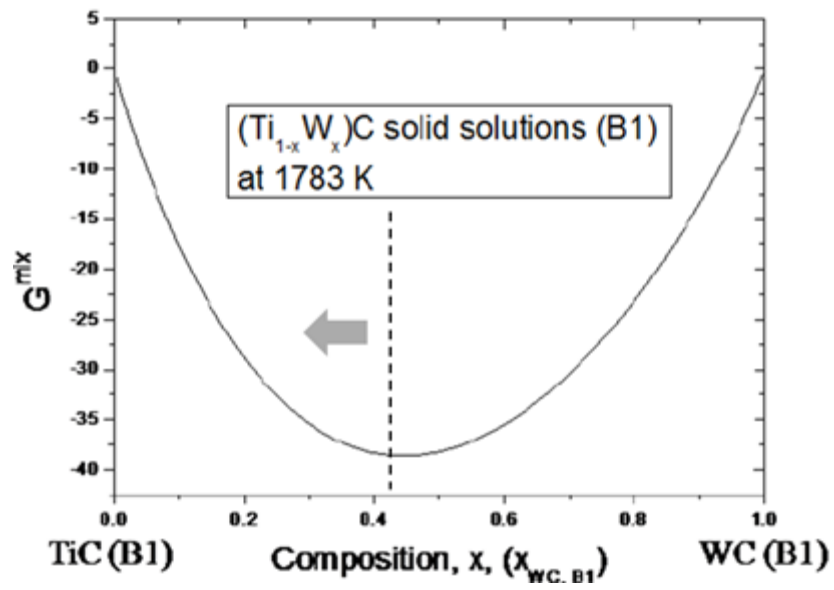


Figure 2.  $(Ti_{1-x}W_x)C$  thermodynamic stability plot [39]

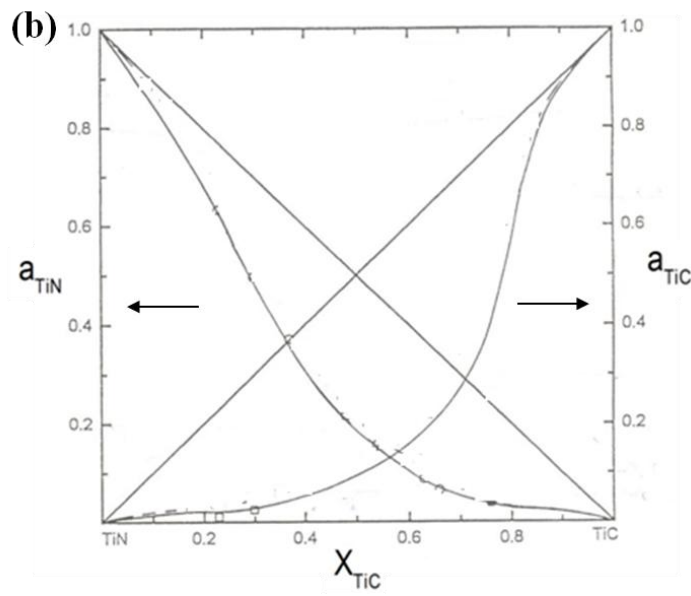
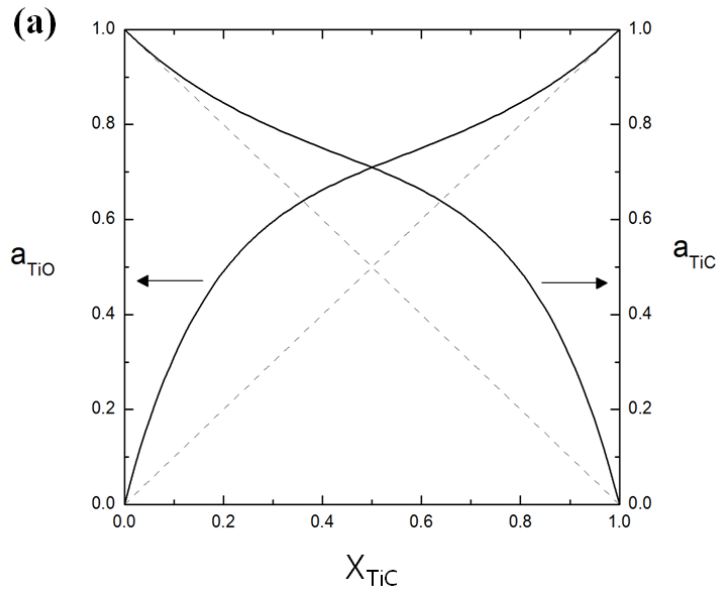
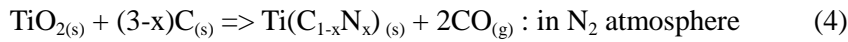
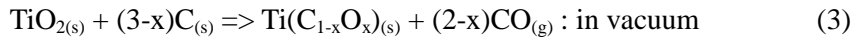
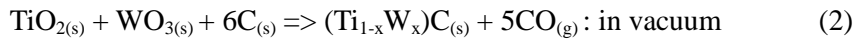
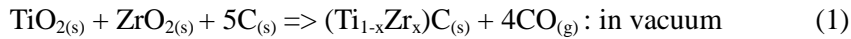


Figure 3. Activities of (a) TiC and TiO in  $\text{Ti}(\text{C}_{1-x}\text{O}_x)$  solid solution,[48] (b) TiC and TiN in  $\text{Ti}(\text{C}_{1-x}\text{N}_x)$  solid solution at 1578K[49]

## 2.3. Experimental

TiC based solid solution carbide is synthesized with high energy ball milling and carbothermal reduction. By this milling process, homogeneous nanoscale mixing is possible and it is easy to control accurate composition of  $(\text{Ti}_{1-x}\text{Me}_x)\text{C}$  or  $\text{Ti}(\text{C}_{1-x}\text{A}_x)$  solid solution. They were synthesized using anatase- $\text{TiO}_2$  (99+% purity,  $43\mu\text{m}$  avg. particle size, Aldrich) powder,  $\text{WO}_3$  (99+% purity,  $20\mu\text{m}$  avg. particle size, Aldrich),  $\text{ZrO}_2$  (99.9%, Aldrich,  $5\mu\text{m}$ ) and graphite powder (Seunglim carbon metal,  $<1.65\mu\text{m}$ ).

The oxides were mixed with carbon to achieve the target compositions. The oxide/carbon mixture was subjected to high-energy ball milling using a planetary mill (Pulverisette 5, Fritsch, Germany) at a ball-to-powder ratio (BPR) of 30:1 by weight. It is used zirconia jar and Ytria-stabilized zirconia (YSZ) balls for the least contamination. All milling was carried out at a speed of 250 rpm for 20hrs. Finally, solid solution powders were prepared by carbothermal reduction at  $1300^\circ\text{C}$  for 2hrs. After carbothermal reduction, the oxygen and nitrogen content was measured by Oxygen/Nitrogen analyzer (Model: 631-800-100, LECO, USA). The following overall reaction sequence is resulted to occur with carbothermal reduction or nitridation process with the milled mixture of oxides and graphite carbon powder. Stable oxide can minimize contamination from jar or balls. The reaction is followed as:



## 2.4. Results and Discussion

### 2.4.1. $(\text{Ti}_{1-x}\text{Me}_x)\text{C}$ , (Me= W or Zr)

Figure 4(a) shows the result of SEM-EDS from Kim's thesis[39]. It shows the variation of tungsten content (x) in  $(\text{Ti}_{1-x}\text{W}_x)\text{C}$  of grains. Up to the tungsten content is 0.4, difference of tungsten content in the  $(\text{Ti}_{1-x}\text{W}_x)\text{C}$  grains between target and real compositions are very small. It indicates added WC are fully solutionized in  $\text{TiC(B1)}$ . [39] Above  $x=0.5$ , the tungsten content converged at  $x \sim 0.47$ . Also, this result agrees with the XRD data in Figure 4(b), the increase of lattice parameter means expansion of lattice structure of  $\text{TiC}$ . [39] And the precipitate of WC or  $(\text{Ti}_{1-x}\text{W}_x)$  inter-metallic phase shows over solubility limit of tungsten. And Figure 5 shows XRD result of  $(\text{Ti}_{1-x}\text{Zr}_x)\text{C}$  with x content by own milling and reduction process. From the linear peak shift of Figure 6, we can ensure the effect of lattice expansion of  $\text{TiC}$  with the substitution of zirconium too. ZrC separation can be observed at  $x=0.06$  of  $(\text{Ti}_{1-x}\text{Zr}_x)\text{C}$ . The difference of solubility limit with reference ( $x=0.19$ ) [36] is due to the synthesis temperature. Thus, it shows complete  $(\text{Ti}_{1-x}\text{Zr}_x)\text{C}$  and  $(\text{Ti}_{1-x}\text{W}_x)\text{C}$  solid solution phase without other residual phase within solubility limit.

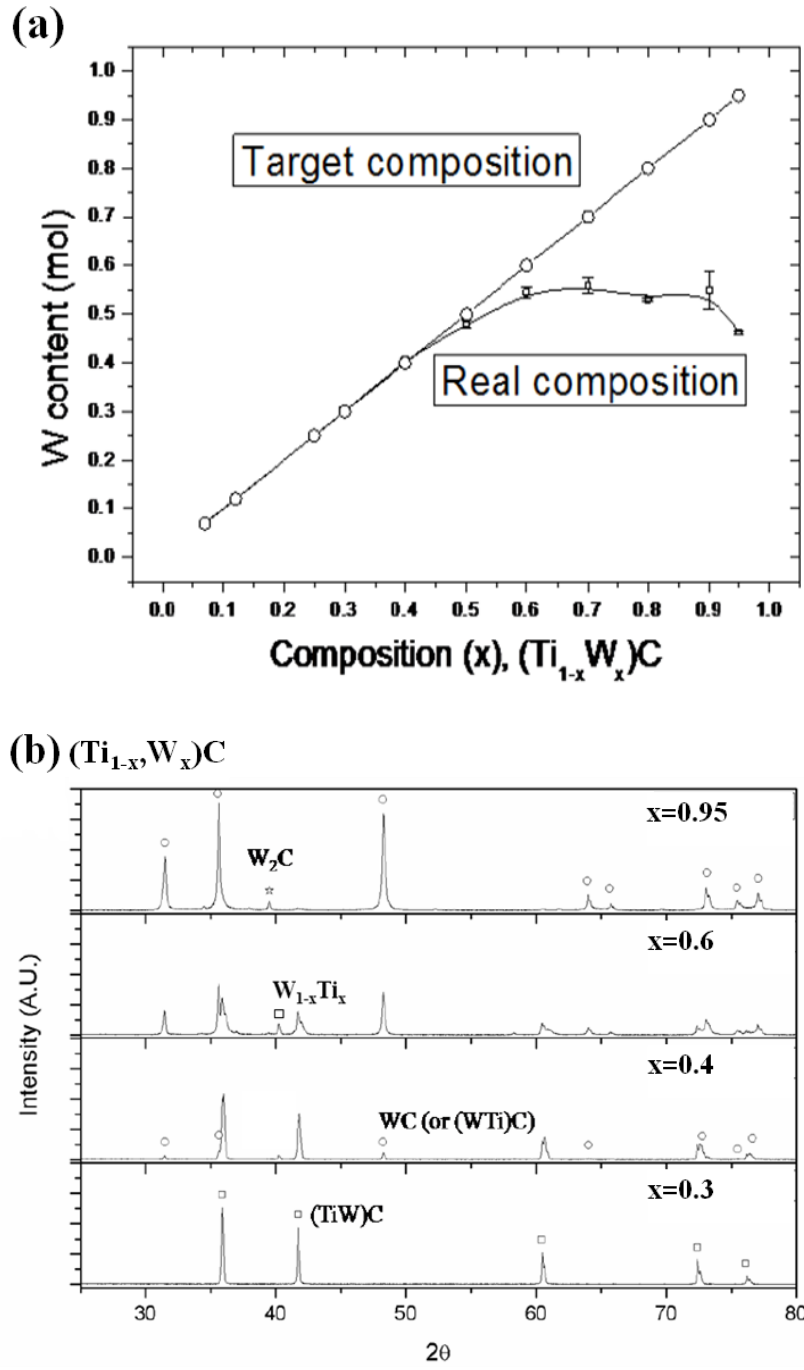


Figure 4.  $(\text{Ti}_{1-x}\text{W}_x)\text{C}$  experimental results (a) SEM-EDS [39] and (b) XRD [39]

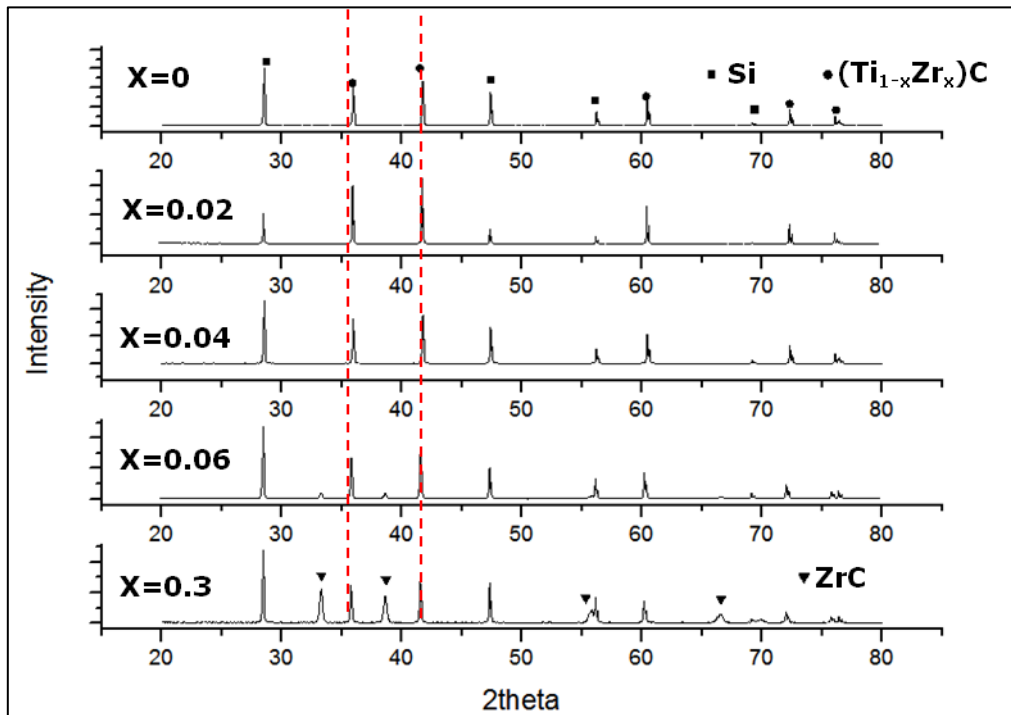


Figure 5.  $(\text{Ti}_{1-x}\text{Zr}_x)\text{C}$  experimental results of XRD ( $x=0 \sim 0.3$ )

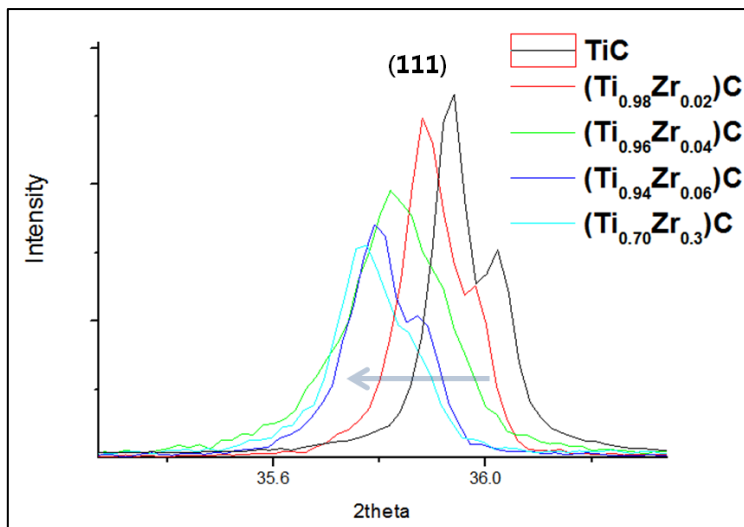


Figure 6. Peak shift of  $(\text{Ti}_{1-x}\text{Zr}_x)\text{C}$  in XRD ( $x=0 \sim 0.3$ )

#### 2.4.2. $\text{Ti}(\text{C}_{1-x}\text{A}_x)$ ( $x = \text{O or N}$ )

From Figure 7 to Figure 12, it shows the XRD and C/N/O analysis data with the content of A(oxygen or nitrogen) in  $\text{Ti}(\text{C}_{1-x}\text{A}_x)$  after carbothermal reaction. In Figure 7(a) it shows the XRD data of compositions covered from TiO to  $\text{Ti}(\text{C}_{1-x}\text{O}_x)$  and to TiC. As seen in Figure 7(a), if oxygen content( $x$ ) is above 0.5 then,  $\text{Ti}_2\text{O}_3$  oxide phase remained even after carbothermal reduction due to insufficient amount of carbon.  $\text{Ti}_2\text{O}_3$  is much more stable than TiO, TiC when the carbon is not enough for complete CO/ $\text{CO}_2$  reaction. [50] The reason of this intermediate oxide phases between titanium and oxygen are observed due to the positive activity deviation between TiC and TiO. That is, the oxide ( $\text{TiO}_2$ ) formation tendency is much stronger than oxycarbide phase above  $x=0.5$ , even TiO and TiC have same cubic crystal structure. Figure 7(b) is revealing the complete formation of only solid solution phase in the range of  $\text{Ti}(\text{C}_{0.6}\text{O}_{0.4}) \sim \text{Ti}(\text{C}_{0.9}\text{O}_{0.1})$ . Also lattice contraction is observed with linear (111) peak shift to high angle as seen in Figure 8. This contraction is due to the high bonding strength of stable Ti-O. Figure 9 shows the carbon and oxygen analysis after carbothermal reduction. Carbon and oxygen content is almost similar with the ideal content. That is, produced  $\text{Ti}(\text{C}_{1-x}\text{O}_x)$  shows almost same composition with target. Meanwhile, synthesis of any composition of  $\text{Ti}(\text{C}_{1-x}\text{N}_x)$  is possible due to strong negative activity deviation from ideal solution phase. Only complete  $\text{Ti}(\text{C}_{1-x}\text{N}_x)$  phase can be observed in Figure 10. Linear peak shift with composition in Figure 11 means a decrease of lattice parameter with the increase of N content in  $\text{Ti}(\text{C}_{1-x}\text{N}_x)$  phase. And the exact composition of carbon and nitrogen is shown in Figure 12 which means synthesis of accurate targeted composition. From this plots and Table 1, it is confirmed that successful synthesis of solid solution is accomplished above  $x=0.5$  in  $\text{Ti}(\text{C}_{1-x}\text{O}_x)$  and any  $x$  in  $\text{Ti}(\text{C}_{1-x}\text{N}_x)$  by high energy ball milling.



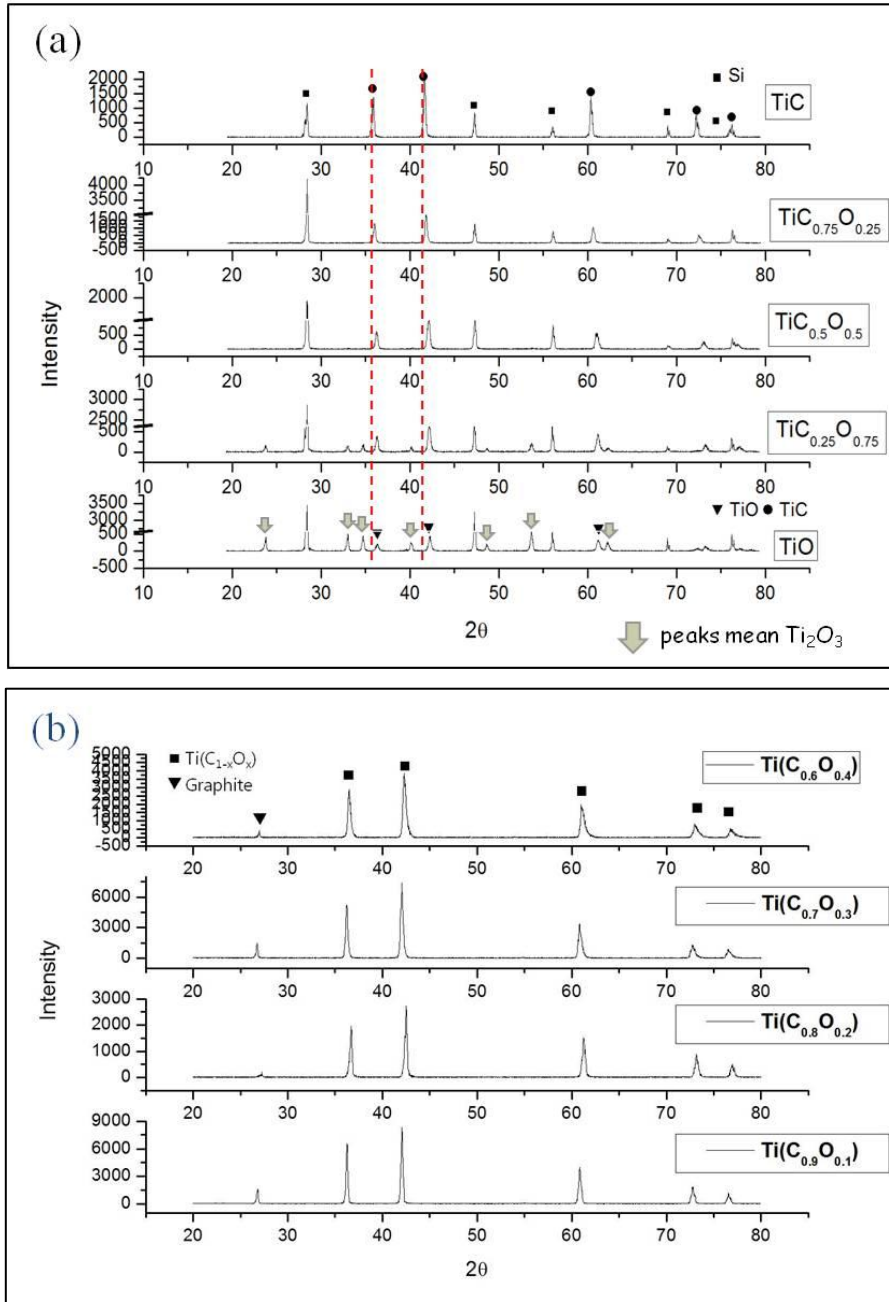


Figure 7. XRD result of  $\text{Ti}(\text{C}_{1-x}\text{O}_x)$  with oxygen content of (a)  $x=0\sim 1$ , (b)  $x=0.6\sim 0.9$

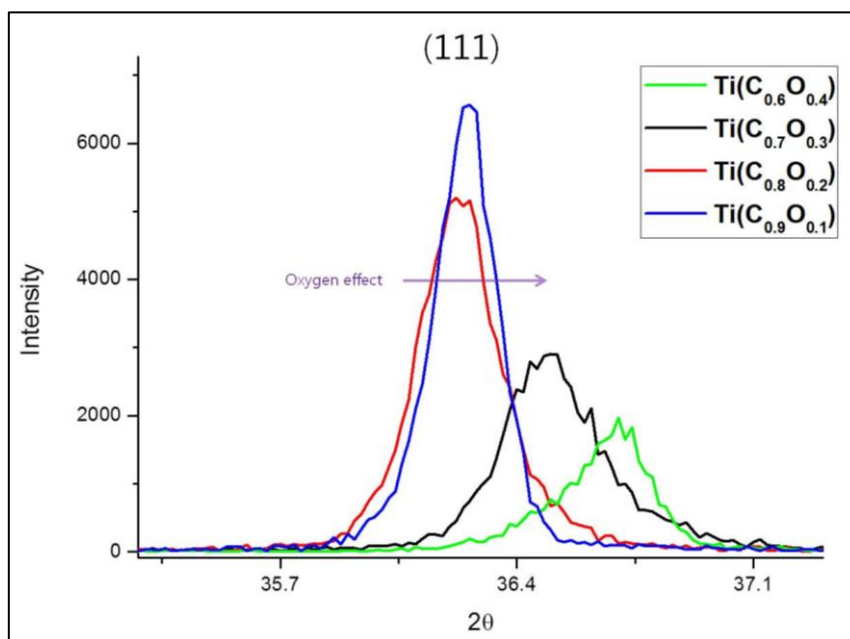


Figure 8. Peak shift of  $\text{Ti}(\text{C}_{1-x}\text{O}_x)$  in XRD with oxygen content of  $x=0.6\sim 0.9$

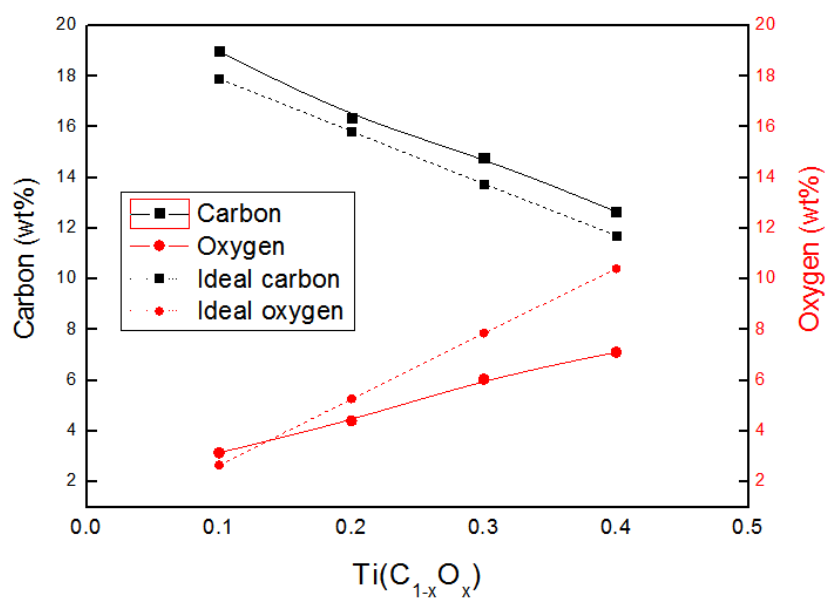


Figure 9. Carbon and Oxygen analysis of  $\text{Ti}(\text{C}_{1-x}\text{O}_x)$  with oxygen content of  $x=0.6\sim 0.9$

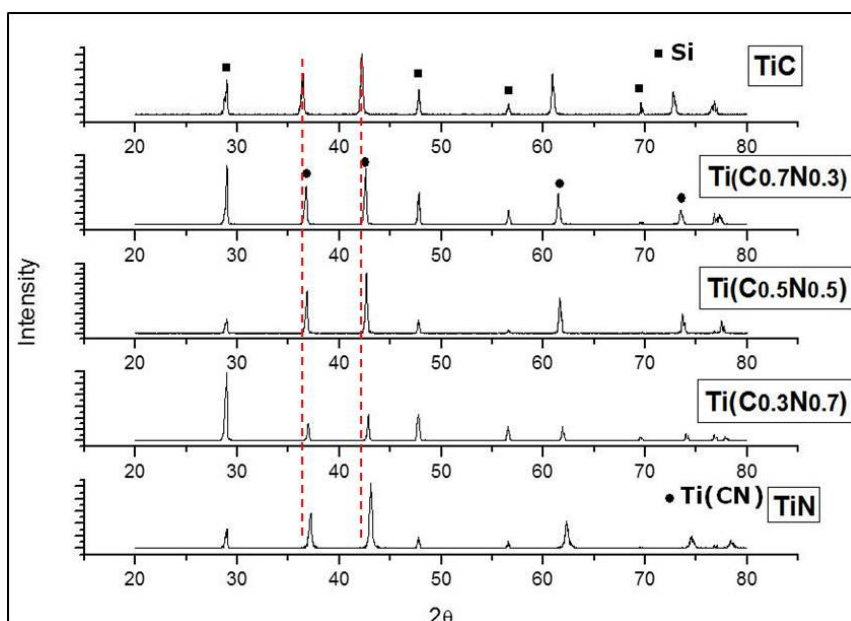


Figure 10. XRD result of  $\text{Ti}(\text{C}_{1-x}\text{N}_x)$  with nitrogen content

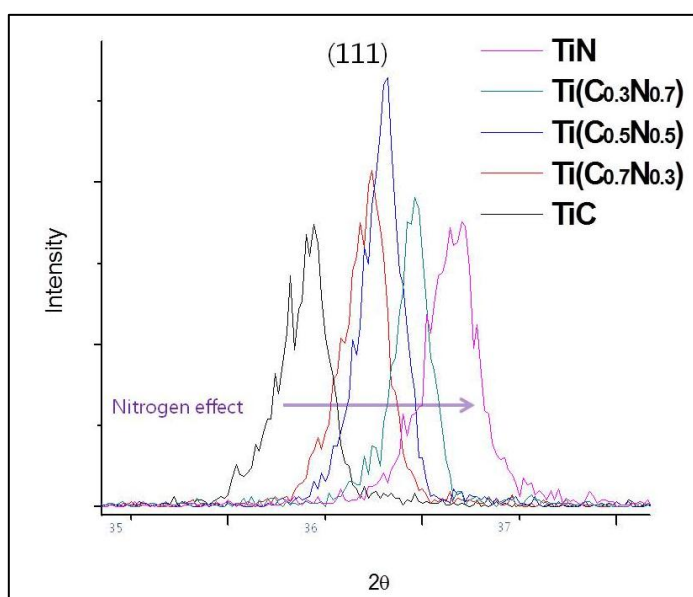


Figure 11. Peak shift of  $\text{Ti}(\text{C}_{1-x}\text{N}_x)$  with the content of nitrogen in XRD

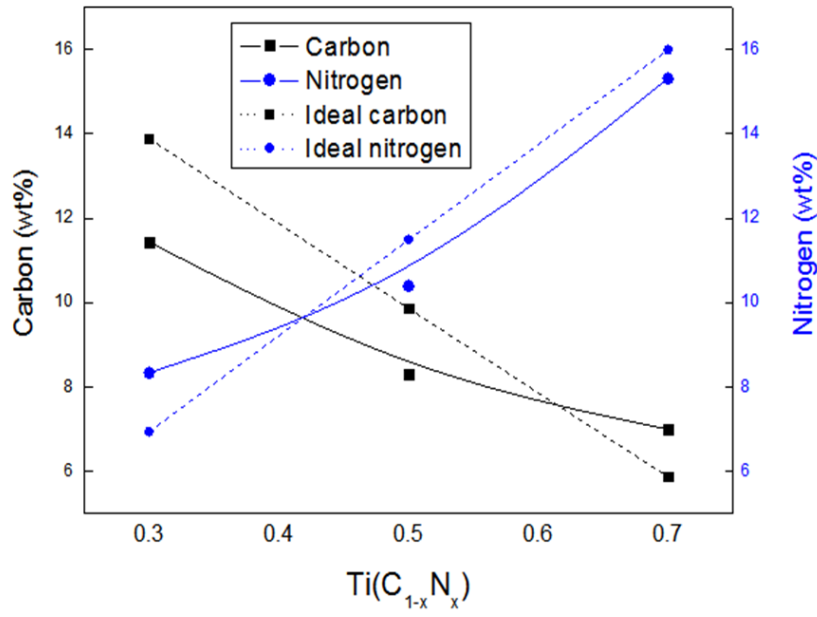


Figure 12. Carbon and Nitrogen analysis of  $\text{Ti}(\text{C}_{1-x}\text{N}_x)$

$\text{Ti}(\text{C}_{1-x}\text{O}_x)$		$\text{Ti}(\text{C}_{1-x}\text{N}_x)$	
Target	Real	Target	Real
$\text{Ti}(\text{C}_{0.6}\text{O}_{0.4})$	$\text{Ti}(\text{C}_{0.648}\text{O}_{0.273})$	$\text{Ti}(\text{C}_{0.7}\text{N}_{0.3})$	$\text{Ti}(\text{C}_{0.357}\text{N}_{0.670})$
$\text{Ti}(\text{C}_{0.7}\text{O}_{0.3})$	$\text{Ti}(\text{C}_{0.753}\text{O}_{0.231})$	$\text{Ti}(\text{C}_{0.5}\text{N}_{0.5})$	$\text{Ti}(\text{C}_{0.421}\text{N}_{0.452})$
$\text{Ti}(\text{C}_{0.8}\text{O}_{0.2})$	$\text{Ti}(\text{C}_{0.827}\text{O}_{0.167})$	$\text{Ti}(\text{C}_{0.3}\text{N}_{0.7})$	$\text{Ti}(\text{C}_{0.576}\text{N}_{0.364})$
$\text{Ti}(\text{C}_{0.9}\text{O}_{0.1})$	$\text{Ti}(\text{C}_{0.954}\text{O}_{0.118})$		

**Table 1.** Compositions of  $\text{Ti}(\text{C}_{1-x}\text{A}_x)$

## 2.5. Summary

From the above results, it is confirmed that successful synthesis of target composition is accomplished not only  $(\text{Ti}_{1-x}\text{W}_x)\text{C}$  and  $(\text{Ti}_{1-x}\text{Zr}_x)\text{C}$  within solubility limit but also  $\text{Ti}(\text{C}_{1-x}\text{O}_x)$  above  $x=0.5$  and  $\text{Ti}(\text{C}_{1-x}\text{N}_x)$  by optimized own high energy ball milling process. It means that rational tuning composition of raw precursor is possible and ready to see the effect of solid solution for chlorination process.

## III. CARBIDE DERIVED CARBON FROM TIC

### SOLID SOLUTION

#### 3.1. Introduction

The studies of CDC synthesized from solid solution carbide are very few. There is no research about the chlorination of  $(\text{Ti}_{1-x}\text{Me}_x)\text{C}$  due to the difficult synthesis and control of complete solid solution. Only few CDCs from solid solution are reported such as titanium oxycarbide[51], oxycarbonitride[52], SiCN.[22] Although Ostrovski studied chlorination of oxycarbide[51] and oxycarbonitride[52], they didn't synthesize complete solid solution phase due to the lack of controlling accurate composition, it resulting to study only pathway of chlorination with thermodynamic study. Recently Gogotsi[22] reported the organic-inorganic polymers with a backbone containing Si atoms, which is called polymer derived ceramics (PDCs) introduced as a raw materials for mesoporous CDC. It forms amorphous SiCN phase, in which nanocrystallites (such as SiC or  $\text{Si}_3\text{N}_4$ ) and free carbon (carbon not linked to Si atoms) can co-exist and the structure evolution occurs with pyrolysis temperature. But their process shows very limited composition and they didn't control complete SiCN [22] with atomic scale. In this way, there were few previous challenges about chlorination of solid solution phase but no significant results were found yet.

##### 3.1.1. Adsorption Isotherms

Gas adsorption is the phenomenon, when the concentration of gas at the surface has a higher concentration than in the bulk of the gas.[53] There are two adsorption types: physical adsorption (physisorption) and chemical adsorption (chemisorption). Physisorption, which does not involve chemical bonding, occurs for all gases and solid surfaces. It increases with increasing pressure and, as adsorption is always an exothermic process, with decreasing temperature. It must be distinguished from chemisorption, which involves the formation of direct chemical bonds between gas and

solid surface. Keeping the temperature constant and varying the external gas pressure, simultaneously recording the amount adsorbed at each pressure, one can obtain the adsorption isotherm. The adsorption isotherms can be used to analyze the surface area, pore volume, fluid-wall interaction strength, pore size distribution and other porous properties.

There are six principal types of isotherm shapes as seen in Figure 13(a).[2] Type I is the characteristic reversible isotherm of highly microporous materials, having relatively small external surfaces; it saturates at low relative pressures. The reversible Type II isotherm is typical for non-porous or macro-porous materials and it represents unrestricted monolayer-multilayer adsorption. The reversible Type III isotherm is not common and generally associated with weak adsorbent-adsorbate but strong adsorbate-adsorbate interactions. It is characteristic for adsorption on surfaces with low adsorption potential, like organic polymers. The Type IV isotherms resemble Type II, the difference is its hysteresis loop (see below) which is associated with capillary condensation taking place in mesopores and limiting uptake at high relative pressures. It is a typical isotherm for mesoporous materials. The Type V isotherm is uncommon, but obtained for some porous adsorbents, where the adsorbent-adsorbate interactions are exceptionally weak in comparison with adsorbate-adsorbate interactions. It is typical for water vapor adsorption on microporous carbons. The last Type VI isotherm represents stepwise multilayer adsorption on uniform non-porous surfaces. The step height represents the monolayer capacity and usually remains constant for two-three adsorbed layers.[54]

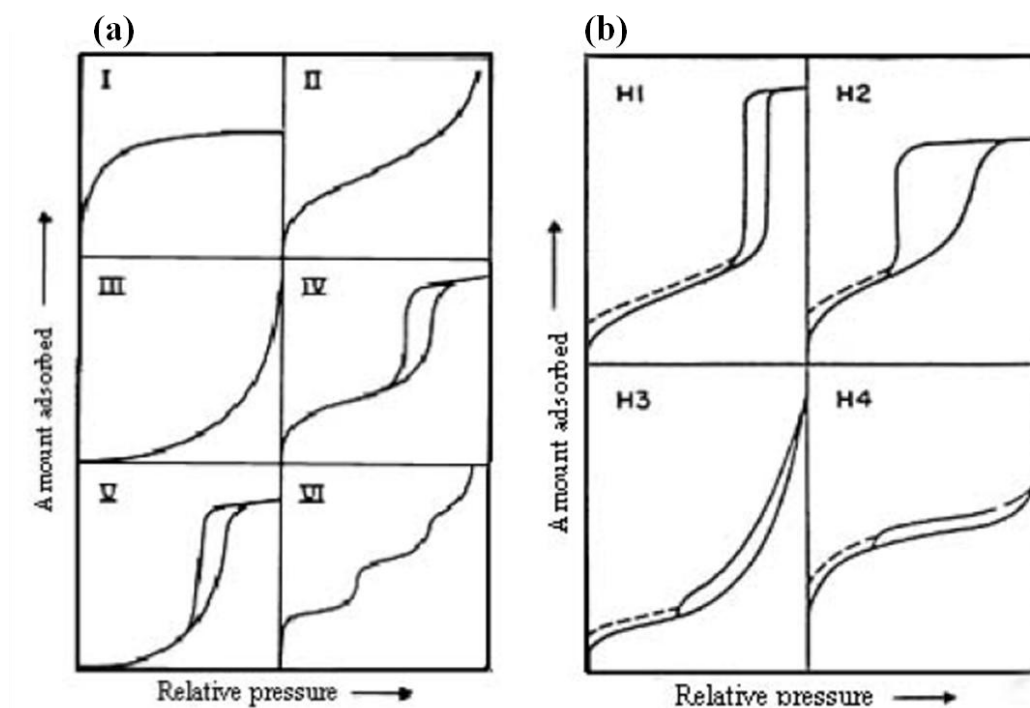


Figure 13. IUPAC classification of sorption isotherms.  $P/P_0$  represents the relative pressure and  $V$  represents the amount of gas adsorbed. (a) Classifications of different types of isotherms help in understanding the porous nature of solids. (b) Hysteresis of adsorption isotherms.

### 3.1.2. Hysteresis

The adsorption-desorption process on materials possessing mesopores is accompanied by the appearance of hysteresis loops as seen type IV in Figure 13(a). Adsorption hysteresis is said to occur when adsorption and desorption values deviate from each other. [54] This phenomenon has been extensively studied but its origin is still not fully understood and is usually attributed to thermodynamic or pore network effects: capillary condensation or evaporation in pores and existence of a network with different pore sizes which are emptied at different relative pressures[55]. IUPAC



distinguish between four types of hysteresis loops as Figure 13(b). The Type H1 and Type H4 are the two extreme cases. In the Type H1 hysteresis, the adsorption and desorption lines are almost vertical and parallel to each other over quite a narrow range of partial pressures. This is associated with materials with good pore connectivity and narrow pore size distribution.[56, 57] In the Type H4 hysteresis loop, adsorption and desorption lines are almost horizontal and parallel over a wide range of partial pressures. Recent experiments suggest that Type H4 hysteresis arises due to large mesopores embedded in the matrix of smaller pores[58]. The Types H2 and H3 are to some extent intermediate between these two extremes. It is necessary to note that the closure point of hysteresis loops at lower relative pressures is dependent on the nature of adsorptive, not the nature of adsorbent (e.g. for nitrogen at 77K the hysteresis loop is closing at  $p/p_0 \approx 0.42$ )[58]. The H2 type adsorption hysteresis is explained as a consequence of the interconnectivity of pores[59]. In such systems, the distribution of pore sizes and the pore shape is not well defined or irregular. A sharp step on the desorption isotherm is usually understood as a sign of interconnection of the pores. If a pore connected to the external vapor phase via a smaller pore, it will show H3 type. In many cases the smaller pore acts as a neck (often referred to as an "ink-bottle" pore[60]). In the cases when adsorption is expected to happen homogeneously over the entire volume of a porous material, desorption may happen by different mechanisms: percolation, i.e. the pore space is emptied progressively when the condition of emptying of the smallest pores, blocking the excess to the external gas phase, is fulfilled; cavitation, i.e. formation of gas bubbles in the pore interior. The latter corresponds to the condition of spinodal evaporation, when the limit of stability of the liquid is reached.

### 3.1.3. BET method

BET equation	$\frac{p}{V(p^o - p)} = \frac{1}{V_m c} + \frac{c-1}{V_m c} p / p^o$
$V$	amount adsorbed in volume STP (cm <sup>3</sup> /g) or in molar amount (mmol/g);
$V_m$	monolayer capacity in volume STP (cm <sup>3</sup> /g) or in molar amount (mmol/g);
$p$	equilibrium vapour pressure (P <sub>a</sub> );
$p^o$	saturation vapour pressure (P <sub>a</sub> );
$c$	average energy of adsorption ( $c = \exp [(\Delta H_A - \Delta H_L)/RT]$ );
$\Delta H_A$	heat of adsorption;
$\Delta H_L$	heat of liquefaction.
STP	Standard Temperature (25°C) and Pressure (1atm)

In 1938, Brunauer, Emmett and Teller reported the multilayer adsorption theory (BET theory). They extended the Langmuir's monolayer theory to multilayer adsorption. The derived equation is named the BET equation after the first letter of each of their names. The BET equation has been utilized in determining the monolayer volume of adsorbed gas, from which we can calculate the surface area of adsorbent. The BET method is based on several assumptions [54]: a) the surface is flat; b) all the surface sites have uniform energy, molecules in the first layer act as sites for molecules in the second and higher layers; c) the condensation and evaporation properties of all layers above the first are similar to the liquid adsorptive; d) there is no interaction between adsorbed molecules; e) the number of layers is unlimited[58].

BET surface areas were determined from the calculated isotherms by the same method used for treating experimental data.[61, 62] As seen in above equation, the BET analysis is performed by plotting

“ $x/V(1 - x)$ ” vs “ $x$ ”,

where  $x = P/P^0$  ( $P^0 = 1$  bar) and  $V$  is the volume of nitrogen adsorbed per gram of CDC

at STP. This analysis produces a curve typically consisting of three regions: concave to the x axis at low pressures, linear at intermediate pressures, and convex to the x axis at high pressures. Choosing the proper linear region can be somewhat subjective because often several pressure regions will give a roughly linear BET plot. The slope ( $[c - 1]/V_m C$ ) and y intercept ( $1/V_m C$ ) of this linear region give the monolayer capacity,  $V_m$ , that is then used to calculate the surface area from  $A = V_m \sigma_0 N_{AV}$  where  $\sigma_0$  is the cross-sectional area of the nitrogen at liquid density ( $16.2 \text{ \AA}^2$ ). Also it is possible to calculate the total pore volume too.  $V_p [\text{cm}^3/\text{g}]$  is converted to the volume liquid state as Equation (3.1). (In case that the relative pressure of last adsorption point is smaller than the set value, the total pore volume is to calculate from amount adsorbed of last adsorption point. )

$$V_p = V / 22414 \times M_g / \rho_a \quad (3.1)$$

( $V$ = adsorption volume,  $M_g$  = molecular weight of  $N_2$  and  $\rho_a$  = density of  $N_2$ )

#### 3.1.4. MP method

Micropore volume and PSD were traditionally evaluated using the t-plot [63],  $\alpha_s$  [64], MP(Micro Pore) [65] methods. Before explanation of MP method, it should be mentioned about t-plot method. Because both  $\alpha_s$  and MP methods are based on this t-plot. Adsorption amount depends on gas pressure, adsorption temperature, and properties of adsorptive gas and adsorbent solid. In a nitrogen adsorption isotherm measurement, temperature is constant and gas is limited, thus the isotherm changes according to the property of solid. However, in case of non-porous solid, although there is difference in adsorption amount, there is almost no difference in the shape of isotherm. In this case, plural isotherms can be expressed in one isotherm by standardizing adsorption amount as seen in Figure 14. This is the concept of standard isotherm. There are many ways of standardization, but the one that was suggested by Shull et al. is frequently used. In this method, adsorption amount is expressed by the

thickness of adsorption layer  $t$ , and the equation is as follows:

$$t = \frac{V_{ads}}{V_{mono}} * 0.354nm \quad (3.2)$$

By the way, the slope of  $t$ -plot decreases at a certain point. As can be seen in Figure 15, if the size of micropores is homogeneous, the plot will be on either of the two lines. In other words, the straight line from the origin should be bent sharply at the point when filling into micropores is complete. However, plots have curvature. This means that there is distribution in pore size. The  $t$ -plot method, which was invented by Lippens and de Boer, compares the above-mentioned standard isotherm and arbitrary isotherm. Standard isotherm shows the relationship between relative pressure and thickness of adsorption layer. Using standard isotherm, x-axis of isotherm that you wish to analyze can be changed from relative pressure to thickness of adsorption layer. Obtained  $t$ -plot can be divided into 3 types in broad term as seen in Figure 15. (These 3 different types of  $t$ -plot from (I) to (III) are shown above, but this categorization is just for the matter of convenience, and there is no type defined by IUPAC like in adsorption isotherm.) If  $t$ -plot is a linear curve that passes the original point like (I), it means that adsorption amount increased at the same rate as standard isotherm, and thus the adsorbent is considered to be non-porous material. Here, the increased adsorption amount when adsorption layer increases by one layer ( $t=0.354nm$ ) is equal to mono-molecular adsorption amount. Therefore, specific surface area as  $[m^2/g]$  can be calculated from the following equation with the slope of  $s$  in  $t$ -plot.

$$a_s = \frac{s \times 0.354}{22414} \times L \times \sigma = 1.541 \times s \quad (3.3)$$

Here,  $s$  means slope of  $t$ -plot.  $L$  is Avogadro constant and  $\sigma$  is cross sectional area of

adsorptive. If t-plot has 2 different slopes like (II) in Figure 15 that one of them is a sharp slope passing the original point and the other is more gradual slope, it means that the adsorbent has homogeneous sized micropores. In the early stage of adsorption, adsorption amount increases drastically due to adsorption into micropores (micropore filling) but the thickness of adsorption does not increase so much, as the result, the slope of t-plot becomes sharp. When adsorption into micropores is completed, adsorption happens only on the surface. As a result, the slope of the curve becomes gradual. At this point, whole surface area ( $a_1$ ) can be calculated by applying the slope of the linear curve L1 to equation (3.2). In the same manner, external surface area ( $a_2$ ) can be calculated by applying the slope of the other curve L2 to the equation. Pore surface area can be calculated by subtracting  $a_2$  from  $a_1$ . Pore volume can be obtained by converting the value of Y intercept of L2 to a volume under liquid condition. Furthermore, adsorption condition is considered to be like in the Figure 16(a) above at intersecting point of L1 and L2. Thus, doubled value of  $t$  (value  $2t$ ) is regarded as the average pore diameter. However, value  $2t$  gives wrong analysis results when pore size is only 2 layer or less. When  $2t$  value is smaller than 0.7nm, as it is micropore filling you can have rough idea whether the pores are big or small but there is no credibility in terms of numerical value. If t-plot draws a sharp straight line which begins from the original point but becomes smoother curve from some point like (III), the adsorbent is considered to have mesopores. The deviation from the linear curve is due to capillary condensation. Even in t-plot of this type, whole surface area can be measured from linear that passes the original point like in case of (I).

MP method measures distribution from the curvature of t-plot. In order to perform MP method analysis, t-plot has to be produced first. In Figure 16(b), the slope ( $s_2$ ) of the linear curve ( $L_2$ ), which connects the 2nd point and the 3rd point, is smaller than the slope ( $s_1$ ) of the linear curve ( $L_1$ ), which connects original point and the 1st point. This is because pores are filled with adsorbates. The surface area of pore can be expressed by the difference between  $a_1$  and  $a_2$ , which are both calculated by multiplying each

slope by 1.541 in eq.(3.3). Pore volume  $V_1$  (ml/g) can be calculated by multiplying  $a_1$  by thickness of adsorption layer. Thickness of adsorption layer used in this method is the average value of the thickness of 1st and 2nd layer ( $t_1$  and  $t_2$  respectively), so the following equation can be made.

$$V_1 = (a_1 - a_2) \times \frac{(t_1 + t_2)}{2} \quad (3.4)$$

Distribution curve can be obtained by carrying out the same calculation until the end point of t-plot and then plotting the obtained pore volume against the thickness of adsorption layer (average value).  $a_1$  in MP method is the surface area that is calculated from linear curve that passes the original point, and  $a_2$  is the one that is calculated from the other linear curve.  $V_p$  is an integrated value of pore volume, which can be obtained in above equation. Although it is not suitable for MP method analysis when pore size is below 0.7 nm, due to the same reason for the fact that average pore diameter is not accurate unless 2 or more adsorption layers are formed in pores as seen in Figure 16(a).

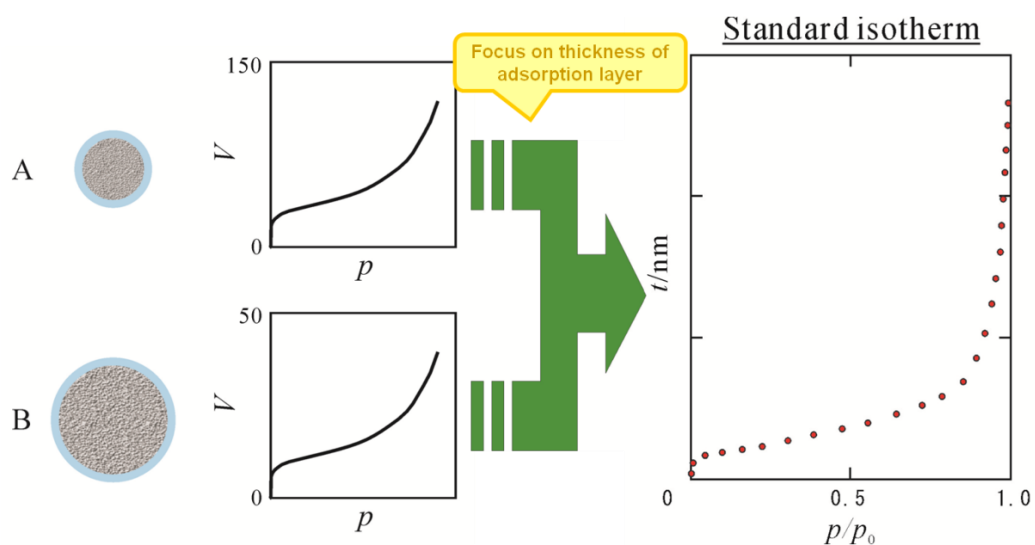


**Figure 14. Standardizing adsorption isotherm of non-porous solid with thickness of nitrogen**

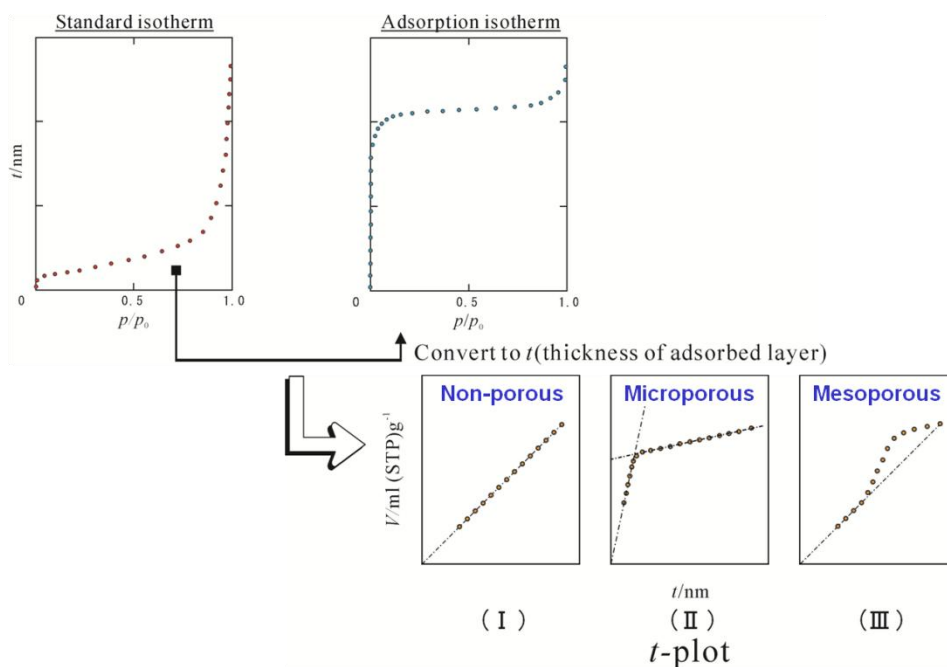


**Figure 15. 3 kinds of  $t$ -plots of adsorption volume ( $\text{cm}^3/\text{g}$ ) per thickness(nm) from the conversion between standard and sample isotherm**

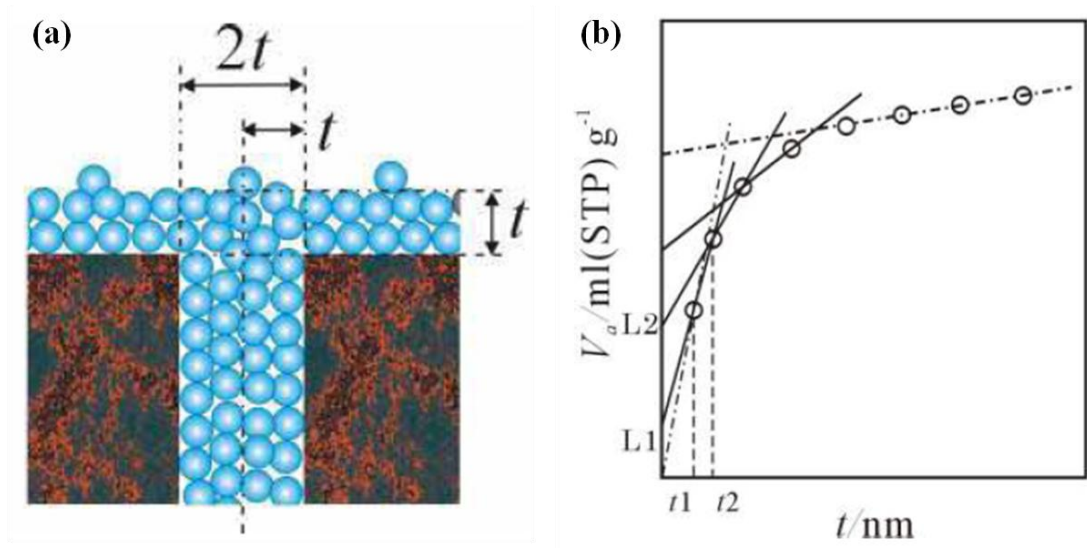


**Figure 16. (a) Schematic model of t-plot method (b) MP plot method**

### 3.1.5. BJH

The mesopore volume was obtained using the BJH (Barrett-Joyner-Halenda) method. In type IV adsorption isotherms in Figure 13(a), hysteresis occurs in adsorption and desorption processes. The hysteresis shape depends on the shape of mesopore. Whenever hysteresis exists, equilibrium adsorption amount at desorption is larger than the one at adsorption. This is because capillary condensation of nitrogen gas happens in mesopore and there is difference in meniscus between in adsorption process and in desorption process. There is an equation which represents the relationship between mesopore size and critical condensation pressure, Kelvin equation, and some analysis using Kelvin equation to calculate pore size distribution have been reported. Some of these methods are based on the assumption that the mesopores have cylinder shape. (Dollimore & Heal method, Cranston & Inkley method and etc.) Pore size distribution is calculated from desorption isotherm. In 1951, Barrett, Joyner and Halenda proposed



a method to evaluate pore size distribution. Pore curve is expressed as percentage change of pore volume ( $\Delta V_p / \Delta r_p$ ) against micropore radius ( $r_p$ ). In the area where capillary condensation is in presence, radius of cylinder shaped pore is sum of the thickness of adsorption layer at the arbitrary pressure ( $t$ ) and core radius ( $r^k$ ) of meniscus part.

$$r_p = t + r_k \quad (3.5)$$

Thickness of adsorption layer can be calculated from  $t$  curve of standard sample, and core radius can be calculated by Kelvin equation (3.6).

$$\ln \frac{p}{p_0} = - \frac{2\gamma V_L}{RT r_m} \quad (3.6)$$

Here,  $r_m$  is meniscus radius,  $\gamma$  is surface tension,  $V_L$  is molar volume of liquid adsorptive,  $R$  is gas constant and  $T$  is absolute temperature. In mesopore with cylinder shape, suppose meniscus radius at desorption is equal to core radius ( $r_k$ ), and if  $\gamma$  and  $V_L$  of nitrogen at liquid nitrogen temperature (77 K) are applied, the following equation can be obtained

$$r_m = 0.953 / \ln(p_0/p) \quad (3.7)$$

In very fine pores, having widths of the order of a few molecular diameters, the Kelvin equation could no longer remain strictly valid. Analytical methods based on the equation give a substantial margin of error when it is applied to calculation for pores below 1–1.5 nm. Consider a system of open ended cylindrical pores.

Assume that the relative pressure  $(p/p_0)_1$ , slightly lower than saturation vapor pressure and at the pressure all pores are filled with liquid.

As the pressure decreases, desorption occurs. When the pressure is reduced from  $(p/p_0)_1$  to  $(p/p_0)_2$ , a certain amount of gas,  $\Delta V_1$  is desorbed. The reduction in relative pressure result not only in emptying the largest pore of its capillary condensate, but also in a reduction in thickness of the physically adsorbed layer by the amount  $t_1$ .  $\Delta V_1$  and  $V_{p_1}$ , the volume of pores which has the largest pore radius  $r_{p_1}$  are expressed as

follows:

$$\Delta V_1 = \pi(r_{k1} + \Delta t_1)^2 L_1 \quad (3.8)$$

$$V_{p1} = \pi r_{p1}^2 L_1 \quad (3.9)$$

where  $L_1$  is the total length of first pore (pore radius :  $r_{p1}$ ). Thus  $V_{p1}$  can be expressed as follows:

$$V_{p1} = R_1 \Delta V_1 \quad (3.10)$$

Where  $R_1 = r_{p1}^2 / (r_{k1} + \Delta t_1)^2$ . When the pressure  $(p/p_0)_2$  is lowered to  $(p/p_0)_3$ ,  $\Delta V_2$  of gas is desorbed.  $\Delta V_2$  is not only that which comes from the second pore (pore radius:  $r_{p2}$ ) but also includes that from a second thinning of the physically adsorbed layer left behind in the first layer. If the volume which is released by this thinning is designated as  $V_{\Delta t2}$  then:

$$V_{p2} = R_2 (\Delta V_2 - V_{\Delta t2}) \quad (3.11)$$

where  $R_2 = r_{p2}^2 / (r_{k2} + \Delta t_2)^2$ . Inspection of the figure above shows that

$$V_{\Delta t2} = \pi L_1 (r_{k1} + \Delta t_1 + \Delta t_2)^2 - \pi L_1 (r_{k1} + \Delta t_1)^2 \quad (3.12)$$

Equation (3.12) is simple but in case that a greater number of pores are involved, such a calculation would become impractical. An alternative expression for  $V_{\Delta t2}$  is:

$$V_{\Delta t2} = \Delta t_2 \times A c_1 \quad (3.13)$$

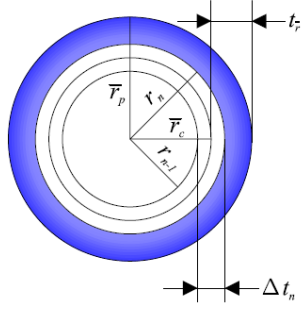
where  $A c_1$  is average area from which the physically adsorbed gas is desorbed.

Equation (3.13) can be generalized to express  $V_{\Delta m}$  when the pressure is lowered to  $(p/p_0)_n$  as follows:

$$V_{\Delta m} = \Delta t_n \sum_{j=1}^{n-1} A c_j \quad (3.14)$$

Generalizing equation (3.11) and substituting (3.14) for  $V_{\Delta m}$  yields:

$$V_{P_n} = R_n \Delta V_n - R_n \Delta t_n \sum_{j=1}^{n-1} A_{c_j} \quad (3.15)$$



(3.15) is complicated to carry out pore size distribution because  $A_c$  varies stepwise with each successive decrease in  $p/p_0$ . On the other hand  $A_p$ , the area of each pore, is a constant which can be calculated from its volume by the relationship  $A_p = 2V_p/r_p$ . It is obvious that using  $A_p$  for calculation is more practical. Figure left represents  $\Delta t_n$ , change in thickness of the physically

adsorbed layer of a previously emptied pore of radius  $\bar{r}_p$  during the  $n$ th desorption step. In a desorption step, capillary radius changes from  $r_{n-1}$  to  $r_n$ . The average value of  $r_{n-1}$  and  $r_n$  is  $\bar{r}_c$ . Although  $A_c$  in equation (3.15) varies actually before and after a desorption step, it can be represented using as follows:

$$A_c = A_p \times (\bar{r}_c / \bar{r}_p) \quad (3.16)$$

Also  $\bar{r}_c$  can be described as follows:

$$\bar{r}_c = \bar{r}_p - \bar{t}_r \quad (3.17)$$

where  $\bar{t}_r$  is the thickness of physically adsorbed layer at the corresponding value of  $(p/p_0)$ . Equation (3.15) can be rewritten as:

$$V_{p_n} = R_n \Delta V_n - R_n \Delta t_n \sum_{j=1}^{n-1} c_j A_{p_j} \quad (3.18)$$

Where,

$$c = (\bar{r}_p - \bar{t}_r) / \bar{r}_p \quad (3.19)$$

$$R_n = r_{pn}^2 / (r_{kn-1} + \Delta t_n)^2 \quad (3.20)$$

$c$  is a ratio of lateral area of two cylinders, one of which has a radius of  $\bar{r}_c$  and another has a radius of  $\bar{r}_p$ . Even in the same pore,  $c$  value varies according to thickness of the physically adsorbed layer, i.e.  $c$  depends on the pressure. But in the original paper, they insisted that there was no big deal of error if  $c$  was treated as a constant. Then they derived equation (3.21) from equation (3.18).

$$V_{pn} = R_n \Delta V_n - R_n \Delta t_n c \sum_{j=1}^{n-1} A_{pj} \quad (3.21)$$

They recommended using 0.75, 0.8, 0.85, 0.9 as  $c$  value to make calculation simple in their original paper. And they also recommended that  $c$  value should be selected according to a peak position of pore size distribution curve. Nowadays computers have developed and we can use equation (3.18) for pore size calculation without determining  $c$  value, which makes the calculation more accurate. Pore radius can be obtained from equation (3.5), pore volume can be calculated from equation (3.18) or (3.21). Pore size distribution curve can be yielded by plotting  $\Delta V/\Delta r$  against pore radius. By summing pore volume variation and plotting them against pore radius, cumulative pore volume curve can be obtained.

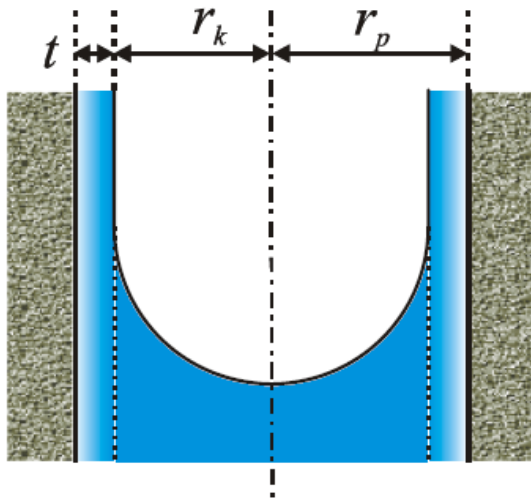


**Figure 17. Schematic diagram of capillary condensation for BJH method.**

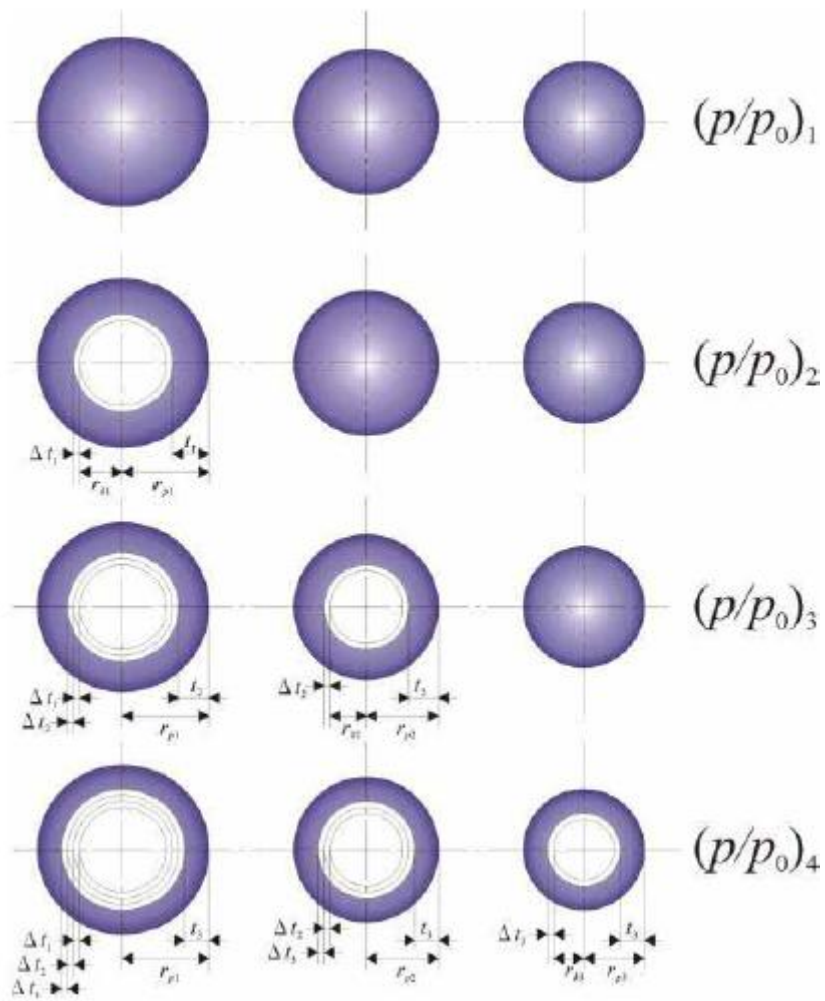


Figure 18. Schematic picture for understanding BJH method

### 3.1.6. Non-Local Density Functional Theory

As mentioned previously, mesopore and micropore are treated separately when characterizing porous materials by means of adsorption due to the limitations in the mathematical models used for extracting structural information from the isotherms, and in the description of pore-filling mechanisms for variable pore sizes. The dimensions of mesopores are traditionally calculated using the Kelvin equation, the micropore dimensions are calculated by t-method as written above. But in the use of models based on the density functional theory (DFT), which seem to give a better description of the adsorption in the pores, is increased, especially as it covers both meso- and micropores range.[5, 6, 66] Evans and Tarazon studied adsorption and phase of fluid in pores through molecular modeling based on DFT by using computers[67, 68] After that, Seaton *et al.* studied calculation of pore distribution based on DFT[69]. The pore distribution analysis based on the initial DFT provided satisfactory results to discuss adsorption status in pores. However, it has a problem about quantitative measurement in micropores.

This, the non-local density functional theory (NLDF) has been developed as new pore size distribution evaluation methods for porous materials. In contrast to classical thermodynamic methods for calculation of PSDs, the NLDF method is based on a statistical mechanics model, and calculations depend on the adsorbate-adsorbent system. The filling of micropores occurs in a continuous way, whereas the filling of mesopores occurs by pore condensation, which represents a first order transition from a gas-like state to a liquid-like state. For a material having both micropores and mesopores, the MP and BJH methods cannot accurately describe PSDs, and so we selected NLDF as a method of choice for determining the PSDs. PSD is calculated by equating the experimental isotherm to a combination of theoretical isotherms in individual pores (Eqn. 3.22). This equation, commonly referred to as the Generalized Adsorption Isotherm (GAI), assumes that the total isotherm consists of numerous individual single pore isotherms multiplied by their distribution,  $f(W)$  for a range of

pore sizes, min W to max W .

$$N_{\text{exp}}\left(\frac{P}{P^o}\right) = \int_{W_{\text{min}}}^{W_{\text{max}}} N\left(\frac{P}{P^o}, W\right) f(W) dW \quad (3.22)$$

where,

$N_{\text{exp}}\left(\frac{P}{P^o}\right)$  = experimental adsorption isotherm;

$W$  = pore width

$N\left(\frac{P}{P^o}, W\right)$  = kernel of theoretical isotherm of different pore width; and

$f(W)$  = pore size distribution.

The statistical mechanical model used in NLDFIT can be described as the best fit (non-negative least square algorithm) obtained by comparing the theoretical isotherms,  $N(P/P^o, W)$  for a particular adsorbate-adsorbent system to the experimental isotherm,  $N_{\text{exp}}(P/P^o, W)$ . The kernel,  $N(P/P^o, W)$  is obtained for different adsorbate-adsorbent system by either using NLDFIT or Monte Carlo simulation. In this work, the kernel obtained from the NLDFIT method is used for determining the pore size distribution. The weighted pore size of CDCs was determined using the following equation.

$$w_{\text{weighted}} = \frac{\sum_{i=1}^n w_i \cdot v_i}{\sum_{i=1}^n v_i} \quad (3.23)$$

where,

$w$  = pore width; and

$v$  = pore volume.

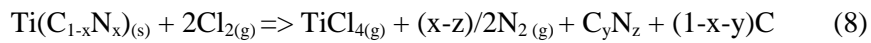


### 3.2. Experiment

The schematic experimental process is shown in Figure 19. CDC powders were produced by chlorination in quartz tube.  $(\text{Ti}_{1-x}\text{Me}_x)\text{C}$  and  $\text{Ti}(\text{C}_{1-x}\text{A}_x)$  powders were placed in a horizontal tube furnace (diameter 5cm), purged in argon flow, heated to 800 °C with a rate of 10 °C/min and exposed to chlorine gas(10sccm) for 3hours. After chlorination, additional annealing process at hydrogen atmosphere for 2hours in order to remove residual chlorine and chlorides trapped in pores. The oxygen and nitrogen content before and after chlorination was measured by XPS(X-ray Photoemission Spectroscopy) with SIGMA PROBE (ThermoVG, U.K). Pore structure analysis is used by nitrogen adsorption isotherms at low pressures (<1atm) with BELSORP-mini(Japan). Nitrogen at 77K is commonly used for determining adsorption properties of porous materials, although nitrogen gas can only access pores larger than 0.4 nm, and even for such size a restricted diffusion can be present due to the low temperature of the measurement. [70] But nitrogen is sufficient to analyze pore structure of CDC from the previous studies. The specific surface area was calculated using the Brunauer-Emmett-Teller(BET) method[61] from the nitrogen adsorption data in the relative range( $P/P^0$ ) of 0.05-0.30. The total pore volume was determined from the amount of  $\text{N}_2$  uptake at a relative pressure of  $P/P^0 = 0.995$ . And the MP method which is an extension of the de Boer's t-method was used for the calculation of micropore volume. Also Mesopore volume was derived from the adsorption branch of the isotherm based on the Barrett-Joyner-Halenda (BJH) model.[71] For analyzing pore size distributions, we used the non-local density functional theory (NLDFT) for  $\text{N}_2$  sorption assuming slit-shaped pores. It has been shown that  $\text{N}_2$  sorption gives reliable pore size and SSA values for pore diameters ranging between 0.5 and 40nm.[7, 72, 73] The chlorination of solid solution follows below reactions:



Reactions of (7), (8) show the formation of carbon dioxide<sub>[74]</sub> and carbon nitride<sub>[75]</sub> as below:



Reaction of (7) and (8) will be treated in chapter 4.

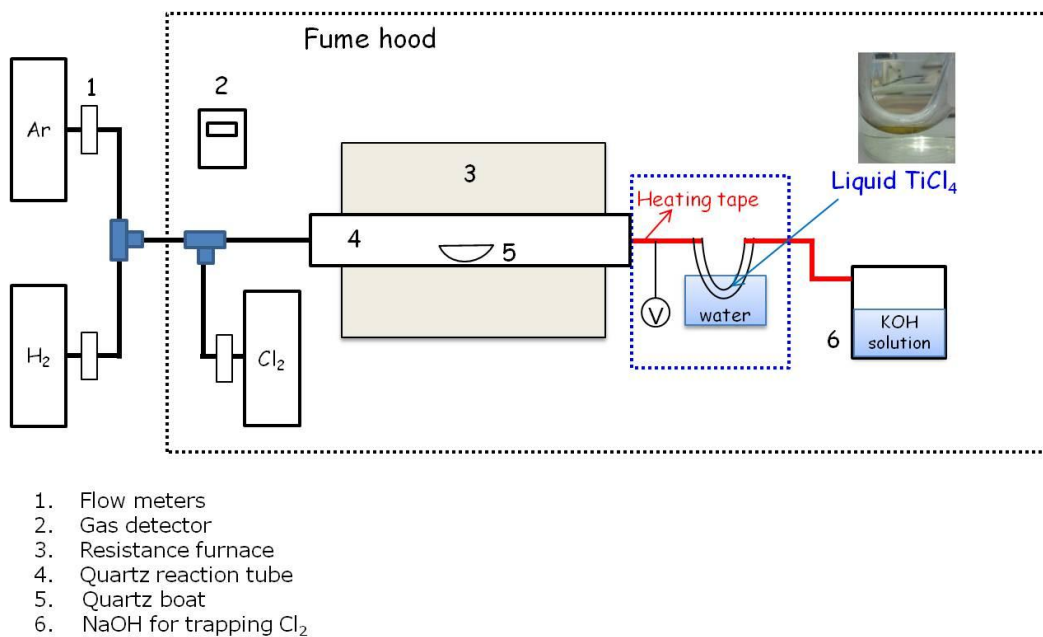


**Figure 19. Schematic of the experimental process of chlorination**

### 3.3. Result and discussion.

#### 3.3.1. $(\text{Ti}_{1-x}\text{Me}_x)\text{C-CDC}$ , (Me= W or Zr)

In Dash's thesis[76], it showed that the complete conversion of TiC to porous carbon took place at 400°C and complete chlorination of ZrC at 300°C. Even WC has higher chlorination temperature (800 °C)[77], our process of chlorination at 800 °C for 3hour is enough to complete conversion of all compositions of CDC. It shows almost same result with the Metal or content(x) of  $(\text{Ti}_{1-x}\text{Me}_x)\text{C-CDC}$  after chlorination at 800°C. As seen in Figure 20, all CDCs show type I adsorption isotherm which means micropore structure. And convergence of adsorbed volume at low pressure is same too. It means that the effect of  $\text{MeCl}_x$  phases (such as  $\text{TiCl}_4$  or  $\text{ZrCl}_4$  or  $\text{WCl}_x$ ) is not major factor to determine micropore structure during chlorination. Generally, CDC pore structure is depends on 3 kinds of factors: chlorination temperature, raw carbide structure, raw carbide composition which means  $\text{MeCl}_4$  effects. But there is still no exact explanation between pore properties and lattice parameter, initial carbide volume, kinds of metal.[1] Thus, below result in Figure 20 is meaningful because it is showing only  $\text{MeCl}_x$  effect in same cubic crystal structure during chlorination. This result will be used for the assumption of empirical simulation for the calculation of CDC structure in next chapter.

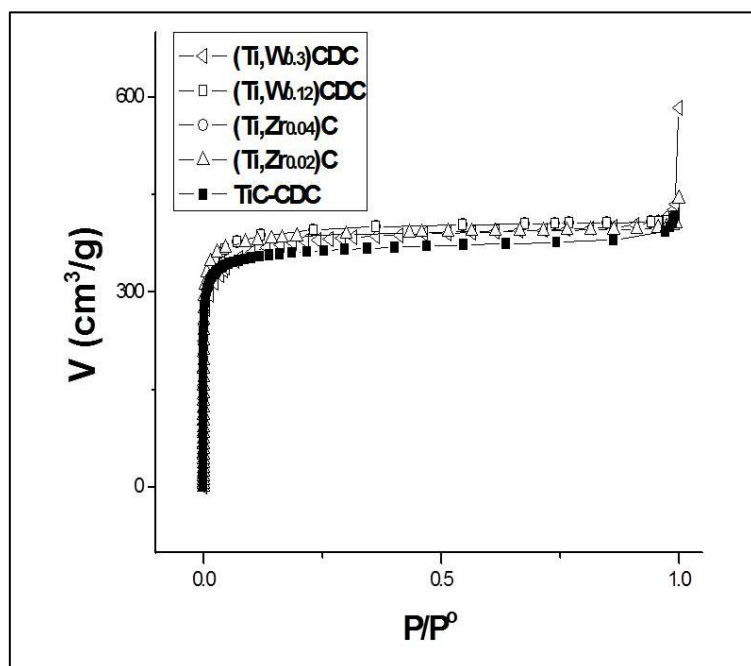


**Figure 20.** Nitrogen adsorption isotherms at 77K with x content of  $(\text{Ti}_{1-x}\text{Me}_x)\text{C-CDC}$  within solubility limit.

	TiC-CDC	$(\text{Ti}_{0.88}\text{W}_{0.12})\text{C}$ CDC	$(\text{Ti}_{0.7}\text{W}_{0.3})\text{C}$ CDC	$(\text{Ti}_{0.98}\text{Zr}_{0.02})\text{C}$ CDC	$(\text{Ti}_{0.96}\text{Zr}_{0.04})\text{C}$ CDC
SSA	1512.0	1563.8	1472.5	1549.8	1506.1
$V_{\text{mp}}$	0.623	0.666	0.631	0.651	0.614
$V_{\text{meso}}$	0.040	0.056	0.120	0.048	0.065
$V_{\text{total}}$	0.641	0.642	0.753	0.639	0.719

**Table 2.** Pore properties of  $(\text{Ti}_{1-x}\text{Me}_x)\text{C-CDC}$

### 3.3.2. Ti(C<sub>1-x</sub>A<sub>x</sub>)-CDC (A= O or N)

Previously, CDC from TiC has mainly narrow micropore distribution and Ti(C<sub>1-x</sub>O<sub>x</sub>)-CDC shows similar results too. In Figure 21, all isotherms of Ti(C<sub>1-x</sub>O<sub>x</sub>)-CDCs were of Type I in the Brunauer classification[2], which increases rapidly and converged at low pressure ( $P/P^0$ ), indicating the microporous structure. It shows definite oxygen effect during chlorination. From TiC-CDC, convergence of adsorption volume which means micropore filling is higher and higher with the increase of oxygen in Ti(C<sub>1-x</sub>O<sub>x</sub>). However, reverse result from Ti(C<sub>1-x</sub>N<sub>x</sub>)-CDC which exhibits a type IV isotherm can be observed in Figure 22. When this raw solid solution has low nitrogen content, Ti(C<sub>0.7</sub>N<sub>0.3</sub>), it shows both micropore filling and hysteresis of H4 type in Figure 13(b) after chlorination. As already mentioned in introduction, adsorption and desorption lines are almost horizontal and parallel over a wide range of partial pressures. Recent experiments suggest that Type H4 hysteresis arises due to large mesopores embedded in the matrix of smaller pores[58]. Ti(C<sub>0.5</sub>N<sub>0.5</sub>) shows H3 type hysteresis can be shown. It clearly means that nitrogen derived mesopores. In Figure 23, micro- and mesopore volumes are compared with x content of Ti(C<sub>1-x</sub>A<sub>x</sub>) at fixed 800°C chlorination temperature. All results in Table 3 are calculated from nitrogen adsorption isotherm of Figure 21 and 22. Ti(C<sub>1-x</sub>O<sub>x</sub>)-CDC shows significantly higher SSA and micropore volume than TiC-CDC. It shows noticeable SSA and pore volume results up to Ti(C<sub>7</sub>O<sub>3</sub>)-CDC: 3200m<sup>2</sup>/g, 1.55cm<sup>3</sup>/g of V<sub>micro</sub> (micropore volume) and 1.71cm<sup>3</sup>/g of V<sub>total</sub> (total pore volume). The surface area is an important characteristic of porous materials, especially for applications in adsorption separations and gas storage. For physisorption, the energetic interaction of guest molecules with surface atoms is usually much more important than guest-guest interaction, so it is expected that a higher surface area and micropore volume of material should correlate with a higher amount of adsorbed (per mass).[78]

Meanwhile, although low value of micropore volume is shown in Ti(C<sub>1-x</sub>N<sub>x</sub>)-CDC, much high mesopore volume value such as 1.67cm<sup>3</sup>/g of V<sub>meso</sub> (mesopore volume) and

1.9cm<sup>3</sup>/g of  $V_{\text{total}}$  were observed from Ti(C<sub>0.7</sub>N<sub>0.3</sub>)-CDC in Table 3. Also the formation of mesopore was maximized in Ti(C<sub>0.5</sub>N<sub>0.5</sub>)-CDC. The relatively low pore volume of Ti(C<sub>0.6</sub>O<sub>0.4</sub>)- and Ti(C<sub>0.3</sub>N<sub>0.7</sub>)-CDC is caused by partial collapse of pore structure due to the low carbon fraction in its structure. And specific surface area has same behavior with micropore volume in Figure 23. The highest SSA can get from Ti(C<sub>7</sub>O<sub>3</sub>)-CDC as mentioned above.

In Figure 24, pore size distribution (PSD) is plotted with oxygen content with Non-local density functional theory (NLDFT) assumed slit shaped pore.[79, 80] General CDC from TiC reported that it has mainly narrow micropore distribution at about 0.7nm[81] However, Ti(C<sub>1-x</sub>O<sub>x</sub>)-CDC shows broader pore size distribution than the former and 1.5nm sized micropore. We will suggest that it is derived by the CO/CO<sub>2</sub> formation and the wide distance between carbon atoms by the extraction of its sites in next chapter. Meanwhile, PSD of Ti(C<sub>1-x</sub>N<sub>x</sub>)-CDC can be seen in Figure 25. It shows good agreement with the mesopore formation in Figure 23. Average pore size increased with nitrogen content. Ti(C<sub>0.7</sub>N<sub>0.3</sub>) contains micropore below 1nm due to the high TiC fraction but significantly growth of mesopore formation with nitrogen content.

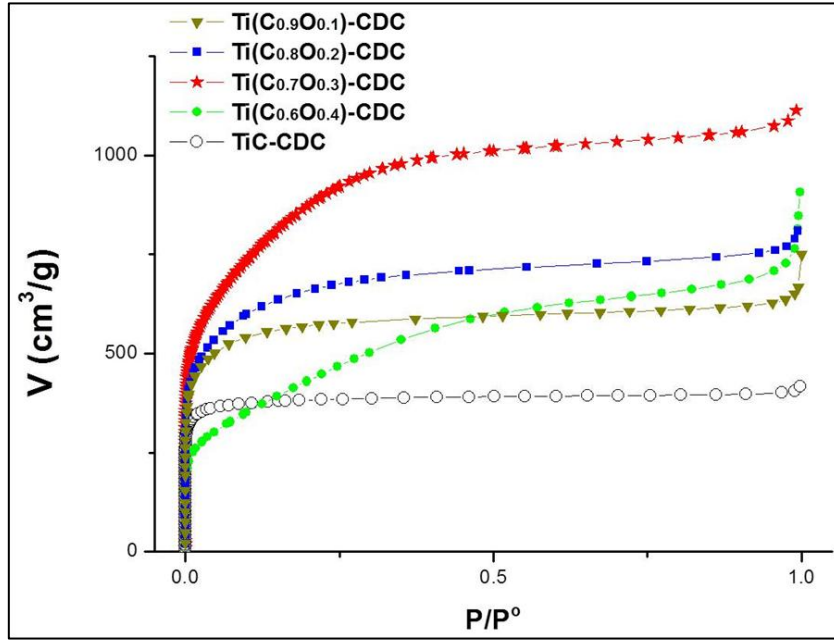


Figure 21. Nitrogen adsorption isotherms at 77K with oxygen content of  $\text{Ti}(\text{C}_{1-x}\text{O}_x)\text{CDC}$

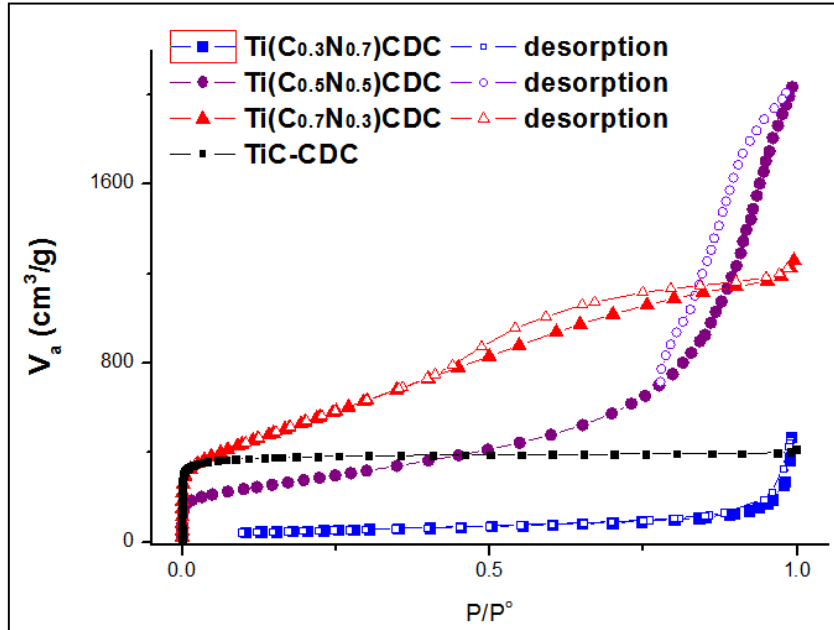
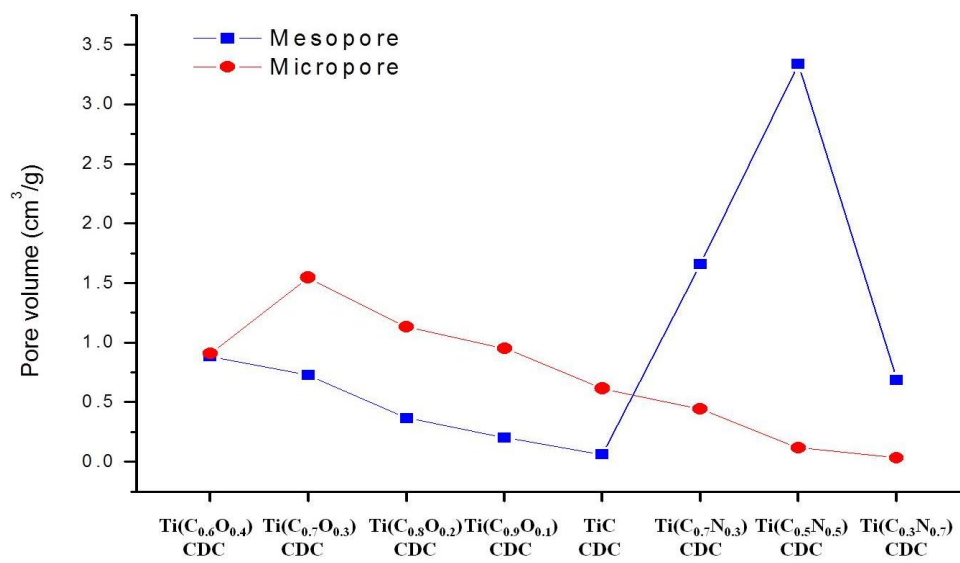


Figure 22. Nitrogen adsorption isotherms at 77K with nitrogen content of  $\text{Ti}(\text{C}_{1-x}\text{N}_x)\text{CDC}$



**Figure 23. Micro and meso pore volume of Ti(C<sub>1-x</sub>O<sub>x</sub>) and Ti(C<sub>1-x</sub>N<sub>x</sub>)**



	SSA	V <sub>mp</sub> (micro)	V <sub>BJH</sub> (meso)	V <sub>total</sub> (BET)
<b>Ti(C<sub>0.6</sub>O<sub>0.4</sub>)-CDC</b>	<b>1613.9</b>	<b>0.910</b>	<b>0.880</b>	<b>1.319</b>
<b>Ti(C<sub>0.7</sub>O<sub>0.3</sub>)-CDC</b>	<b>3113.4</b>	<b>1.548</b>	<b>0.725</b>	<b>1.716</b>
<b>Ti(C<sub>0.8</sub>O<sub>0.2</sub>)-CDC</b>	<b>2448.3</b>	<b>1.134</b>	<b>0.365</b>	<b>1.251</b>
<b>Ti(C<sub>0.9</sub>O<sub>0.1</sub>)-CDC</b>	<b>2207.7</b>	<b>0.952</b>	<b>0.204</b>	<b>1.055</b>
<b>TiC-CDC</b>	<b>1512.0</b>	<b>0.623</b>	<b>0.040</b>	<b>0.641</b>
<b>Ti(C<sub>0.7</sub>N<sub>0.3</sub>)-CDC</b>	<b>1213.2</b>	<b>0.441</b>	<b>1.659</b>	<b>1.962</b>
<b>Ti(C<sub>0.5</sub>N<sub>0.5</sub>)-CDC</b>	<b>522.1</b>	<b>0.033</b>	<b>3.337</b>	<b>3.453</b>
<b>Ti(C<sub>0.3</sub>N<sub>0.7</sub>)-CDC</b>	<b>183.1</b>	<b>0.012</b>	<b>0.685</b>	<b>0.723</b>

**Table 3. Summary of pore properties of Ti(C<sub>1-x</sub>A<sub>x</sub>) chlorinated at 800°C**

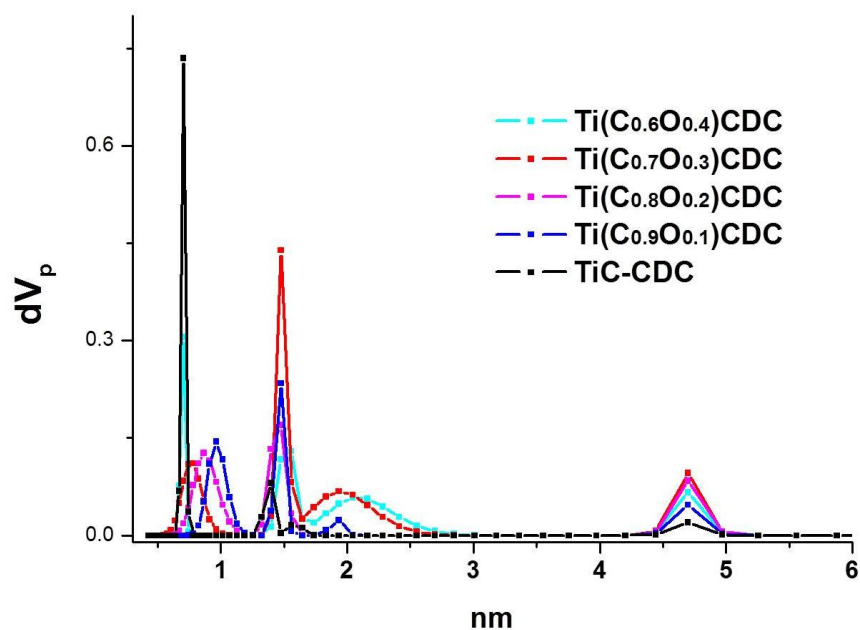


Figure 24. Pore size distribution of  $\text{Ti}(\text{C}_{1-x}\text{O}_x)$  calculated by NLDFT.

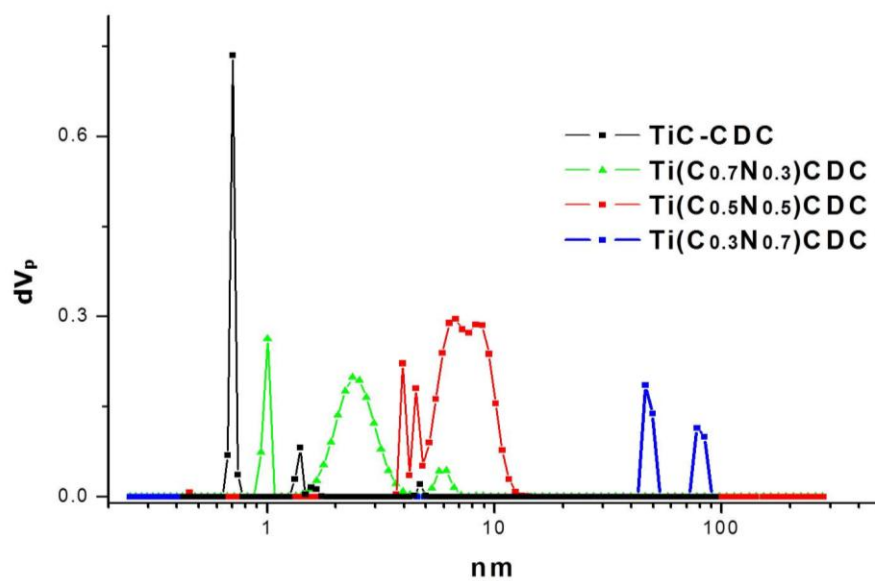


Figure 25. Pore size distribution of  $\text{Ti}(\text{C}_{1-x}\text{N}_x)$  calculated by NLDFT.

### 3.4. Summary

These results demonstrate that pore structure changed with the composition of solid solution such as  $(\text{Ti}_{1-x}\text{Me}_x)\text{C}$  and  $\text{Ti}(\text{C}_{1-x}\text{A}_x)$  after chlorination. Although  $(\text{Ti}_{1-x}\text{Me}_x)\text{C}$ -CDC didn't show any significant results between different metals in TiC, it can be used basic data for analysis of relationship between  $\text{MeCl}_4$  and pore structure of CDC. Also it was demonstrated that  $\text{Ti}(\text{C}_{1-x}\text{A}_x)$ -CDCs from solid solution phase are a great material to control pore structure covered from micro- to mesopores. Thus, it is enabling precise tuning of pores, and possibly having use in a wide range of pore applications. Even if CDC synthesized from same cubic crystal structure of  $\text{Ti}(\text{C}_{1-x}\text{A}_x)$  and temperature, it shows inverse results about pore volume, size with selection of only A atom in TiC. They have significantly higher properties than previously reported results such as pore volume and SSA.

## **IV.MECHANISM OF SOLID SOLUTION CARBIDE DERIVED CARBON**

### **4.1. Introduction**

The schematic layout of the process is depicted in Figure 26, micropore or mesopore formation could be possible either way with the only atom selection between oxygen and nitrogen. As shown in Figure 26,  $\text{TiO}_2$  and graphite carbon mixed and milled with high energy ball milling as mentioned previous chapter. Complete  $\text{Ti}(\text{C}_{1-x}\text{O}_x)$  phase is synthesized by carbothermal reaction in vacuum atmosphere in contrast  $\text{Ti}(\text{C}_{1-x}\text{N}_x)$  phase is from reaction in nitrogen atmosphere. Oxygen (red ball) in TiC is expected to react with carbon for  $\text{CO}/\text{CO}_2$  formation after extraction of titanium (blue ball). And nitrogen (green ball) in TiC which has a reaction with carbon for  $\text{C}_y\text{N}_x$  gas may derive mesopores finally. In this chapter, it will be shown the experimental results to support this micropore and mesopore formation mechanism.

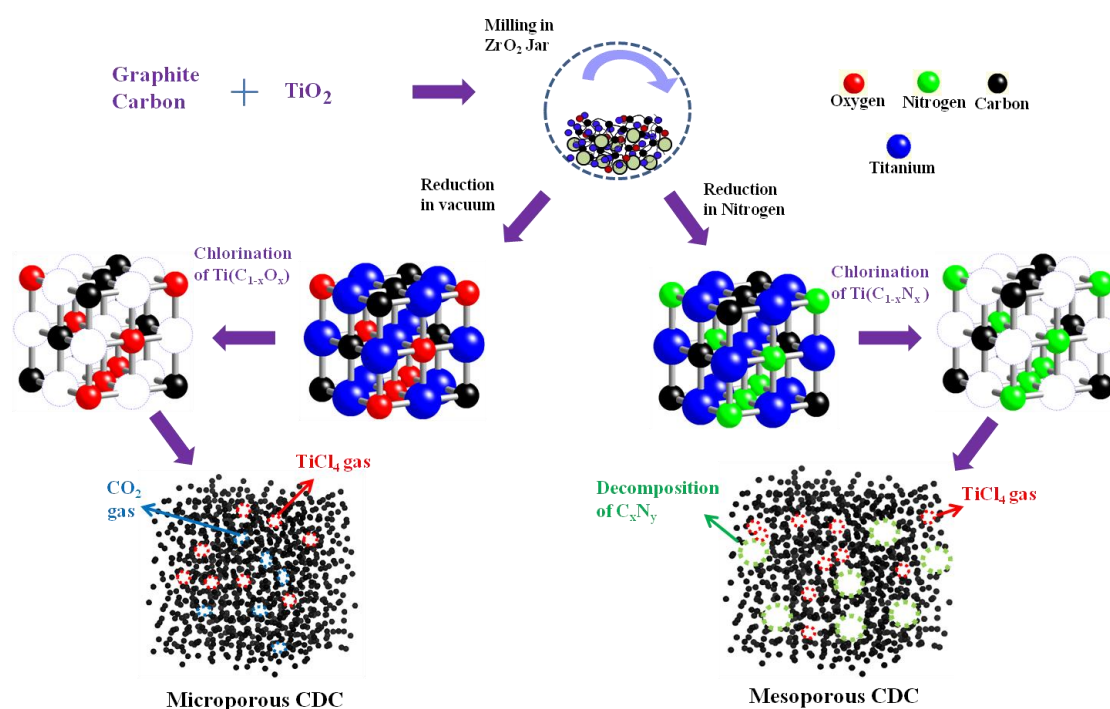


Figure 26. Schematic of the synthesis steps for a  $\text{Ti}(\text{C}_{1-x}\text{A}_x)\text{-CDC}$  powders, with a proposed schematic process.

## 4.2. Result and Discussion of $\text{Ti}(\text{C}_{1-x}\text{A}_x)\text{-CDC}$ ( $x = \text{O}$ or $\text{N}$ )

To understand the mechanism of pore formation, composition of  $\text{Ti}(\text{C}_{0.7}\text{O}_{0.3})\text{-}$ ,  $\text{Ti}(\text{C}_{0.7}\text{N}_{0.3})\text{-CDC}$  is fixed and compared with chlorination temperature in Figure 28 which is calculated from Figure 27. In the case of  $\text{Ti}(\text{C}_{0.7}\text{O}_{0.3})\text{CDC}$ , the evolution of micropore is dominantly observed until  $800^\circ\text{C}$  in Figure 28(a), finally it decreased at  $1000^\circ\text{C}$  due to the graphitization which means the inaccessible to nitrogen gas. Figure 28(a) also outperforms the benchmark  $\text{TiC-CDC}$  chlorinated at the same temperature. During the chlorination,  $\text{CO}$  and  $\text{CO}_2$  formation reaction can be proceeded after extraction of titanium due to the oxygen source in  $\text{Ti}(\text{C}_{1-x}\text{O}_x)$ . [51] According to the detailed calculation based on Thermodynamics [82],  $\text{CO}_2$  and  $\text{CO}$  gases prevail only at  $<600\text{K}$  and  $>1400\text{K}$ , respectively in an equilibrium condition, while  $\text{CO/CO}_2$  gas mixture exists together between this temperature range. [83] Molecular diameter calculated from van der Waals constant of  $\text{O=C=O}$  is only about  $0.51\text{nm}$  [84] which is smaller diameter than titanium tetrachloride ( $0.8\text{nm}$ ). [85] During chlorination, slit shaped micropore which is below  $2\text{nm}$  is derived by  $\text{CO/CO}_2$  and  $\text{TiCl}_4$  gas formations when these gas molecules flow out from CDC structure. It means that  $\text{CO/CO}_2$  reaction helps formation of micropore, it leads higher SSA and micropore volume than  $\text{TiC-CDC}$  as seen in Figure 28(a). Also the growth of mesopore volume at the expense of micropore volume is shown at  $1000^\circ\text{C}$ . This behavior is agree well from Chmiola's study, chlorination temperature in the range of  $400\sim 800^\circ\text{C}$ , creates new micropores, but above this temperature, the increase of mesopore volume which is larger than  $2\text{nm}$  comes at the expense of smaller micropores. [86]. Meanwhile, in Figure 28(b),  $\text{Ti}(\text{C}_{0.7}\text{N}_{0.3})\text{-CDC}$  has almost same values of micro- and mesopore volume compared with  $\text{Ti}(\text{C}_{0.7}\text{O}_{0.3})\text{-CDC}$  below  $600^\circ\text{C}$ . Finally, it shows significantly high mesopore volume at  $800^\circ\text{C}$  chlorination with the convergence of micropore volume value. The reason of this curious inversion tendency can be explained by the difference of reaction between  $\text{CO/CO}_2$  gas formation and partial decomposition of  $\text{C}_x\text{N}_y$  gas. General CDC structure is assumed to form by local re-bonding of each carbon atom in the carbide

with a close neighboring atom when metal(Ti) atoms are removed from their structure sites by chlorine.[87] That is, active C and A(O or N) atoms were formed bonding after extraction of metal. And the atomic distance between C and A atom was small enough to ensure the rearrangement and re-bonding. Then, carbon (di)oxide or carbon nitride could be formed. CO<sub>2</sub> gas immediately flow out, by contrast, C<sub>x</sub>N<sub>y</sub> solid phase remained in CDC structure. But synthesized carbon nitride during chlorination is reported to even partially decompose above 650°C due to its low stability.[75] It is expected that huge mesopore formation derived by decomposition of C<sub>y</sub>N<sub>x</sub> solid phase at 800°C chlorination temperature as shown in Figure 28(b). As the evidence, the case of 400°C chlorination shows only liquid TiCl<sub>4</sub> in the back side of the line after chlorination while chlorination at 800°C contains residual yellow solid as seen in Figure 29. From the XRD, this residual solid consists of TiNCl, C<sub>2</sub>H<sub>4</sub>ClN<sub>6</sub>, ClCN phases which contain nitrogen. Also Figure 30 and Figure 31 shows XPS results of Ti(C<sub>1-x</sub>A<sub>x</sub>)-CDC at 400°C and 800°C after chlorination. CDCs still contain oxygen or nitrogen after chlorination at 400°C. In Figure 31(a), the C 1s can be deconvoluted in to two lines peaked at 284.5 and 287.05 eV. By comparing with sp<sup>3</sup> binding energy (286.9 eV) [88] and pyridine (C<sub>5</sub>H<sub>5</sub>N, sp<sup>2</sup> binding energy: 285.5 eV) [89], the carbon peak at 287.05 and 284.5 eV are assigned due to sp<sup>3</sup> and sp<sup>2</sup> bondings, respectively. The N 1s also can be deconvoluted in to two lines peaked at 397.6 and 399.4 eV. These two peaks are attributed to sp<sup>2</sup> N, i.e. substitutional N in the graphite sheet [90, 91]. However, in Figure 31(b), nitrogen atoms in CDC existed as quaternary nitrogen (400.8 eV), pyridinic nitrogen (398 eV), and nitrogen oxide (402.5 eV) [92] but nitrogen content significantly decreased after 800°C chlorination. It means that oxygen and nitrogen definitely effect to the pore structure formation. Finally, mass spectrometer of C<sub>2</sub>N<sub>2</sub> in helium atmosphere shows clear evidence of C<sub>x</sub>N<sub>y</sub> existence with Figure 32(c), C<sub>2</sub>N<sub>2</sub> flows out around 600°C only in Ti(C<sub>0.5</sub>N<sub>0.5</sub>)CDC chlorinated at 400°C, it shows the difference with Figure 32 (a),(b). All of these data can prove that mesopore is derived by the decomposition of C<sub>x</sub>N<sub>y</sub> phase during chlorination.

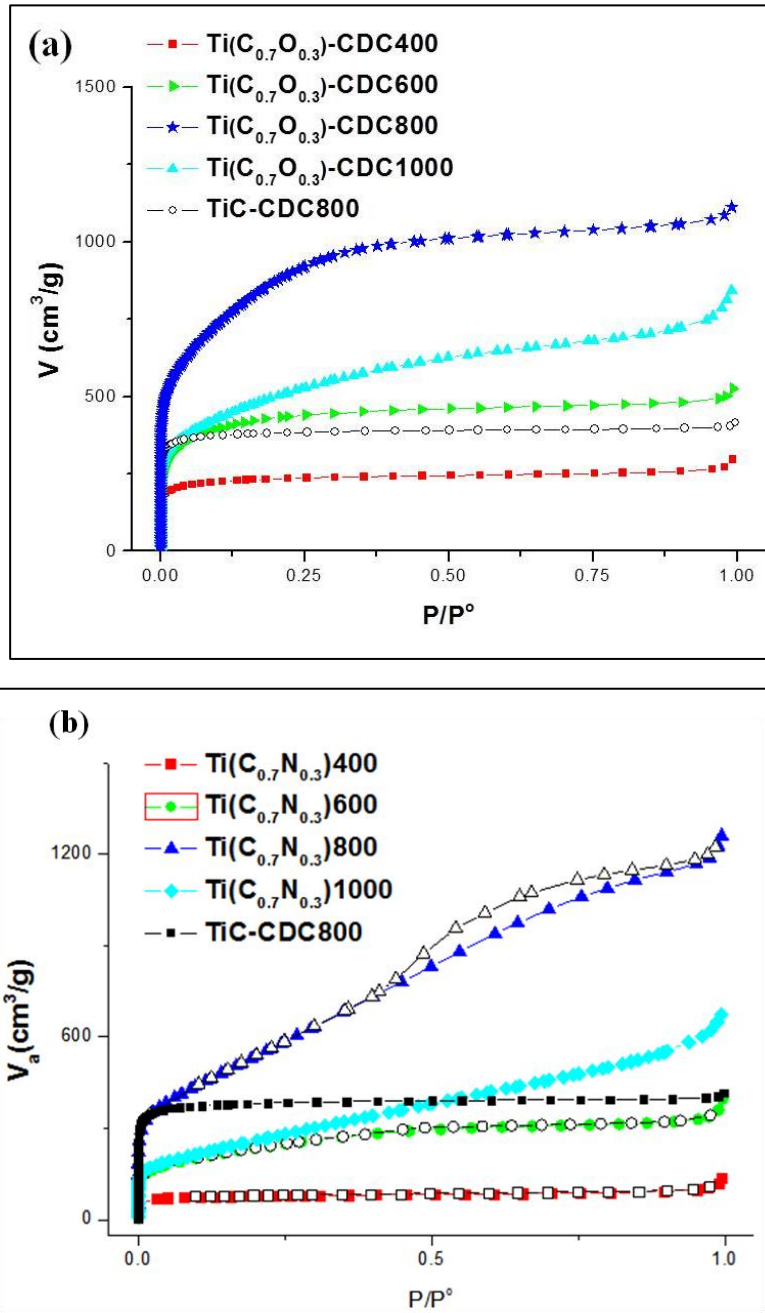
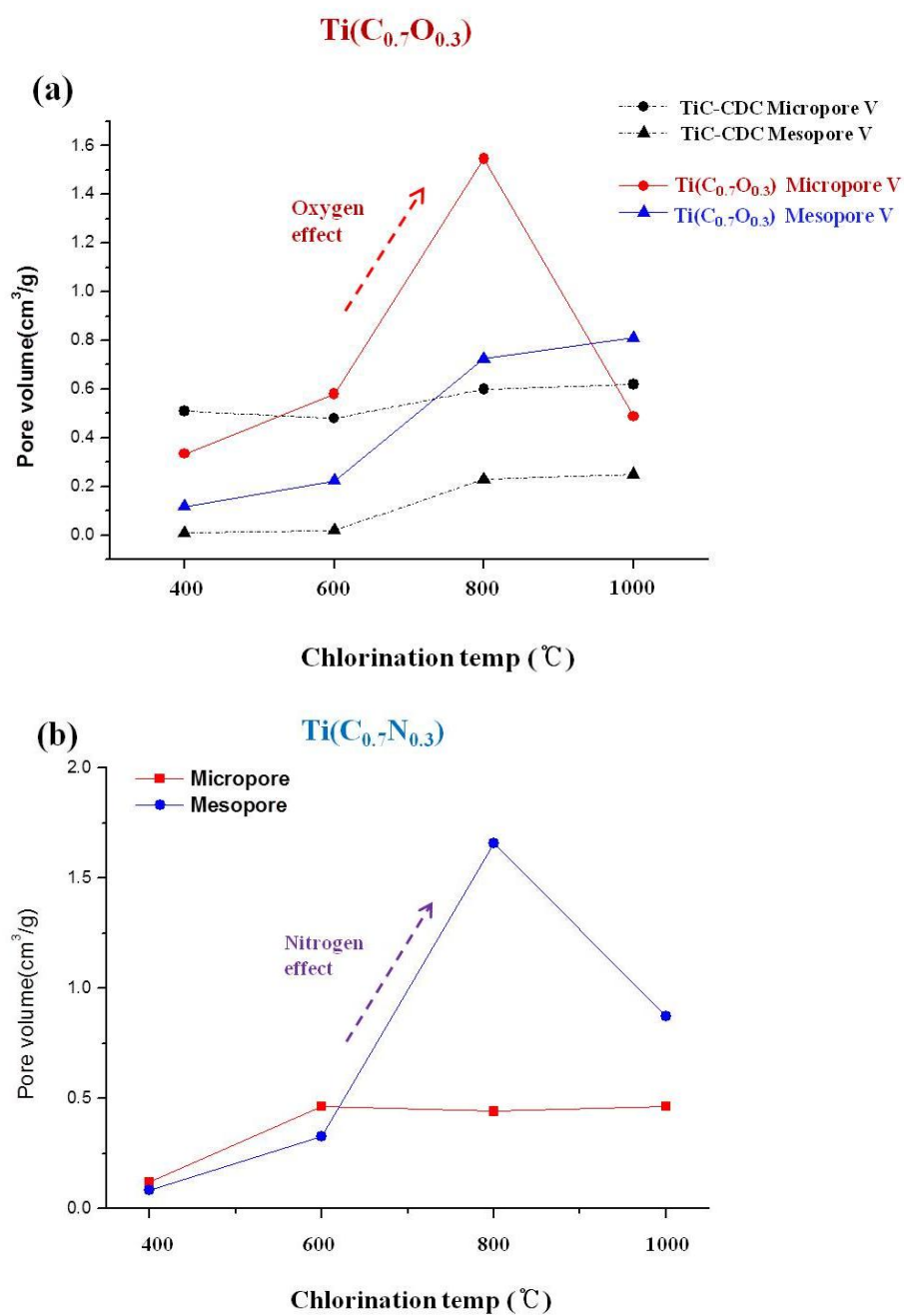


Figure 27. Nitrogen adsorption isotherms at 77K with chlorination temperature of  
 (a) $\text{Ti}(\text{C}_{0.7}\text{O}_{0.3})\text{CDC}$  (b) $\text{Ti}(\text{C}_{0.7}\text{N}_{0.3})\text{CDC}$





**Figure 28. Micro/meso-pore volume of (a) Ti(C<sub>0.7</sub>O<sub>0.3</sub>)-CDC, (b) Ti(C<sub>0.7</sub>N<sub>0.3</sub>)-CDC with chlorination temperature. Results of TiC-CDC is from reference [76]**

<b>Ti(C<sub>0.7</sub>O<sub>0.3</sub>)-CDC</b>	<b>400°C</b>	<b>600°C</b>	<b>800°C</b>	<b>1000°C</b>
<b>SSA</b>	905.3	1628.6	3113.4	1813.7
<b>V<sub>mp</sub> (micro)</b>	0.334	0.581	1.548	0.489
<b>V<sub>BJH</sub> (meso)</b>	0.118	0.224	0.725	0.811
<b>V<sub>total</sub> (BET)</b>	0.452	0.806	1.716	1.300

**Table 4. Summary of pore properties of Ti(C<sub>1-x</sub>O<sub>x</sub>) with chlorination temperature**

<b>Ti(C<sub>0.7</sub>N<sub>0.3</sub>)-CDC</b>	<b>400°C</b>	<b>600°C</b>	<b>800°C</b>	<b>1000°C</b>
<b>SSA</b>	299.2	837.6	1213.2	852.
<b>V<sub>mp</sub> (micro)</b>	0.122	0.463	0.441	0.462
<b>V<sub>BJH</sub> (meso)</b>	0.082	0.328	1.659	0.875
<b>V<sub>total</sub> (BET)</b>	0.193	0.565	1.962	1.044

**Table 5. Summary of pore properties of Ti(C<sub>1-x</sub>N<sub>x</sub>) with chlorination temperature**

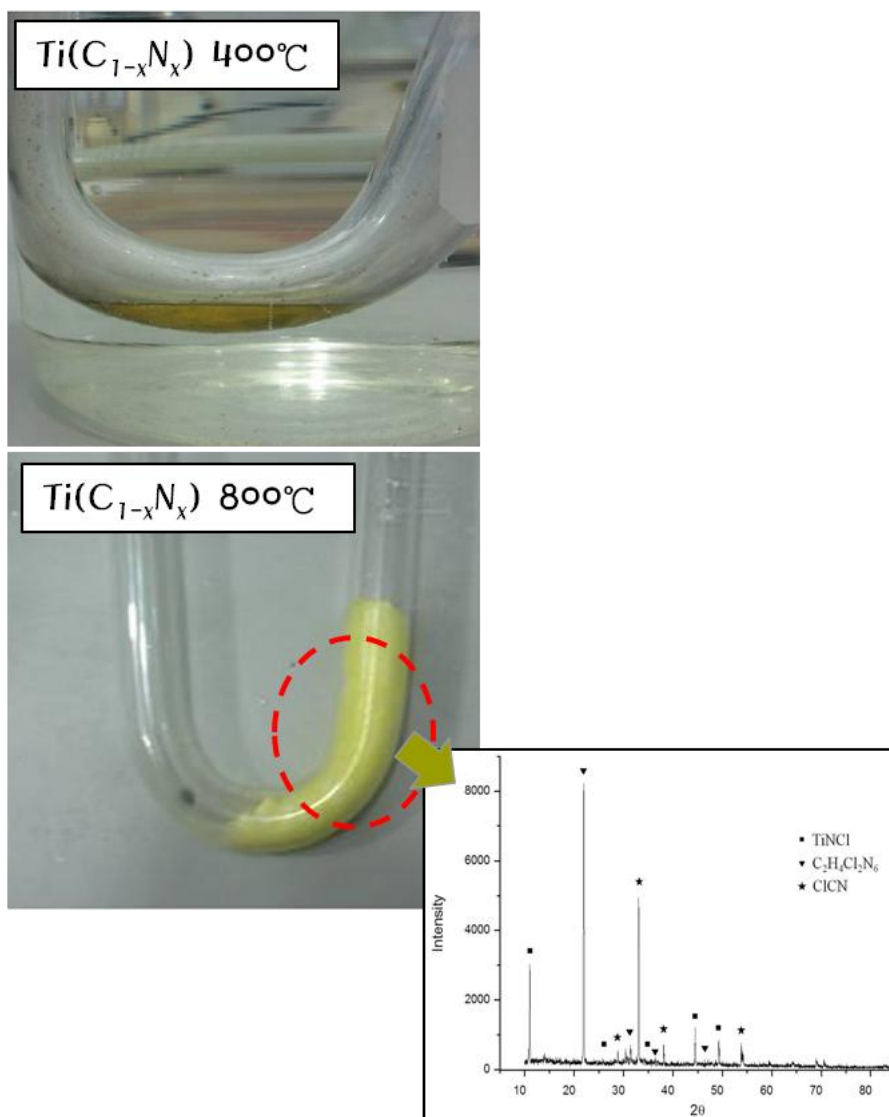


**Figure 29. The difference of  $Ti(C_{1-x}N_x)$  with chlorination temperature between 400 °C and 800°C, XRD result of yellow residual solid phase from 800°C chlorination.**

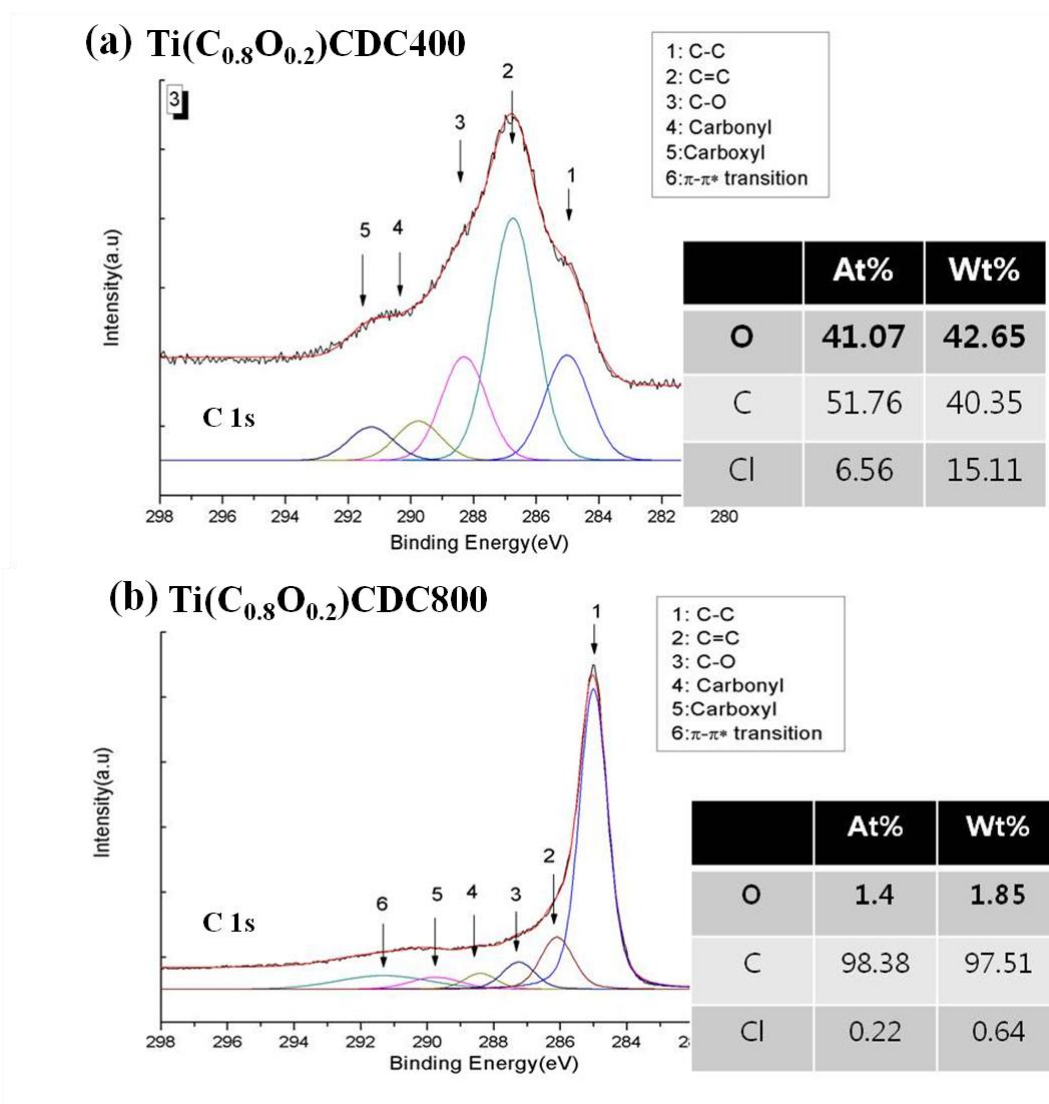


**Figure 30.** XPS results of  $\text{Ti}(\text{C}_{0.8}\text{O}_{0.2})\text{-CDC}$  at (a)400°C, (b)800 °C

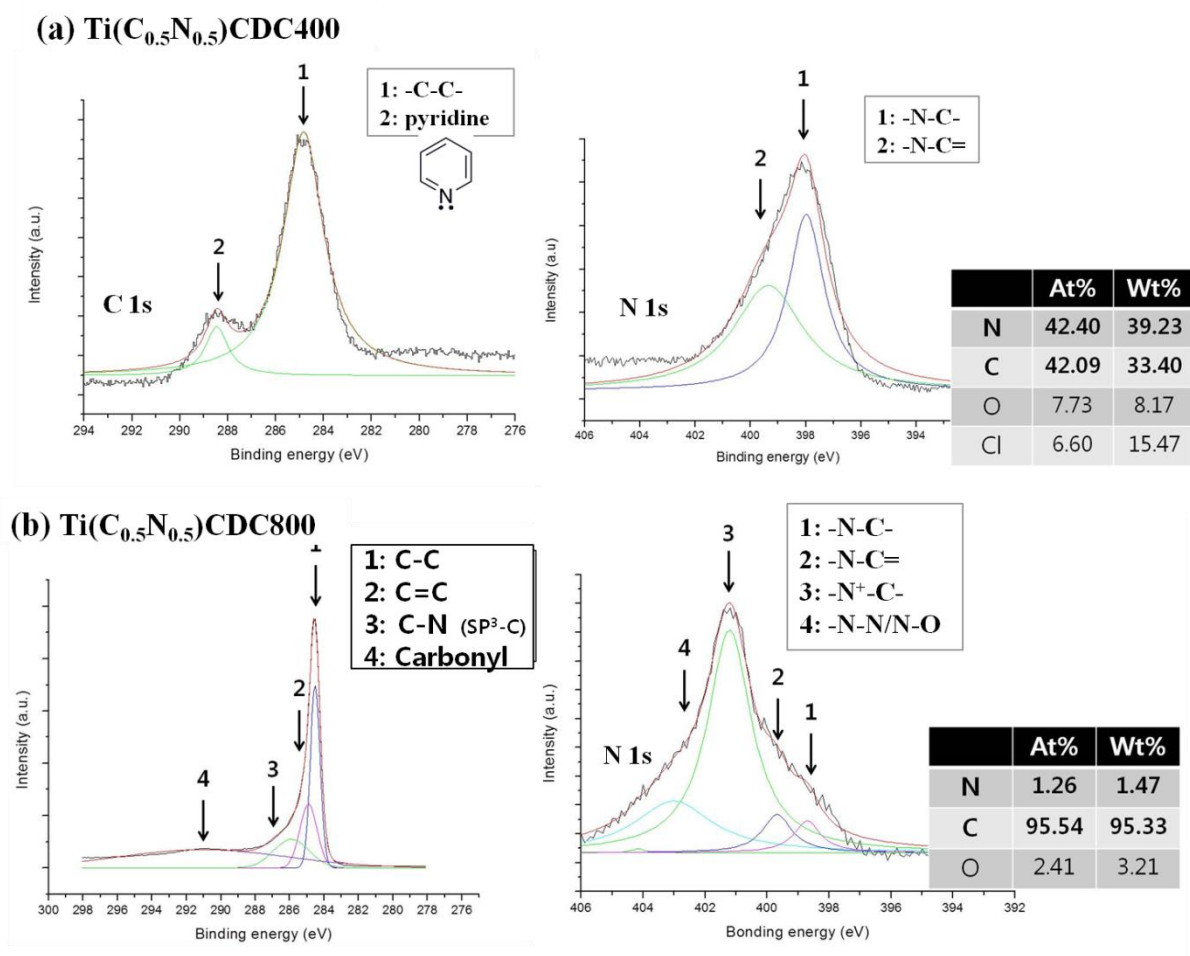


**Figure 31. XPS results of  $\text{Ti}(\text{C}_{0.5}\text{N}_{0.5})\text{-CDC}$  at (a)  $400^\circ\text{C}$ , (b)  $800^\circ\text{C}$**

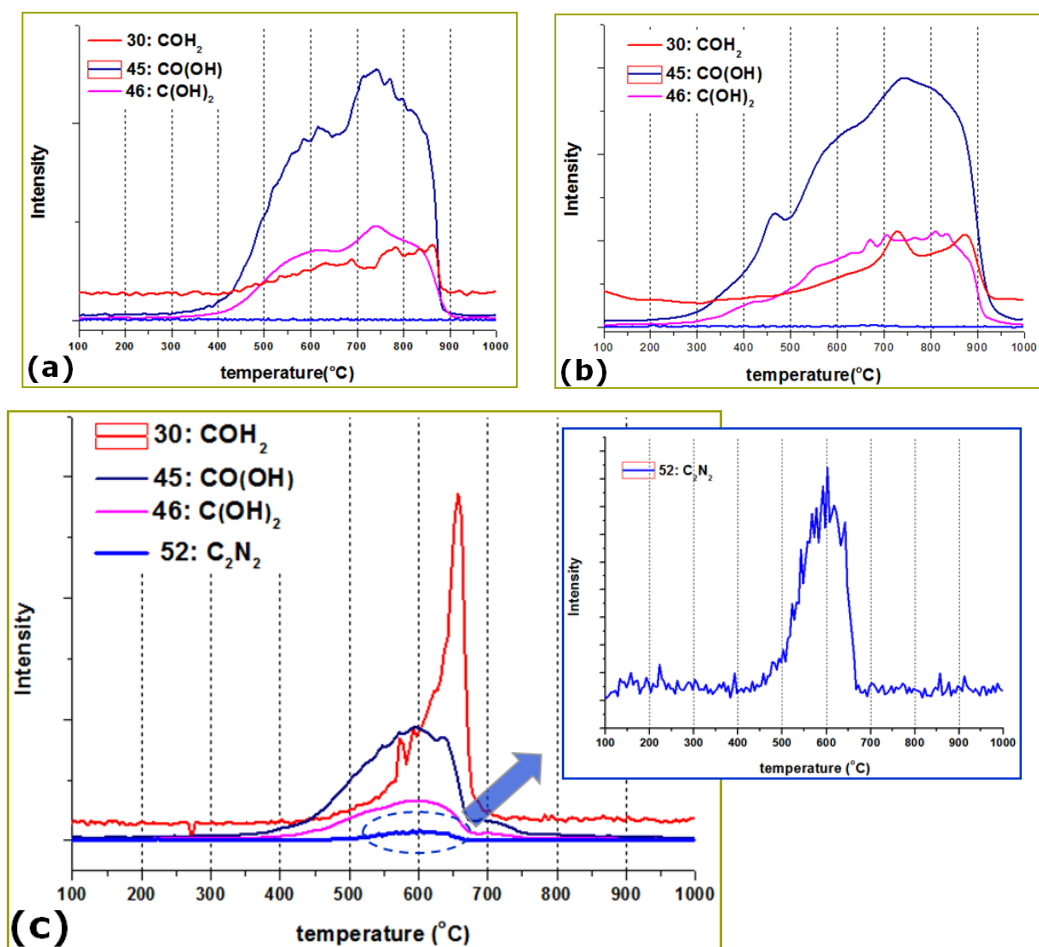


Figure 32. Mass spectroscopy of (a)TiC-CDC chlorinated 800°C (b) $\text{Ti(C}_{0.5}\text{N}_{0.5}\text{)}$ -CDC chlorinated 800°C (c) $\text{Ti(C}_{0.5}\text{N}_{0.5}\text{)}$ -CDC which is chlorinated at 400 °C

### 4.3. Empirical calculation method

#### 4.3.1. Introduction

The reactive empirical bond order potential (REBO) for variety carbon structures developed by Brenner and co-workers and based on potentials first introduced by Abell[93] and Tersoff.[94-96] has been used extensively to study numerous studies, including structural deformation of hydrocarbon[97, 98], carbon nanotube, diamond[99], and amorphous structural carbon[100]. Both Tersoff and Brenner are convenient, short-range, bond-order, empirical potentials which are often used in Molecular Dynamics (MD) simulations and other calculations to model of various carbon-based materials.[101, 102] The convenience of these potentials comes from their rather simple, analytical forms of atomic interactions. The Brenner potential is based directly on the Tersoff potential but has additional terms and parameters which allow it to better describe various chemical reactions in oxygen bonding with carbon, hydrocarbons and include nonlocal effects. Originally, Tersoff potential parameters were independently determined for elements C, Si and Ge. [94-96] Parameters for nitrogen have also recently been developed.[103, 104] And Brenner potential parameters were determined for C, H and Si [98, 105] and oxygen[97] have been developed. Therefore Brenner used to calculate the potential between carbon and oxygen in  $Ti(C_{1-x}O_x)$  and Tersoff potential is for potential between carbon and nitrogen in  $Ti(C_{1-x}N_x)$ . There are tremendous practical advantages to these potentials, where the energy is modeled empirically derived by fitting to data sets from experiments and *ab initio* calculations. Therefore when the results of the REBO potential have been compared to more accurate *ab initio* or tight-binding methods, it has been shown to always be qualitatively accurate and sometimes quantitatively accurate.[97] It means that huge unitcell which contains thousands of atoms is possible to calculate in shorter time than *ab-initio* or other calculation method. In CDC materials, final structure will depends on the rearrangement of potentials with distance between carbon atoms and chlorination temperature. Thus, these Brenner and Tersoff potential which are based on

the bond ordered mechanism are proper to calculate the potential between carbon atoms after extraction titanium during chlorination. It means good expression of real amorphous CDC structure.

#### 4.3.2. Assumption

To determine the structure of solid solution CDC, it needs 3 kinds of assumption as Figure 33.

- No volume change during chlorination.[4, 19, 81]
- $\text{MeCl}_4$  formation effect to pore structure is ignored. (from 3.3.1)
- CDC structure only depends on chlorination temperature and initial carbon distribution.

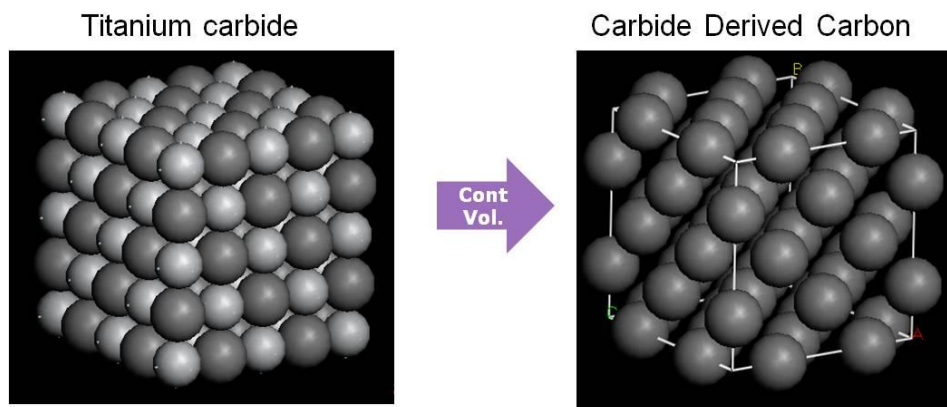


**Figure 33. Dependence of CDC structure from initial carbon distribution.**



#### 4.3.3. Calculation

To calculate TiC-CDC,  $\text{Ti}(\text{C}_{1-x}\text{O}_x)\text{-CDC}$ ,  $\text{Ti}(\text{C}_{1-x}\text{N}_x)\text{-CDC}$ , we build 65,536 atoms include both titanium and carbon, nitrogen, oxygen which generates a simulation cell of size  $69.2\text{\AA} \times 69.2\text{\AA} \times 138.5\text{\AA}$  to simulate a realistic CDC. The amorphous carbon structure is then generated by eliminating all titanium atoms using MD simulations in an (NVT) ensemble at 1073K for 600ps. Then, the material is equilibrated at 200ps as shown in Figure 34. The time step for the MD simulations is 1fs, and periodic conditions are employed in all the three directions. In this way, a nanopore space with a solid amorphous carbon matrix is generated. After elimination of all titanium from its unitcell, we obtained total 32,768 atoms including carbon, oxygen and nitrogen. Then, they were submitted to MD simulations using Brenner or Tersoff potential to minimize non-physical features such as distorted angles and distances of bonding with rearrangement. Due to the high computational cost required to perform a full MD, only the equilibrium phase was performed. Afterward, each structure was confirmed the convergence at 200ps. All relaxations of MD simulation were performed using GULP tool in Materials Studio.[106] We have used Tersoff and Brenner empirical interatomic potentials.

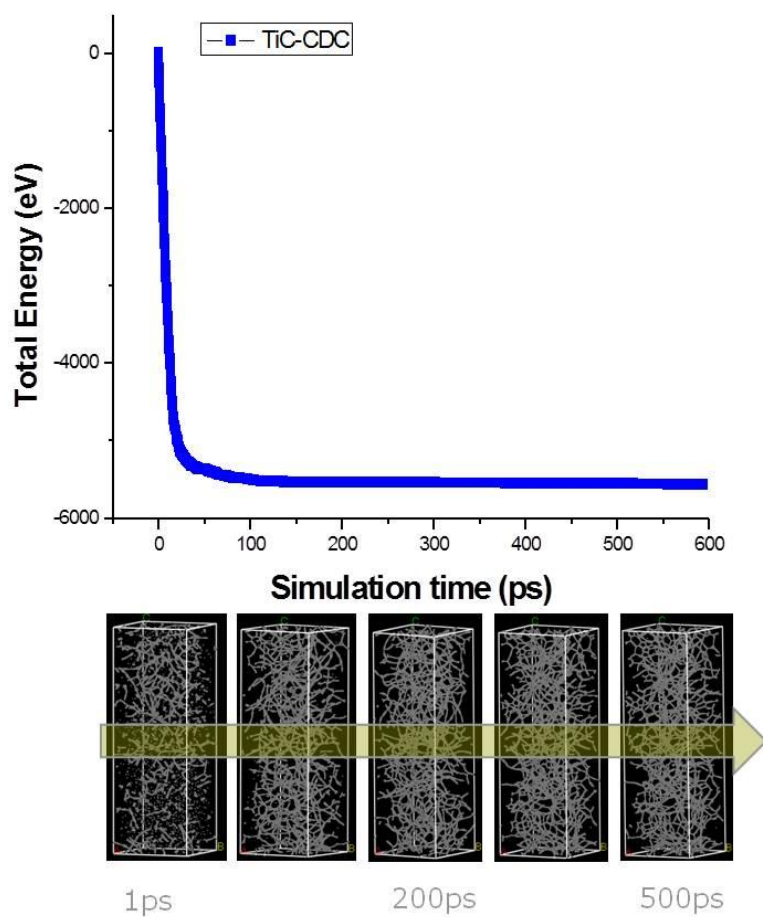


**Figure 34. Convergence of total energy and difference of CDC structure with simulation time.**

#### 4.3.4. Structure of simulated results

To ensure this calculation strategy, we compared two approaches of MD using SiC instead of TiC due to the lack of titanium potential in both Tersoff and Brenner. Although SiC has different lattice structure with TiC, it is worth to see the difference with comparing these two approaches; The first model is calculated by eliminating silicon atoms in one by one layer from the surface of SiC unitcell. And the second method is eliminating all silicon atoms at once in SiC unitcell before generating MD. With comparing pore properties which are calculated by the Connolly surface within Materials Studio, after convergence of total energy, we can ensure that it shows almost same SSA and total pore volume ( $^{total}V_p$ ) as shown in Table 6. SSA and  $^{total}V_p$  increased with elimination Si atoms from the surface of SiC lattice. The definition of this Connolly surface will be treated below in 4.2.5 part. Although the first approach can be more close to the real structure because the driving force of chlorination is the diffusion of  $Cl_2$ , above assumption can be proper to determine CDC pore structures with the similar result between (g) and (h) in Figure 35 and Table 6.

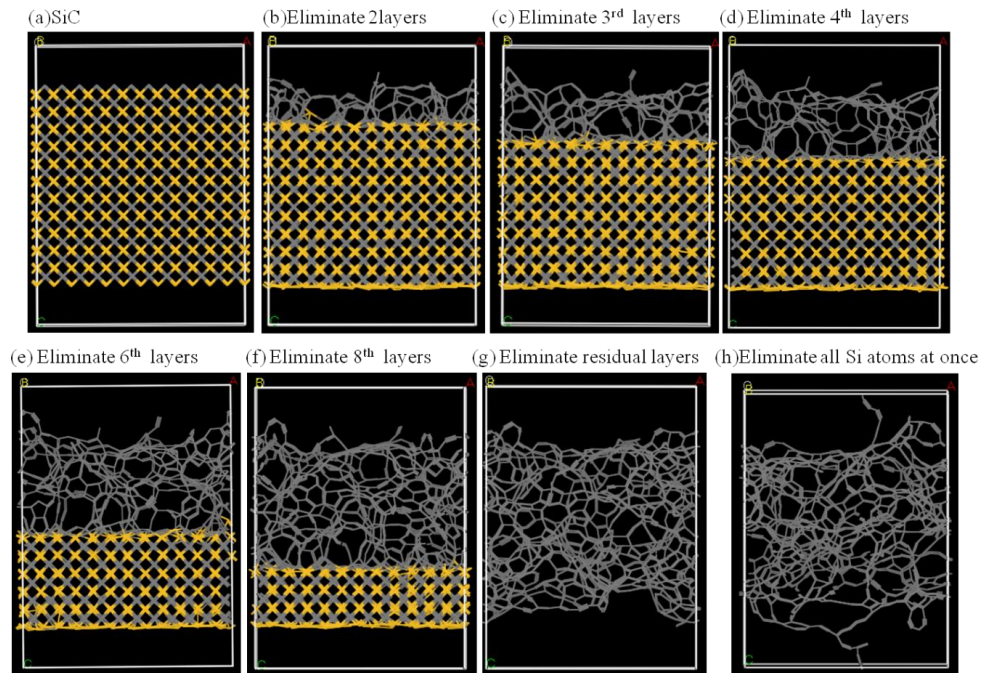


**Figure 35.** Calculated structure of SiC from the surface layer with eliminating by (a) 0 layer (b) 2<sup>nd</sup> layers (c) 3<sup>rd</sup> layer (d) 4<sup>th</sup> layer (e) 6<sup>th</sup> layer (f) 8<sup>th</sup> layer (g) residual layers (h) all layer at once from initial SiC

SiC-CDC	Exp. result [23]	(a) 0 layer	(b) 2 <sup>nd</sup> layer	(c) 3 <sup>rd</sup> layer	(d) 4 <sup>th</sup> layer	(e) 6 <sup>th</sup> layer	(f) 8 <sup>th</sup> layer	(g) residual layers	(h) all layer at once
SSA (m <sup>2</sup> /g)	1500	0	258.4	466.1	592.0	482.464	642.7	1580.4	1712.5
V <sub>total</sub> (cm <sup>3</sup> /g)	0.62	0	0.088	0.156	0.189	0.125	0.169	0.50	0.455

**Table 6.** Specific surface area and total pore volume calculated by Connolly surface which is from the surface layer with eliminating Si atoms in (a) 0 layer (b) 2<sup>nd</sup> layers (c) 3<sup>rd</sup> layer (d) 4<sup>th</sup> layer (e) 6<sup>th</sup> layer (f) 8<sup>th</sup> layer (g) residual layers (h) all layer at once from initial SiC

The significant difference can be seen between  $\text{Ti}(\text{C}_{0.7}\text{O}_{0.3})\text{-CDC}$  and  $\text{Ti}(\text{C}_{0.7}\text{N}_{0.3})\text{-CDC}$  after convergence as shown in Figure 36. As our expectation,  $\text{Ti}(\text{C}_{0.7}\text{O}_{0.3})\text{-CDC}$  shows CO and  $\text{CO}_2$  gas formation and amorphous carbon structure. In contrast,  $\text{Ti}(\text{C}_{0.7}\text{N}_{0.3})\text{-CDC}$  shows that carbon atoms aggregate near around nitrogen and no  $\text{N}_2$  gas formation. It can be thought due to the possibility of new phase formation such as  $\text{C}_x\text{N}_y$ . It will be good agreement with the increase of C-N, C=N bonding after chlorination at  $800^\circ\text{C}$  in Figure 31(b). And Figure 37 shows the comparison of simulated  $\text{TiC-CDC}$ ,  $\text{Ti}(\text{C}_{0.7}\text{O}_{0.3})\text{-CDC}$ ,  $\text{Ti}(\text{C}_{0.7}\text{N}_{0.3})\text{-CDC}$  structures which is on convergence state again after eliminating all oxygen and nitrogen.  $\text{Ti}(\text{C}_{0.7}\text{O}_{0.3})\text{-CDC}$  is observed additional empty space with the formation of carbon monoxide compared to  $\text{TiC-CDC}$ . Single graphite layers were folded specially in  $\text{Ti}(\text{C}_{0.7}\text{N}_{0.3})\text{-CDC}$  and also it is observed bigger empty space which can be suggested bigger pores than  $\text{TiC-CDC}$  and  $\text{Ti}(\text{C}_{0.7}\text{O}_{0.3})\text{-CDC}$  due to the elimination of nitrogen and bonded carbon. This behavior can be significantly seen in next part with Connolly surface. One should note, however, that Tersoff and Brenner's potential does not includes van der Waals forces, which should be quite important in determining the geometries properties of carbon structures. It is the reason that many folded graphene layers can be observed in calculated structure. By contrast, in real CDC structure (002) plane layers of graphite could be confirmed with TEM.

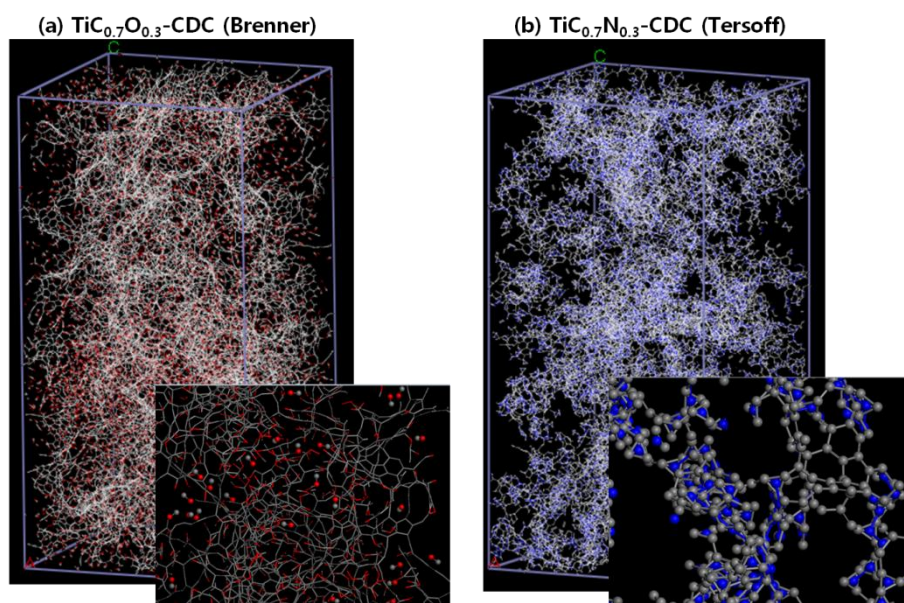


**Figure 36.** CDC structures of (a) $\text{Ti}(\text{C}_{0.7}\text{O}_{0.3})$ -CDC and (b) $\text{Ti}(\text{C}_{0.7}\text{N}_{0.3})$ -CDC after convergence (white grey : carbon, red : oxygen, blue :nitrogen)

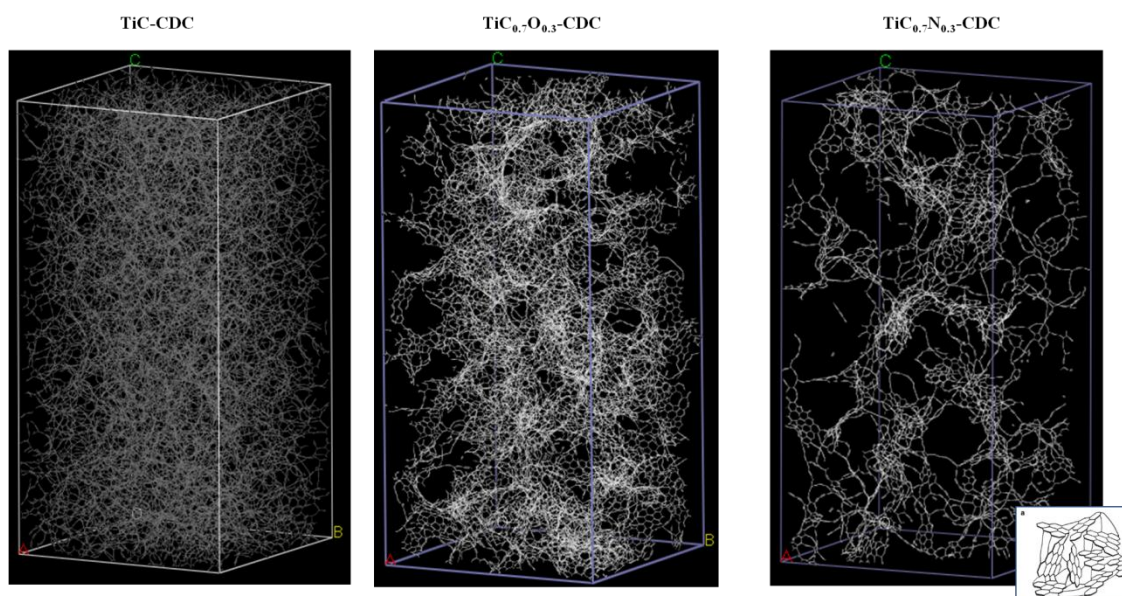


**Figure 37.** CDC structures of (a) $\text{TiC}$ -CDC (b)  $\text{Ti}(\text{C}_{0.7}\text{O}_{0.3})$ -CDC and (c)  $\text{Ti}(\text{C}_{0.7}\text{N}_{0.3})$ -CDC after elimination of oxygen or nitrogen

#### 4.3.5. Connolly surface area

A Connolly surface[107, 108] was created for the model using the Atom, Volumes and Surface module in Materials Studio as a condition of coarse grid resolution and a Connolly radius set to 1.82 Å (the kinetic radius of N<sub>2</sub>). It is calculated from the bottom of a probe molecule (N<sub>2</sub>) rolling across the surface as illustrated in Figure 38. It shows the Connolly surface area presents a quick and easy way to judge specific surface area and pore volume. By comparing simulated the Connolly surface area to the BET surface areas from the experimental values, this approach can be judged. In Figure 39, it is observed slit shaped pore structure of TiC-CDC. The size of all pores seems less than 1nm size which is good agreement with above experimental results. Also Ti(C<sub>0.7</sub>O<sub>0.3</sub>)-CDC shows wider size of slit pores which means CO/CO<sub>2</sub> reaction during chlorination can enhance micropore volume. And mesopore formation which means bigger than 2nm can be confirmed in Ti(C<sub>0.7</sub>N<sub>0.3</sub>)-CDC as can be seen in Figure 39(c). Meanwhile, simulated TiC-CDC, Ti(C<sub>0.7</sub>O<sub>0.3</sub>)-CDC show almost same SSA (1577, 3433m<sup>2</sup>/g) with experiment (1512, 3113m<sup>2</sup>/g) in Table 7. But the reason of the little different SSA of Ti(C<sub>1-x</sub>N<sub>x</sub>)CDC is from the inaccurate elimination of C<sub>x</sub>N<sub>y</sub> in its unitcell. Also pore volume in Table 7 shows same behavior with experiment even with little deviation from real values. It can be seen this approach is good to expect and determined the structure of solid solution CDC.

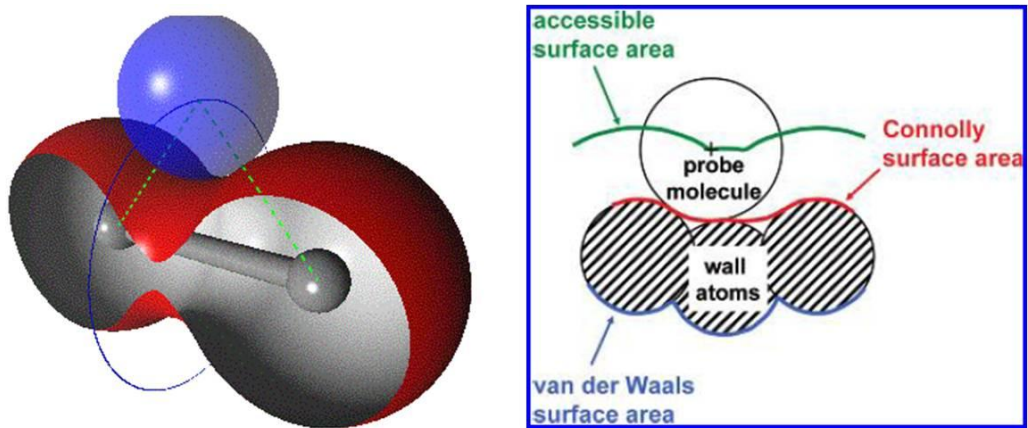


**Figure 38.** Schematic diagram for understand the definition of connolly surface area (red line), probe molecule (N<sub>2</sub>) [109]



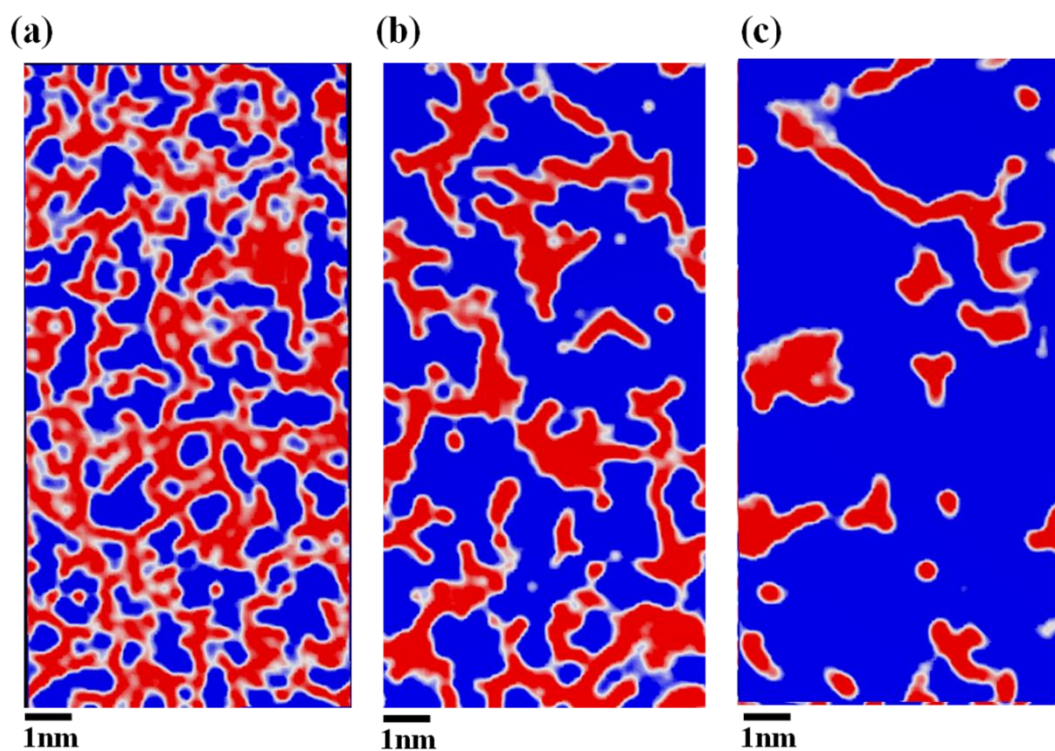


Figure 39. Slice planes of calculated (a)TiC-CDC, (b)Ti(C<sub>0.7</sub>O<sub>0.3</sub>)-CDC, (c)Ti(C<sub>0.7</sub>N<sub>0.3</sub>)-CDC (red: carbon occupied layers, blue: empty space)

	TiC CDC	Ti(C <sub>0.7</sub> O <sub>0.3</sub> ) CDC	Ti(C <sub>0.7</sub> N <sub>0.3</sub> ) CDC
<b>SSA</b> (m <sup>2</sup> /g)	<b>1545.8</b>	<b>3432.5</b>	<b>1488.7</b>
<b>V<sub>total</sub></b> (cm <sup>3</sup> /g)	<b>0.434</b>	<b>1.278</b>	<b>3.924</b>

Table 7. Specific surface area and pore volume calculated by Connolly surface of CDCs.

#### 4.4. Summary

Mechanism of pore formation of  $\text{Ti}(\text{C}_{1-x}\text{A}_x)$  ( $\text{A} = \text{O}$  or  $\text{N}$ ) is suggested and supporting experimental results observed. To understand the mechanism of pore formation, composition of  $\text{Ti}(\text{C}_{0.7}\text{O}_{0.3})\text{-CDC}$ ,  $\text{Ti}(\text{C}_{0.7}\text{N}_{0.3})\text{-CDC}$  is fixed and compared with chlorination temperature. During the chlorination,  $\text{CO}$  and  $\text{CO}_2$  formation reaction can be proceeded and enhanced micropores after extraction of titanium due to the oxygen source in  $\text{Ti}(\text{C}_{0.7}\text{O}_{0.3})$ . Meanwhile, during chlorination of  $\text{Ti}(\text{C}_{0.7}\text{N}_{0.3})$ , synthesized carbon nitride during chlorination is reported to even partially decompose above  $650^\circ\text{C}$  due to its low stability. It is expected that huge mesopore formation derived by partial decomposition of  $\text{C}_x\text{N}_y$  solid phase. Also Molecular dynamics simulation is generated to understand the amorphous CDC structure. It shows some agreement with the experimental results even if more or less deviation can be observed.

## **V. APPLICATIONS OF MICRO/MESO POROUS CARBIDE DERIVED CARBON**

### **5.1. Micropore of $\text{Ti}(\text{C}_{1-x}\text{O}_x)$ -CDC for hydrogen storage**

#### **5.1.1. Introduction**

The criteria for an onboard hydrogen storage system have been defined by the US Department of Energy (DOE), in close collaboration with the automotive industry. The most frequently quoted target is a gravimetric system storage capacity exceeding 6wt% (2.0kWh/kg). This was the 2010 target [110] until recently but has since been reduced to 4.5wt% (1.5kWh/kg). At the time of writing, the 2015 target is 5.5wt% (1.8kWh/kg), a refueling time of less than 3min (1.5kg/min), a minimum lifetime of 1500 hydrogenation/dehydrogenation cycles, an operating pressure in the range of 3-100atm (0.3-10.1MPa). These figures are not currently satisfied by any known storage system. To satisfy these needs, the promising chance of a solution to this problem is thought to be through the use of solid state storage and, as a result, the search for suitable candidate materials has intensified. [111]

There are presently three basic routes known for the storage of hydrogen in materials; i) physisorption, ii) chemisorptions, and/or (iii) chemical reaction. One of these methods, the advantages of physisorption for hydrogen storage include the high reversibility between adsorption and desorption, fast adsorption/desorption kinetics and low temperature and low or moderate pressure involved.[76] Physical adsorption in solid depends on weak van-der Waals bonding, and as the minimum potential energy between the surface of the storage material and hydrogen is at a distance of approximately one molecular size of hydrogen, it means extremely small micropores are necessary for maximizing physisorption of molecular hydrogen.[76, 112, 113] Microporous materials tend to have high storage capacities at low temperatures and they contain pore dimensions of less than 2nm and extraordinarily large internal

surface areas, high micropore volume values. One of many candidates, carbons are interested as attractive adsorbents because of their low molar mass, high specific surface area and good thermal, chemical stability.[114] Many types of microporous carbons have been investigated including activated carbon, carbon nanotubes and nanofibers and, more recently, carbide derived carbons(CDC). CDC is the one of good candidate for hydrogen storage material due to its narrow pore size distribution, high surface area.[115] Thus, we suggest definitely clear results of noble  $\text{Ti}(\text{C}_{1-x}\text{O}_x)\text{CDC}$  which contained the high micropore dimension with the substitution of oxygen in lattice structure of TiC as a raw material.

### 5.1.2. Experiment

Volumetric hydrogen adsorption analysis is used by hydrogen adsorption isotherms at low pressures ( $<1\text{atm}$ ) and 77K temperature with BELSORP-mini(Japan). Gravimetric  $\text{H}_2$  adsorption capacities were measured under high-pressure conditions (up to 80bar) at 77 K, 87K using a PCT Pro 2000 (Hy-Energy LLC, America)

### 5.1.3. Results and discussion

$\text{Ti}(\text{C}_{0.7}\text{O}_{0.3})\text{-CDC}$  which contains optimized SSA and micropore volume shows significantly high  $\text{H}_2$  uptake with value up to 3.0wt% as shown Figure 40. They also outperform the benchmark TiC-CDC chlorinated at 800 °C. In the low pressure range of  $P/P^0$  ( $<0.25$ ), it shows not much different hydrogen adsorption volume due to the same micropore size ( $<1\text{nm}$ ) derived by extraction of titanium. However, it increased dramatically from 0.5 to 1atm due to the wider micropore formation( $<2\text{nm}$ ) from CO/ $\text{CO}_2$  reaction. Also the results of high-pressure hydrogen sorption measurements preformed at 77K and 87K, respectively, are given in Figure 41.  $\text{Ti}(\text{C}_{0.7}\text{O}_{0.3})\text{-CDC}$  shows rapid convergence at 4.51wt% at 77k, 20bar compared to 3.42wt% of TiC-CDC. That is, high  $\text{H}_2$  uptake was attributed to the new adsorption sites formed by oxygen resulting to high SSA and micropore volume.

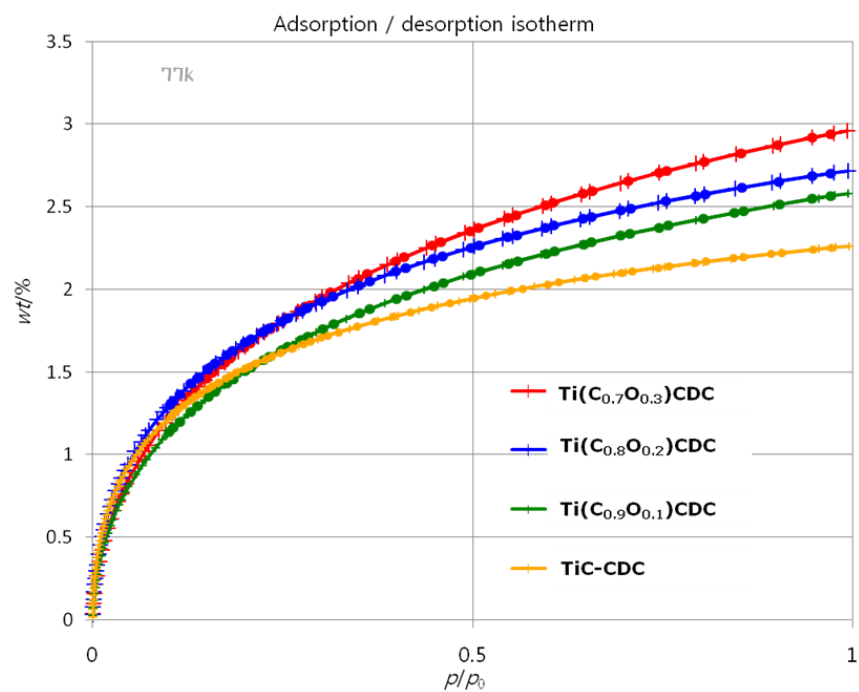


**Figure 40.** Low pressure ( $\sim 1\text{atm}$ )  $\text{H}_2$  sorption isotherms at 77K with oxygen content of  $\text{Ti}(\text{C}_{1-x}\text{O}_x)\text{-CDC}$

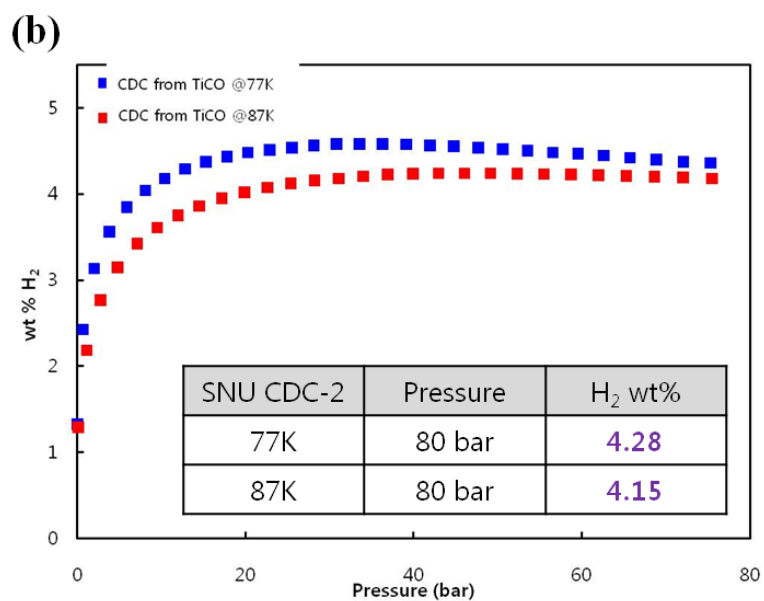
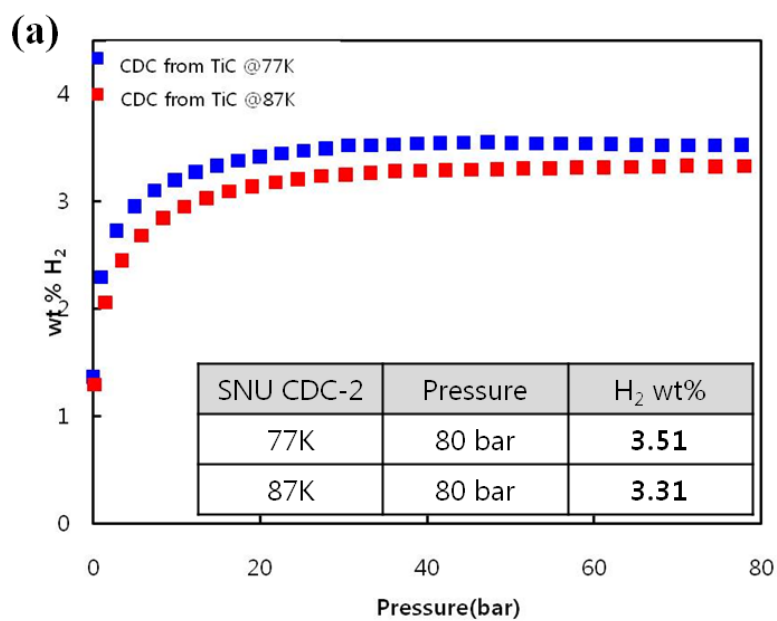


**Figure 41. High pressure (80atm) H<sub>2</sub> sorption isotherms at 77K with oxygen content of (a) TiC-CDC and (b)Ti(C<sub>0.7</sub>O<sub>0.3</sub>)-CDC**

## **5.2. Mesopore of $\text{Ti}(\text{C}_{1-x}\text{N}_x)$ -CDC for supercapacitor candidate**

### **5.2.1. Introduction**

Recently [116], more important applications proposed for CDC are fuel cells [117], different selective adsorption processes such as extraction/purification of noble gases [118] compared to hydrogen storage materials. However, one of the most challenging applications is the rapidly developing field of the electrochemical energy storing devices among them super- or ultracapacitors. [119, 120] Supercapacitors, which are also called ultracapacitors or electrical double-layer capacitors, are rechargeable devices for electrical energy storage. They are poised to begin displacing batteries in applications where high power and low weight are essential. As batteries rely on slow rate-determining chemical reactions, they lack the ability to supply quick power bursts. In addition, chemical reactions in batteries contribute to 20 to 25% of the charging energy being lost. Most high-power batteries offer limited lifetime, require narrow temperature window for efficient operation, and are not environmentally friendly. Supercapacitors offering long-cycle life ( $>100,000$  cycles), high efficiency ( $>90\%$ ), and fast charging/discharging are competitive alternatives to batteries for such applications as personal electronic devices, mobile telecommunications, back-up power storage, peak power sources for hybrid electric, electric and traditional vehicles, among others [4]. A supercapacitor consists of two porous electrodes with high surface area separated by an ionconducting membrane. Energy is stored as a charge separation in a thin double layer at the interface between the electrode and the electrolyte. To increase energy storage, the electrodes in a supercapacitor should have as high a surface area accessible to the electrolyte as possible. Till date, various carbon materials have been used as electrodes in double-layer capacitors, including activated carbons, carbon fiber composites, and CNT. The main disadvantage of high surface area activated carbons used in supercapacitors is their wide pore-size distribution. A large fraction of the pores is too small to permit the electrolyte ions to freely diffuse in and out of pores, so that only a fraction of the total surface area is utilized to form a double layer (Figure 42).

The presence of very small pores also increases the electrode resistance.[4] Very large pores that are present in activated carbons are not so efficient for energy storage. Electrodes made from carbon fibers and CNT also suffer from a wide pore-size distribution. In the ideal case, the electrode material should have a narrow pore-size distribution with an average pore size tailored to suit the electrolyte used. So far, the best CDC materials for supercapacitors have been made from titanium carbide.[121] This CDC contains a large quantity of very small nanopores with pore size below 6–7 Å°, which are inaccessible to the solvated electrolyte ions [121, 122]. Recently a new method was developed, which enables to improve the pore size distribution in the carbide-derived carbon particles [123]. Using the chlorination of the carbide/oxide mixture, due to which the carbothermal reduction of TiO<sub>2</sub> in chlorine atmosphere gives the possibility to oxidise in situ the desired part of carbon during its formation from the carbide. However, it shows limited application due to the inhomogeneous distribution of TiO<sub>2</sub> dispersion.[116] Thus, using mesoporous Ti(C<sub>1-x</sub>N<sub>x</sub>)-CDC, we can show possibility to fine-tune the pore size which is forced the development of applications requiring the porous material for supercapacitor.

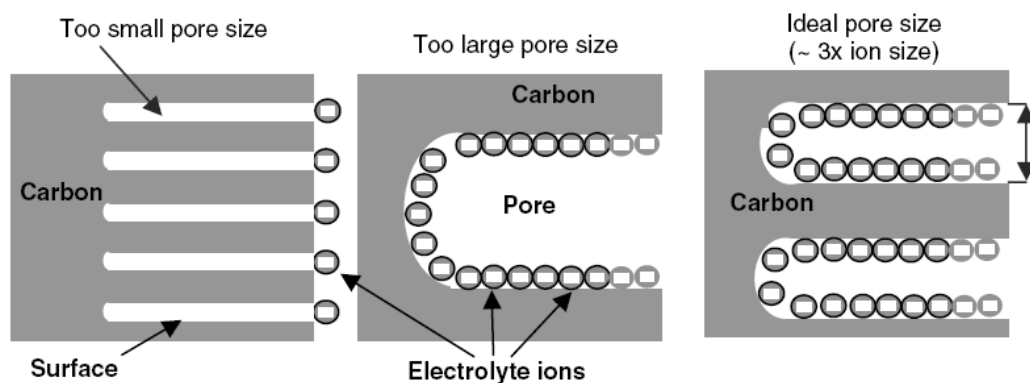


**Figure 42. Schematic explanation of the optimum pore size for the highest surface area accessible by the electrolyte ions.**



### 5.2.2. Experiment

Cyclic voltammetry and galvanostatic charge-discharge were performed on electrodes produced from  $\text{Ti}(\text{C}_{0.5}\text{N}_{0.5})$ -CDC chlorinated at  $800^{\circ}\text{C}$  in NMP(N-methyl 2-pyrrolydone). Electrodes were produced by combining 95% CDC and 5% PVDF (polyvinylidene fluoride) to form a film which was then made into a thick foil using a doctor blade. For the comparison, CNT used as commercial multiwall CNT (CM250, diameter: 15nm, Hanwha Nanotec.) and activated carbon which has SSA of  $2450\text{m}^2/\text{g}$  (Sam Cheon-ri) performed under same experimental conditions. Electrodes were dried overnight in vacuum at  $120^{\circ}\text{C}$ . From this film,  $1\text{cm}^2$  circular electrodes were punched out and inserted into a two electrode cell with a cellulose fibre filter paper and 1M  $\text{LiPF}_6$  aqueous electrolyte. Two-electrode cells were assembled in an airtight glove box with two  $\text{Ti}(\text{C}_{0.5}\text{N}_{0.5})$ -CDC electrodes sandwiching a cellulose separator. For electrochemical measurement a test cell of a capacitor (working potential: 1.5~3.5V) was fabricated with Ethylen Carbonate(EC) : DiEC =1:1. Specific capacitance was calculated from the discharge curves at 0~2 mA using the equation:  $C = -2i / (m dV/dt)$ , where m is the mass of a single electrode, i is the discharge current and  $dV/dt$  is the slope of the discharge curve ( $50\text{mV/s}$ ). All voltages were referenced to the open cell voltage of the fully discharged cell.

### 5.2.3. Results and discussion

The electrochemical behavior of the supercapacitor was analyzed in a two-electrode system using cyclic voltammetry (CV). Although the current response profile of the CV curve at a scan rate of  $50\text{mV/s}$  is not rectangular along the time-potential axis, it can show the possibility of solid solution CDC for supercapacitor. Because  $\text{Ti}(\text{C}_{0.5}\text{N}_{0.5})$ CDC has better capacitance behavior than activated carbon and similar with CNT. All values in Figure 43 can't compare with other published data however it can be only seen relatively.

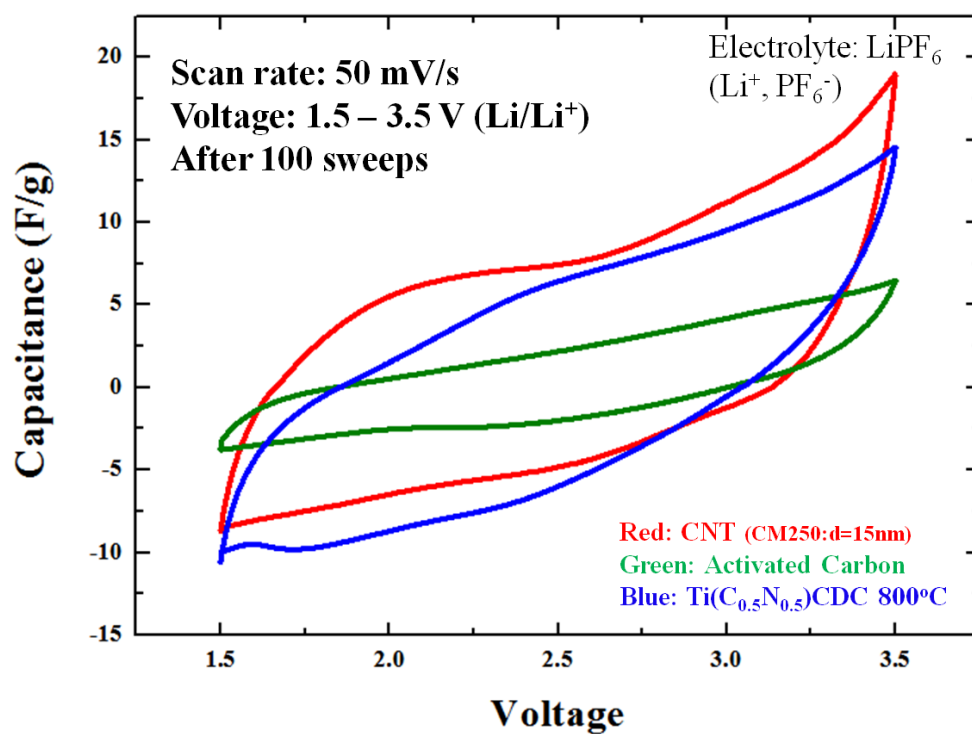


Figure 43. CV taken at scan rates of 50mV/s for  $\text{Ti}(\text{C}_{0.5}\text{N}_{0.5})\text{CDC}$  chlorinated at 800°C

### 5.3. Summary

Porous CDC electrode which is synthesized from  $\text{Ti}(\text{C}_{0.5}\text{N}_{0.5})$  shows higher capacitance than commercial activated carbon and similar with CNT-electrode. Although this CV data couldn't compare previously published data due to their too low values, but it is meaningful to see the relative each behavior. Microporous activated carbon contained too narrow sized pore, it leads to low capacitance. However,  $\text{Ti}(\text{C}_{0.5}\text{N}_{0.5})\text{CDC}$  which contains mesopore as mentioned above chapters.

## VI. Overall conclusion

Mechanical alloying (MA) method is adapted for the synthesis of  $(\text{Ti}_{1-x}\text{Me}_x)\text{C}$  and  $\text{Ti}(\text{C}_{1-x}\text{A}_x)$  solid solution phase. Specially, pore structure of carbide derived carbon was successfully designed by chlorination of  $\text{Ti}(\text{C}_{1-x}\text{A}_x)$  (A= Oxygen or Nitrogen) solid solution phase. First, we can successfully synthesize and control accurate composition of solid solution precursor by high energy ball milling. Second, with selection of the substitutional atom (A), it could be possible to change specific dimension of pore volumes which can be covered in the range of micropore ( $<2\text{nm}$ ) or mesopore size ( $2\text{nm}-50\text{nm}$ ). Finally,  $\text{Ti}(\text{C}_{1-x}\text{A}_x)\text{-CDC}$  has significantly better values of SSA and pore volumes than reported before.  $\text{Ti}(\text{C}_{1-x}\text{O}_x)\text{-CDC}$  contains narrow micropore size, in contrast,  $\text{Ti}(\text{C}_{1-x}\text{N}_x)\text{-CDC}$  is dominantly shows formation of mesopore. Thus, characteristic dimensions of mesopore or micropore can be controlled by kind of substitutional atom(A) instead of carbon in solid solution. One of CDCs have noticeably shows not only 73% ( $V_{\text{micro}}/V_{\text{total}}$ ) micropore volume fraction up to  $\text{Ti}(\text{C}_{0.7}\text{O}_{0.3})\text{CDC}$ :  $1.55\text{cm}^3/\text{g}$  ( $V_{\text{micro}}$ ) per  $1.72\text{cm}^3/\text{g}$  ( $V_{\text{total}}$ ),  $3200\text{cm}^2/\text{g}$  (SSA) but also mesopore volume up to  $\text{Ti}(\text{C}_{0.5}\text{N}_{0.5})$ :  $3.34\text{cm}^3/\text{g}$  ( $V_{\text{meso}}$ ) per  $3.45\text{cm}^3/\text{g}$  ( $V_{\text{total}}$ ),  $522.1\text{cm}^2/\text{g}$  (SSA) by selective extraction of titanium. Each high pore properties derived high properties in the field of hydrogen storage material (micropore) and supercapacitor (mesopore). Although  $(\text{Ti}_{1-x}\text{Me}_x)\text{C-CDC}$  didn't show significant difference, its result was meaningful to use the analysis of CDC pore structure due to the determination of only metal effect during chlorination. Also molecular dynamic simulation was performed with few assumptions, it shows real pore structure and slit sized pores of CDCS. We can calculate pore volume and specific surface area with own molecular dynamics simulation too. Specially, simulation results supported significant difference between  $\text{Ti}(\text{C}_{1-x}\text{O}_x)\text{CDC}$  and  $\text{Ti}(\text{C}_{1-x}\text{N}_x)\text{CDC}$ .

## VII. Reference.

- [1] Urbonaite S, Juárez-Galán JM, Leis J, Rodríguez-Reinoso F, Svensson G. Porosity development along the synthesis of carbons from metal carbides. *Microporous and Mesoporous Materials*. 2008;113(1–3):14-21.
- [2] Miloslav Nic JJ, Bedrich Kosata,. IUPAC Compendium of Chemical Terminology (IUPAC). Laboratory of Informatics and Chemistry of the Institute of Chemical Technology, Prague. 2012.
- [3] Harry Marsh FR-R. Activated Carbon. Oxford,; Elsevier; 2006.
- [4] Y. Gogotsi (Ed.). *Nanomaterials Handbook*. 2006; 2006.
- [5] Jagiello J, Thommes M. Comparison of DFT characterization methods based on N<sub>2</sub>, Ar, CO<sub>2</sub>, and H<sub>2</sub> adsorption applied to carbons with various pore size distributions. *Carbon*. 2004;42(7):1227-32.
- [6] Ocelli ML, Olivier JP, Perdigon-Melon JA, Auroux A. Surface Area, Pore Volume Distribution, and Acidity in Mesoporous Expanded Clay Catalysts from Hybrid Density Functional Theory (DFT) and Adsorption Microcalorimetry Methods. *Langmuir*. 2002;18(25):9816-23.
- [7] Presser V, McDonough J, Yeon S-H, Gogotsi Y. Effect of pore size on carbon dioxide sorption by carbide derived carbon. *Energy & Environmental Science*. 2011;4(8):3059-66.
- [8] Vinu A, Ariga K, Mori T, Nakanishi T, Hishita S, Golberg D, et al. Preparation and Characterization of Well-Ordered Hexagonal Mesoporous Carbon Nitride. *Advanced Materials*. 2005;17(13):1648-52.
- [9] Gao Y, Presser V, Zhang L, Niu JJ, McDonough JK, Pérez CR, et al. High power supercapacitor electrodes based on flexible TiC-CDC nano-felts. *Journal of Power Sources*. 2012;201(0):368-75.
- [10] Gogotsi Y, Nikitin A, Ye H, Zhou W, Fischer JE, Yi B, et al. Nanoporous carbide-derived carbon with tunable pore size. *Nat Mater*. 2003;2(9):591-4.
- [11] Portet C, Kazachkin D, Osswald S, Gogotsi Y, Borguet E. Impact of synthesis conditions on surface chemistry and structure of carbide-derived carbons. *Thermochimica Acta*. 497(1-2):137-42.

- [12] Popovska N, Kormann M. Processing of porous carbon with tunable pore structure by the carbide-derived carbon method. *JOM Journal of the Minerals, Metals and Materials Society*. 2010;62(6):44-9.
- [13] Gogotsi YG, Jeon I-D, McNallan MJ. Carbon coatings on silicon carbide by reaction with chlorine-containing gases. *Journal of Materials Chemistry*. 1997;7(9):1841-8.
- [14] Dash RK, Nikitin A, Gogotsi Y. Microporous carbon derived from boron carbide. *Microporous and Mesoporous Materials*. 2004;72(1-3):203-8.
- [15] I.M. Kotina. Study of the lithium diffusion in nanoporous carbon materials produced from carbides. *J Non-Cryst Solids*. 2002(299-302):815.
- [16] M. Jacob. Synthesis of structurally controlled nanocarbons- in particular the nanobarrel carbon. *Solid State Sci*. 2003;5:133-7.
- [17] J. Leis AP, M. Arulepp, M. Kaarik, and G. Svensson,. Carbon nanostructures produced by chlorinating aluminium carbide,. *Carbon*. 2001;39:2043-8.
- [18] R.K. Dash GY, and Y. Gogotsi,. Synthesis, structure and porosity analysis of microporous and mesoporous carbon derived from zirconium carbide. *Microporous and Mesoporous Mater*. 2005;86:50-7.
- [19] G. Yushin EH, A. Nikitin, H. Ye, M.W. Barsoum, and Y. Gogotsi,. Synthesis of nanoporous carbide-derived carbon by chlorination of titanium silicon carbide. *Carbon*. 2005;43:2075-82.
- [20] E.N. Hoffman GY, M.W. Barsoum, and Y. Gogotsi,. Synthesis of carbide-derived carbon by chlorination of  $Ti_2AlC$ . *Chem Mater*. 2005;17:2317-22.
- [21] Hoffman EN, Yushin G, El-Raghy T, Gogotsi Y, Barsoum MW. Micro and mesoporosity of carbon derived from ternary and binary metal carbides. *Microporous and Mesoporous Materials*. 2008;112(1-3):526-32.
- [22] Yeon S-H, Reddington P, Gogotsi Y, Fischer JE, Vakifahmetoglu C, Colombo P. Carbide-derived-carbons with hierarchical porosity from a preceramic polymer. *Carbon*. 2010;48(1):201-10.
- [23] Vakifahmetoglu C, Presser V, Yeon S-H, Colombo P, Gogotsi Y. Enhanced hydrogen and methane gas storage of silicon oxycarbide derived carbon.

Microporous and Mesoporous Materials. 2011;144(1-3):105-12.

[24] Zetterström P, Urbonaitė S, Lindberg F, Delaplane RG, Leis J, Svensson G. Reverse Monte Carlo studies of nanoporous carbon from TiC. *Journal of Physics: Condensed Matter*. 2005;17(23):3509.

[25] Thomson KT, Gubbins KE. Modeling Structural Morphology of Microporous Carbons by Reverse Monte Carlo. *Langmuir*. 2000;16(13):5761-73.

[26] Mathioudakis C, Kopidakis G, Kelires PC, Wang CZ, Ho KM. Physical trends in amorphous carbon: A tight-binding molecular-dynamics study. *Physical Review B*. 2004;70(12):125202.

[27] S.Y. Ahn SK. Formation of Core/Rim Structures in Ti(C,N)-WC-Ni Cermets via a Dissolution and Precipitation Process. *Journal of the American Ceramic Society*. 2000;83(6):1489-94.

[28] Jung J, Kang S. Effect of ultra-fine powders on the microstructure of Ti(CN)-xWC-Ni cermets. *Acta Materialia*. 2004;52(6):1379-86.

[29] Wally P, Ettmayer P, Lengauer W. The Ti-Mo-C-N system: Stability of the (Ti, Mo)(C, N)<sub>1-x</sub> phase. *Journal of Alloys and Compounds*. 1995;228(1):96-101.

[30] Jung J, Kang S. Sintered (Ti,W)C carbides. *Scripta Materialia*. 2007;56(7):561-4.

[31] Jinkwan Jung K, S. Sintered (Ti,W)C carbides. *Scripta Materialia*. 2007;56(7):561-4.

[32] Sangho Park SK. Toughened ultra-fine (Ti,W)(C,N)-Ni cermets. *Scripta Materialia*. 2005;52 (2005) 129-133.

[33] Thorne K, Ting SJ, Chu CJ, Mackenzie JD, Getman TD, Hawthorne MF. Synthesis of TiC via polymeric titanates: the preparation of fibres and thin films. *Journal of Materials Science*. 1992;27(16):4406-14.

[34] Mas-Guindal MJ, Contreras L, Turrillas X, Vaughan GBM, Kvik Å, Rodríguez MA. Self-propagating high-temperature synthesis of TiC-WC composite materials. *Journal of Alloys and Compounds*. 2006;419(1-2):227-33.

[35] Saidi A. Reaction synthesis of Fe-(W,Ti)C composites. *Journal of Materials Processing Technology*. 1999;89-90(0):141-4.

[36] Teber A, Schoenstein F, Têtard F, Abdellaoui M, Jouini N. The effect of Ti

substitution by Zr on the microstructure and mechanical properties of the cermet  $\text{Ti}_{1-x}\text{Zr}_x\text{C}$  sintered by SPS. *International Journal of Refractory Metals and Hard Materials*. 2012;31(0):132-7.

[37] Kim YK, Shim J-H, Cho YW, Yang H-S, Park J-K. Mechanochemical synthesis of nanocomposite powder for ultrafine (Ti, Mo)C–Ni cermet without core-rim structure. *International Journal of Refractory Metals and Hard Materials*. 2004;22(4–5):193-6.

[38] Zhang S. Titanium carbonitride-based cermets: processes and properties. *Materials Science and Engineering: A*. 1993;163(1):141-8.

[39] Kim Jiwoong SK. Mechanical, thermo-physical and thermodynamic properties of Ti-based solid solution materials and their behavior with Ni binder. Seoul National University, Ph D., 2011.

[40] Marques L, Pinto HM, Fernandes AC, Banakh O, Vaz F, Ramos MMD. Optical properties of titanium oxycarbide thin films. *Applied Surface Science*. 2009;255(10):5615-9.

[41] Fernandes AC, Carvalho P, Vaz F, Lanceros-Méndez S, Machado AV, Parreira NMG, et al. Property change in multifunctional  $\text{TiC}_x\text{O}_y$  thin films: Effect of the O/Ti ratio. *Thin Solid Films*. 2006;515(3):866-71.

[42] Hewitt SA, Kibble KA. Effects of ball milling time on the synthesis and consolidation of nanostructured WC–Co composites. *International Journal of Refractory Metals and Hard Materials*. 2009;27(6):937-48.

[43] Sangho Park, S. Kang, Synthesis of (Ti,M1 M2)(CN)-Ni nanocrystalline powders. *International Journal of Refractory Metal & Hard Materials*. 2006;(24) 2006 115-121.

[44] Jiang WH, Fei J, Han XL. In situ synthesis of (TiW)C/Fe composites. *Materials Letters*. 2000;46(4):222-4.

[45] Ahn S, Kang S. Dissolution phenomena in the  $\text{Ti}(\text{C}_{0.7}\text{N}_{0.3})$ -WC-Ni system. *International Journal of Refractory Metals and Hard Materials*. 2008;26(4):340-5.

[46] Sangho Park YK, S.Kang. Synthesis of (Ti,M1 M2)(CN)-Ni nanocrystalline powders. *International Journal of Refractory Metal & Hard Materials*. 2006;(24) 2006 115-121.



- [47] Metcalfe A.G. The Mutual Solid Solubility of Tungsten Carbide and Titanium Carbide. *Journal Institute of Metals*. 1947;73:591.
- [48] Hanjung Kwon SK. Stability Domains of  $\text{TiO}_2$ - $\text{Ti}_3\text{O}_5$ - $\text{Ti}_2\text{O}_3$ - $\text{TiC}$ / $\text{Ti}(\text{CN})$  Systems During Reduction Process. *Journal of the American Ceramic Society*. 2009;92 (1):272-5.
- [49] IN-JAE JUNG SK. A study of the characteristics of  $\text{Ti}(\text{CN})$  solid solutions. *JOURNAL OF MATERIALS SCIENCE* 35 (2000) 87– 90. 2000.
- [50] Hanjung KWON SK. Carbothermal reduction of Titanium monoxide ( $\text{TiO}$ ). *Journal of the Ceramic Society of Japan* 2008;10(116):1154-8.
- [51] Adipuri A, Zhang G, Ostrovski O. Chlorination of Titanium Oxycarbide Produced by Carbothermal Reduction of Rutile. *Metallurgical and Materials Transactions B*. 2008;39(1):23-34.
- [52] Adipuri A, Zhang G, Ostrovski O. Chlorination of Titanium Oxycarbonitride Produced by Carbothermal Nitridation of Rutile. *Industrial & Engineering Chemistry Research*. 2008;48(2):779-87.
- [53] De Boer JH. *The Dynamical Character of Adsorption*. Second ed. Oxford University: Oxford; 1968.
- [54] Urbonaite Sigita. *Synthesis and Characterisation of Carbide Derived Carbons*. Stockholm University, Ph D., 2008.
- [55] Rouquerol F RJ, Sing K,. *Adsorption by Powders and Porous Solids*. London: Principles; 1999.
- [56] Huo Q, Margolese DI, Stucky GD. Surfactant Control of Phases in the Synthesis of Mesoporous Silica-Based Materials. *Chemistry of Materials*. 1996;8(5):1147-60.
- [57] Kruk M, Jaroniec M, Sayari A. Application of Large Pore MCM-41 Molecular Sieves To Improve Pore Size Analysis Using Nitrogen Adsorption Measurements. *Langmuir*. 1997;13(23):6267-73.
- [58] Kruk M, Jaroniec M. Gas Adsorption Characterization of Ordered Organic–Inorganic Nanocomposite Materials. *Chemistry of Materials*. 2001;13(10):3169-83.
- [59] Mason G. The effect of pore space connectivity on the hysteresis of capillary condensation in adsorption—desorption isotherms. *Journal of Colloid and*

Interface Science. 1982;88(1):36-46.

[60] Takenaka S, Takahashi R, Sato S, Sodesawa T, Matsumoto F, Yoshida S. Pore size control of mesoporous SnO<sub>2</sub> prepared by using stearic acid. *Microporous and Mesoporous Materials*. 2003;59(2–3):123-31.

[61] Brunauer S, Emmett PH, Teller E. Adsorption of Gases in Multimolecular Layers. *Journal of the American Chemical Society*. 1938;60(2):309-19.

[62] Adamson AWG, A. P. *Physical Chemistry of Surfaces*. 6th ed. New York: John Wiley & Sons; 1997.

[63] Lippens BC, de Boer JH. Studies on pore systems in catalysts: V. The t method. *Journal of Catalysis*. 1965;4(3):319-23.

[64] Sing KSW. The use of physisorption for the characterization of microporous carbons. *Carbon*. 1989;27(1):5-11.

[65] Mikhail RS, Brunauer S, Bodor EE. Investigations of a complete pore structure analysis: I. Analysis of micropores. *Journal of Colloid and Interface Science*. 1968;26(1):45-53.

[66] Olivier JP. Improving the models used for calculating the size distribution of micropore volume of activated carbons from adsorption data. *Carbon*. 1998;36(10):1469-72.

[67] Tarazona P. Free-energy density functional for hard spheres. *Physical Review A*. 1985;31(4):2672-9.

[68] Tarazona P, Evans R. A simple density functional theory for inhomogeneous liquids. *Molecular Physics*. 1984;52(4):847-57.

[69] Seaton NA, Walton JPRB, Quirke N. A new analysis method for the determination of the pore size distribution of porous carbons from nitrogen adsorption measurements. *Carbon*. 1989;27(6):853-61.

[70] Rios R, Sunden H, Ibrahim I, Zhao G-L, Eriksson L, Cordova A. Highly Enantioselective Synthesis of 2H-1-Benzothiopyrans by a Catalytic Domino Reaction. *ChemInform*. 2007;38(12):no-no.

[71] Barrett EP, Joyner LG, Halenda PP. The Determination of Pore Volume and Area Distributions in Porous Substances. I. Computations from Nitrogen Isotherms. *Journal of the American Chemical Society*. 1951;73(1):373-80.

- [72] Ravikovitch PI, Neimark AV. Characterization of nanoporous materials from adsorption and desorption isotherms. *Colloids and Surfaces A: Physicochemical and Engineering Aspects*. 2001;187-188(0):11-21.
- [73] Ravikovitch PI, Neimark AV. Density Functional Theory Model of Adsorption on Amorphous and Microporous Silica Materials. *Langmuir*. 2006;22(26):11171-9.
- [74] Manukyan NV, Martirosyan VH. Investigation of the chlorination mechanism of metal oxides by chlorine. *Journal of Materials Processing Technology*. 2003;142(1):145-51.
- [75] Sui J, Lu J-J. Synthesis of carbon nitride powder by selective etching of  $\text{TiC}_{0.3}\text{N}_{0.7}$  in chlorine-containing atmosphere at moderate temperature. *Materials Chemistry and Physics*. 2010;123(1):264-8.
- [76] Ranjan Kumar Dash. Nanoporous Carbons Derived from Binary Carbides and their Optimization for Hydrogen Storage. Drexel University, Doctor of Philosophy, 2006.
- [77] Presser V, Heon M, Gogotsi Y. Carbide-Derived Carbons – From Porous Networks to Nanotubes and Graphene. *Advanced Functional Materials*. 2011;21(5):810-33.
- [78] Walton KS, Snurr RQ. Applicability of the BET Method for Determining Surface Areas of Microporous Metal–Organic Frameworks. *Journal of the American Chemical Society*. 2007;129(27):8552-6.
- [79] Lastoskie C, Gubbins KE, Quirke N. Pore size distribution analysis of microporous carbons: a density functional theory approach. *The Journal of Physical Chemistry*. 1993;97(18):4786-96.
- [80] Silvestre-Albero J, Silvestre-Albero A, Rodríguez-Reinoso F, Thommes M. Physical characterization of activated carbons with narrow microporosity by nitrogen (77.4 K), carbon dioxide (273 K) and argon (87.3 K) adsorption in combination with immersion calorimetry. *Carbon*. 2012;50(9):3128-33.
- [81] Gleb Yushin YG. Carbide-Derived Carbons: Effect of Pore Size on Hydrogen Uptake and Heat of Adsorption. *Adv Funct Mater*. 2006(16):2288–93.
- [82] D. R. Gaskell. *Introduction to the Thermodynamics of Materials*. 4<sup>th</sup>. New

York and London,; 2003.

- [83] Kwon H. Stability Domains of  $\text{TiO}_2\text{--Ti}_3\text{O}_5\text{--Ti}_2\text{O}_3\text{--TiC/Ti(CN)}$  Systems During Reduction Process. *J Am Ceram Soc.* 2009;92.
- [84] Katsumi Kaneko\*. Determination of pore size and pore size distribution 1. Adsorbents and catalysts. *Journal of Membrane Science* 1994;96:59-89.
- [85] Ellestad OH, Blindheim U. Reactions of titanium tetrachloride with silica gel surfaces. *Journal of Molecular Catalysis.* 1985;33(3):275-87.
- [86] Chmiola J, Yushin G, Dash R, Gogotsi Y. Effect of pore size and surface area of carbide derived carbons on specific capacitance. *Journal of Power Sources.* 2006;158(1):765-72.
- [87] Zheng J, Ekstrom TC, Gordeev SK, Jacob M. Carbon with an onion-like structure obtained by chlorinating titanium carbide. *Journal of Materials Chemistry.* 2000;10(5):1039-41.
- [88] X.A. Zhao CWO, Y.C. Tsang, Y.W. Wong, P.W. Chan, C.L. Choy,. *Appl Phys Lett.* 1995;66(66):2652.
- [89] U. Gelius RFH, J. Hedman, B.J. Lindberg, R. Manne, R., Nordberg RN, K. Siegbahn,. *Phys Scr.* 1970;2:70.
- [90] A. Johansson SS. *J Chem Phys.* 1999;111:3203.
- [91] T. Maiyalagan BV. Template synthesis and characterization of well-aligned nitrogen containing carbon nanotubes. *Materials Chemistry and Physics.* 2005;93:291-5.
- [92] Y. Park VC, Y. Gao, B. R. Hsieh, and C. W. Tang,. *Appl Phys Lett.* 1996;68:2699.
- [93] Abell GC. Empirical chemical pseudopotential theory of molecular and metallic bonding. *Physical Review B.* 1985;31(10):6184-96.
- [94] Tersoff J. Empirical Interatomic Potential for Carbon, with Applications to Amorphous Carbon. *Physical Review Letters.* 1988;61(25):2879-82.
- [95] Tersoff J. New empirical approach for the structure and energy of covalent systems. *Physical Review B.* 1988;37(12):6991-7000.
- [96] Tersoff J. New empirical model for the structural properties of silicon. *Physical Review Letters.* 1986;56(6):632-5.

- [97] Ni B, Lee K-H, Sinnott SB. A reactive empirical bond order (REBO) potential for hydrocarbon–oxygen interactions. *Journal of Physics: Condensed Matter*. 2004;16(41):7261.
- [98] Brenner DW, Shenderova OA, Harrison JA, Stuart SJ, Ni B, Sinnott SB. A second-generation reactive empirical bond order (REBO) potential energy expression for hydrocarbons. *Journal of Physics: Condensed Matter*. 2002;14(4):783.
- [99] Brenner DW. Empirical potential for hydrocarbons for use in simulating the chemical vapor deposition of diamond films. *Physical Review B*. 1990;42(15):9458-71.
- [100] Jornada FH, Gava V, Martinotto AL, Cassol LA, Perottoni CA. Modeling of amorphous carbon structures with arbitrary structural constraints. *Journal of Physics: Condensed Matter*. 2010;22(39):395402.
- [101] Hu J, Ruan X, Chen YP. Thermal Conductivity and Thermal Rectification in Graphene Nanoribbons: A Molecular Dynamics Study. *Nano Letters*. 2009;(7):2730-5.
- [102] Cao JX, Yan XH, Xiao Y, Ding JW. Thermal conductivity of zigzag single-walled carbon nanotubes: Role of the umklapp process. *Physical Review B*. 2004;69(7):073407.
- [103] P. M. Kroll. Computer simulations and X-ray absorption near edge structure of silicon nitride and silicon carbonitride. Ph.D, 1996.
- [104] de Brito Mota F, Justo JF, Fazzio A. Structural properties of amorphous silicon nitride. *Physical Review B*. 1998;58(13):8323-8.
- [105] Dyson AJ, Smith PV. Extension of the Brenner empirical interatomic potential to C&unknown;Si&unknown;H systems. *Surface Science*. 1996;355(1):140-50.
- [106] Gale JD, Rohl AL. The General Utility Lattice Program (GULP). *Molecular Simulation*. 2003;29(5):291-341.
- [107] Connolly M. Solvent-accessible surfaces of proteins and nucleic acids. *Science*. 1983;221(4612):709-13.
- [108] Connolly ML. Computation of molecular volume. *Journal of the American Chemical Society*. 1985;107(5):1118-24.
- [109] Düren T, Millange F, Férey G, Walton KS, Snurr RQ. Calculating Geometric Surface Areas as a Characterization Tool for Metal–Organic Frameworks. *The*

Journal of Physical Chemistry C. 2007;111(42):15350-6.

[110] United States Department of Energy. Hydrogen storage technologies road map. In: Energy USDo, ed. Washington 2005.

[111] D.P. B. Hydrogen Storage Materials: The Characterisation of Their Storage Properties London: Springer-Verlag; 2011.

[112] Züttel A. Materials for hydrogen storage. Materials Today. 2003;6(9):24-33.

[113] Schlapbach LZ, A,. Hydrogen-Storage Materials for Mobile Applications. Nature 2001;414:353-8.

[114] Armandi M, Bonelli B, Areán CO, Garrone E. Role of microporosity in hydrogen adsorption on templated nanoporous carbons. Microporous and Mesoporous Materials. 2008;112(1–3):411-8.

[115] Dash R, Chmiola J, Yushin G, Gogotsi Y, Laudisio G, Singer J, et al. Titanium carbide derived nanoporous carbon for energy-related applications. Carbon. 2006;44(12):2489-97.

[116] Arulepp M, Leis J, Lätt M, Miller F, Rumma K, Lust E, et al. The advanced carbide-derived carbon based supercapacitor. Journal of Power Sources. 2006;162(2):1460-6.

[117] Jerome. A, inventor Mixed reactant molecular screen fuel cell,. America. 2005.

[118] H. Simgen GH, G. Zuzel,. Adsorption techniques for gas purification. Applied Radiation and Isotopes. 2004;61:213-7.

[119] B.E. Conway. Electrochemical Supercapacitors. New York,; Kluwer Academic Publishers; 1999.

[120] A.W. Burke. Ultracapacitors: why, how, and where is the technology. J Power Sources 2000;91:37–50.

[121] M. Arulepp. Electrochemical characteristics of porous carbon materials and electrical double layer capacitors. Tartu University; 2003.

[122] Barbieri O, Hahn M, Herzog A, Kötz R. Capacitance limits of high surface area activated carbons for double layer capacitors. Carbon. 2005;43(6):1303-10.

[123] J. Leis MA, M. Lätt, H. Kuura,, inventor A method of making the porous carbon material and porous carbon materials produced by the method. 2005.

## 국문 초록

본 연구는 Ti기반 고용상 재료의 조성 조절 및 염소화 공정을 통하여 기공의 크기 및 특성을 조절한 연구로써 기존에 연구가 되었던 단순한 Binary(TiC, ZrC, HfC, VC, WC, Mo<sub>2</sub>C, TaC) 또는 Ternary(MAX: TiAl<sub>2</sub>C, Ti<sub>3</sub>Si<sub>2</sub>C) CDC(Carbide Derived Carbon)에서 벗어나 원하는 원소를 원하는 만큼의 양을 도입 및 조절할 수 있는 고용상을 사용하였다. 고용상 원료분말을 MA(Mechanical Alloying)방법을 이용하여 합성하고, 염소화 공정으로 Ti를 제거하여 CDC의 기공 구조를 조절할 수가 있었다. 얻은 실험 결과를 바탕으로 CDC 기공 구조의 생성 메커니즘을 규명하였으며, 가정을 적용하고 경험적인 방법을 사용하여 Molecular Dynamics 시뮬레이션을 계산한 결과, 눈으로는 확인 할 수 없었던 CDC의 구조를 규명하고 기공특성들을 계산하여 새로운 고용상CDC의 디자인에 밑거름이 되는 기초자료를 제공한다.

Ti(C<sub>1-x</sub>O<sub>x</sub>)CDC의 경우 기존에 알려진 일반 CDC에 비해 높은 마이크로기공을 및 SSA와 pore volume을 가지고 있었으며, 이로 인하여 저압 및 고압 모두에서 높은 수소저장량을 보였다. 이에 반하여 메조 기공을 주로 가지는 Ti(C<sub>1-x</sub>N<sub>x</sub>)CDC의 경우, Capacitance를 측정하여 기존에 알려진 CNT와 활성탄과 비교하여 산업으로의 응용 가능성을 보여 주었다.

핵심어: 고용상, CDC, 기공, Molecular Dynamics, 수소저장, Supercapacitor

## 감사의 글

Defence를 마치고 느낀 것은 세상에 혼자서 할 수 있는 일은 없었다는 것입니다. 학위를 마치기까지 많은 사람들의 도움이 있었습니다. 받은 고마움을 일일이 찾아가서 감사를 드려야 하지만 일단은 이 글로 조금이나마 대신하려 합니다. 박사 학위를 받았다는 것은 그만큼 공부를 했다는 것보다는 학위과정의 시간만큼 많은 사람을 만나고, 그 사람들로부터 많은 것을 배우고 모든 것을 나누었다는 것이라고 생각합니다. 신경 쓸까봐 항상 연락도 잘 못하셨던 우리 부모님이신 서종화 지소장님과 박영애 여사님, 우리 아버지 어머니께서 계시지 않았다면 저는 아무것도 하지 못했을 것입니다. 든든히 뒤에서 저를 옹고 버텨 주셔서 지금까지 아무런 걱정 없이 공부를 할 수 있었습니다. 그 동안 받은 것이 너무 많아 생전 다 갚지는 못하겠지만, 이제부터라도 효도하겠습니다. 사랑합니다. 또한 이 논문을 완성하기까지 지도교수님인 강신후 교수님께서 많은 전공 지식과 삶을 살아가는 자세, 하느님, 연구자로서의 도덕 등 셀 수 없이 많은 것들을 가르쳐 주셨습니다. 언제나 저를 지켜봐 주시고 믿어주시고 잘못했을 때는 바로 잡아주시는 교수님을 보면서, 제 삶의 목표가 되어 주셨습니다. 모나고 이기적인 저를 등글게 다듬어주신 강신후 교수님과 강윤희 사모님께 감사의 말씀드립니다. 꼭 오랫동안 건강하세요. 저도 교수님 사모님같이 아름다운 가정을 이루고 살아가고 싶습니다. 또한 든든히 내 옆에서 나만 바라봐주는 경주... 정말 고맙고 사랑해 그리고 미안해. 남에게 상처만 주던 나를 따듯이 안아준 너... 이제 남은 인생 함께 잘 지내자. 이 못난 형을 멘토라고 항상 따라다니던 내 친동생 우리 착한 광수... 넌 내 진정한 동생이야 고맙다. 그리고 미안해. 항상 옆에 있으면서 희로애락을 함께 했던 우리 CMC식구들 역시 저의 소중한 인연입니다. 불안할 때면 항상 옆에서 든든히 안심시켜주던 아빠 같은



지웅이형과 슬플 때나 기쁠 때나 힘들 때나 항상 함께였던 엄마 같은 재혁이형, 수소저장물질 과제를 함께 시작해서 같이 염소가스도 마시면서 고생하고 날 힘들게도 했던 그냥 키가 큰 진홍이(말좀 해), 언제나 열심히 하고 차분해서 가르쳐 줄 것보다 배울 것이 많던 진명이, 친구 같기도 하고 동생 같기도 해서 챙겨주고 싶은 내 뒤를 따를 재희, 곧 영어 넘고 벌떡 일어나 실 승희형, 같이 졸업했어야 했는데 아쉬운 가오제(힘내), 든든하면서도 의지가 됐던 재철이형, 같이 일은 많이 못했지만 열심히 하면서도 오해로 나한테 제대로 한번 혼났던 충권이(고생했다ㄸ), 불쌍한 정민이형(힘내요), 들어올 때나 들어와서나 이슈를 많이 만드는 귀여운 여자친구 없는 지선이, 황금 인백이자 외국인이자 언제나 병장 같은 막내 문균이, 같은 방이 아니고 밤에는 잘 안보여서 아직 많이는 친해지지 못한 바투형(국화빵 다이어트 그만 하시길...), 마흐디도 고생하고 있지만 더 열심히 하세요.

“모두 정말 보고 싶을 거야 정말로... 가끔 놀러올께”

이름은 다 넣지 못했지만 CMC졸업 선배님들도 모두 감사드립니다. 용선이형, 선용이형, 오성이형, 한중이형, 태형이형, 지성이형, 주흥이형, 동현이형, 효문이형, 그 중에서도 특히 마지막 실험을 도와주신 김용선교수님은 우리 실험실의 자람이자 제가 존경하는 선배님 중에 하나입니다. (형의 길을 가고 싶습니다!) 이 밖에도 우리 밴드부 장재혁형, 성대형, 태영이, 승표형, 종명이형, 우진이(정말 고맙다ㅠㅠ), 효진이, 병선이, 태형이, 승재형 모두모두 정말 감사드립니다. 또한, ADD 프로젝트를 함께 했던 류성수 박사님께도 감사의 말씀 드리고 디펜스 위원을 허락해주신 한승우 교수님, 남기태 교수님, 한화케미칼 상무 김동욱박사님, 카이스트 전석우 교수님 정말로 감사드립니다. 마지막으로 아직은 조금 멀리 계시는 것 같은 하나님께 모든 영광을 드립니다. 앞으로 계속 다가가겠습니다. 감사합니다.

2012년 8월 서문수 올림.